Models based on space-time symmetries in transitional film flows and turbulent wall-bounded shear flows

by

Fernando G. Carbone

A dissertation submitted to the Graduate Faculty in Physics in partial fulfillment of the requirements for the degree of Doctor of Philosophy, The City University of New York

1996

This manuscript has been read and accepted by the Graduate Faculty in Physics in satisfaction of the dissertation requirement for the degree of Doctor of Philosophy.

11/10/1995 — Nadine Aubry

Date — Chair of Examining Committee

1/29/96 — Joseph S. Imbo

Date — Executive Officer

Professor Andreas Acrivos

Professor Nadine Aubry

Professor Joel Koplik

Professor Dimitry Papageorgiou

Professor Micha Tomkiewicz

Supervisory Committee

The City University of New York

Abstract

Models based on space-time symmetries in transitional film flows and turbulent wall-bounded shear flows

by

Fernando G. Carbone

Advisor: Prof. Nadine Aubry

Falling film flows and turbulent shear flows are modeled by means of biorthogonal decomposition techniques and space-time symmetry considerations. The analysis of experimental data shows that fluid films falling down an inclined plane are subject to spatio-temporal modulations as the Reynolds number is increased; this leads to a process of splitting and coalescence of front waves in physical space. The study of the system in its subharmonic regime clearly shows the convective nature of the instability as well as intermittency in both space and time. It is shown that inhomogeneous wall-bounded shear turbulence can be decomposed in terms of families of spatial and temporal orthogonal modes. In each family there exists a mother function from which all the other modes can be generated by successive stretchings of the mother, and whose energies are exponentially related to that of the mother. This corresponds to an exponentially decaying spectrum law. Due to the presence of a wall, the stretching symmetry must adapt by acting across the spatial domain (in the direction normal to the wall) in a non-homogeneous manner which is explicitly computed analytically.

The previous arguments are tested on statistical data obtained by direct numerical simulation of turbulent channel flow. A good agreement is found within the "inertial range" of the spectrum, excluding the first five modes or so. Within this range, two families of self-similar modes can be extracted and deduced from a mother mode via stretching. The latter persists among the first five modes, but the stretching law is slightly different from that valid in the "inertial range" of the spectrum.

To my family.

Acknowledgments

I am deeply thankful to my advisor, Professor Nadine Aubry, for her constant guidance and support throughout my work on this thesis. Her assistance, constructive criticism, and suggestions were essential components of this research. In addition, I would like to specifically thank her for helping me with my English grammar.

I must also express my gratitude to both Dr. Ricardo Lima, whose enthusiasm, insightful suggestions, and fruitful late night discussions helped me so much, and to Professor Andreas Acrivos, director of the Benjamin Levich Institute where this research was accomplished, for his encouragements.

I am grateful to Dr. Jun Liu and Professor Jerry Gollub for providing the experimental data used in part of this research and for the productive collaboration that resulted. I would like to thank Prof. R. Moser, Prof. P. Moin and Prof. J. Kim for sharing the two-point correlation data analyzed in this work.

Finally, I wish to thank Mary Wright for her constant assistance and efficiency in providing wonderful working conditions. Many thanks also to my friends in the Institute: Anurag, Anubhav, Bir, Cao, Dimas, Erik, Jana, Jysoo, Kai, Knut, Mohamed, Nikolaos, Pawel, Said and Wang for the nice time together and their help, and to my friends from school back in Argentina: Cristina, Dario, Fabian, Javier, Juan, Luis, Marcelo, and Ruben who, dispite the distance separating us, have been a source of constant support. I am also greatful to the City College Security and the cheap 24 hs

East Village restaurants that made my nocturnal habits feasible.

This research was supported by the ONR, under grant number N00014-90-J-1554, Fluid Dynamics program (Code 1132F), and NSF/PYI award number MSS89-57462.

Contents

List of Figures

Chapter 1

Introduction

The relevance of symmetries in physical systems is well-known in science. The conservation of energy in Hamiltonian systems, selection rules for atomic and nuclear spectra, the Buckingham Pi theorem in fluid mechanics are just a few examples of physical properties determined by the invariance of the involved variables under particular transformations applied to the governing equations. Although the above results can be obtained by working out the equations directly, group theoretical techniques make the task considerably simpler. Given the corresponding ordinary differential equations (ODE) or partial differential equations (PDE) describing the system considered, there is a large battery of tools available to reduce the original mathematical problem to a simpler one and classify the possible solutions according to their symmetries [1, 2]. Similar techniques can be applied to matrix operators [3]. Although the knowledge of the symmetries may not suffice, in most cases, it leads to the derivation of a simpler model which describes the observed phenomena. While such techniques have been developed mostly in the framework of temporal dynamics only, the aim of the present work is an extension to space-time dynamical systems.

Of technological and scientific importance, hydrodynamic systems provide a par-

ticularly interesting opportunity to study space-time dynamics. Such systems are rich sources of space-time phenomena and appear to exhibit common routes to spatio-temporal complexity such as those involving defects, symmetry-breaking, and modulations. The major difficulty in understanding fluid flows, even when they are incompressible, lies in the fact that the dimensionless governing equations

$$\frac{\partial \boldsymbol{u}}{\partial t} + (\boldsymbol{u}.\boldsymbol{\nabla})\boldsymbol{u} = -\boldsymbol{\nabla} p + \frac{1}{Re}\boldsymbol{\nabla}^2 \boldsymbol{u} \,, \tag{1.1a}$$

$$\boldsymbol{\nabla}.\boldsymbol{u} = 0 \,, \tag{1.1b}$$

the Navier-Stokes (NS) equations [4, 5], are nonlinear and very difficult to solve, especially as Reynolds number increases. Here, $\boldsymbol{u}$ represents the velocity field, p the pressure, and Re the Reynolds number. While at low Reynolds numbers, linearization procedures are available, this is no longer the case at high Reynolds numbers when the fluid becomes turbulent and nonlinear terms are important.

Sophisticated experiments and computer simulations provide us with an increasingly large amount of data exhibiting intriguing phenomena which raise challenging questions to theorists. Until now, two major theoretical approaches have been used for the treatment of complex fluid dynamical systems, the first one concentrating on a statistical description of the flow, the other one using dynamical systems theory. Both have their limitations. Statistical methods, mainly intended for the treatment of fully developed turbulence, present closure problems in the derived (statistical) equations. In addition, they do not address the description of the space-time dynamics. Dynamical systems theory has had a large impact on the understanding of complex systems, but it has concentrated on either temporal dynamical phenomena or weakly nonlinear stages. No theoretical approach is available yet for spatio-temporal nonlinear dynamics. Although great advances have been achieved, the problem at the PDE level, due to its complexity, is far from being resolved.

The purpose of this work is to derive simple models which capture the space-time behavior of two unsteady fluid dynamical systems. The first one is a film flow falling down on an inclined plane [6, 7] for which the film thickness $h(x,t)$ is measured experimentally. The second system is a fully developed turbulent channel flow numerically simulated by Kim *et al.* [8] (see also [9]). In both cases, I concentrate on the identification of the involved symmetries and the characterization of the dynamics, which, in turn, will be used in the derivation of appropriate models.

1.1 The Analysis of Complex Systems

The above discussion raises the question of how to extract meaningful information from systems in which both the spatial behavior and the temporal evolution must be taken into account. More precisely, how to analyze and model a function $u(x,t)$ in order to capture the dynamics, identify coherent structures, detect bifurcations, etc.? Several methodologies have been used to address this issue, one of the oldest techniques being the Fourier decomposition; more recently wavelet analyses have attracted the attention of many scientists. They both lack the ability to adapt to a general situation and must be used in particular cases. In this work I address the previous issues by using biorthogonal decompositions (BOD), which have been proposed by Aubry *et. al* [10, 11, 12] and used as a tool for studying spatio-temporal dynamics (see [13] for instance). Its major feature consists in providing a deterministic method for space-time data analysis (in the sense of keeping track of space and time variables simultaneously), which leads to the extraction of order, structures and symmetries from space-time complexity. The functional operators are defined by the signal itself and therefore its applicability is general, in contrast with the two alternate methods previously mentioned. Indeed, having its analytical foundation in linear operator

theory, the BOD allows the introduction of symmetry operators (in space-time). The major features of the BOD, including its capability to detect space-time symmetries, necessary for the present work, are outlined in Chapter 2.

As in any numerical analysis, understanding the effects of the discretization of a given signal is of fundamental importance. Besides the euristic argument that the signal defined on the discretization grid must resemble the original function, one must also investigate the effect of discretization on the decomposition itself. In other words, how are the spectrum and functions of the decomposition affected? A detailed analysis addressing these questions in the framework of biorthogonal decompositions is given in Chapter 3. There, a result similar to the Nyquist condition for the Fourier analysis is derived.

1.2 Film Flows

The system under study is an incompressible Newtonian liquid flowing on an inclined surface that makes an angle β with the horizontal. Thin liquid films flowing on an inclined surface are frequently found in engineering and natural processes. The coordinates are chosen such that x is the downstream (or flow) direction, y is the transverse coordinate in the film plane, and z is perpendicular to the film plane (x, y). The Reynolds number $Re = u_0 h_0/\nu$ is based on the unperturbed film thickness h_0, the fluid velocity u_0 at the surface, and the kinematic viscosity ν. The Weber number $W = \gamma/(\rho h_0^2 g \sin\beta)$ is used to represent the effect of surface tension, where γ is the surface tension itself, ρ is the density, and g is the gravitational acceleration. The boundary conditions for this problem are:

$$\boldsymbol{u} = \mathbf{0} \quad at\ z = 0\,, \tag{1.2a}$$

$$\hat{t}(\hat{n}\overleftrightarrow{\sigma}) = 0 \quad at\ z = h(x,y,t)\,, \tag{1.2b}$$

$$\hat{n}(\hat{n}\overleftrightarrow{\sigma}) + p_0 + \gamma(\frac{1}{r_1} + \frac{1}{r_2}) = 0 \quad at\ z = h(x,y,t)\,, \tag{1.2c}$$

where $\hat{n}$ and $\hat{t}$ are the normal and tangential unit vectors at the free surface, p_0 the atmospheric pressure, r_1 and r_2 are the surface principal radii of curvature defined positive when directed toward the film, and the stress tensor $\overleftrightarrow{\sigma}$ is defined by

$$\overleftrightarrow{\sigma} = -p\,\overleftrightarrow{1} + \eta(\overleftrightarrow{\nabla u} + (\overleftrightarrow{\nabla u})^T)\,.$$

Equation (1.2a) represents the no-slip boundary condition. Equations (1.2b) and (1.2c) express that at the liquid surface, the tangential stress must vanish, and the normal stress balances the induced pressure by the surface tension. The relation between the velocity and the film thickness is given by

$$u_z = \frac{\partial h}{\partial t} + \boldsymbol{u}.\nabla h \quad at\ z = h(x,y,t).$$

The initial instability of the system occurs for sufficiently long waves $\alpha < \alpha_c(Re)$ when Re is above the critical Reynolds number $Re_c = (5/4)\cot\beta$, where $\alpha = 2\pi h_0/\lambda$ is the dimensionless wavenumber, and λ is the wavelength. The neutral wavenumber $\alpha_c(Re)$ is determined by surface tension, which damps the short wavelengths. Careful experiments showed that the linear stability analysis is successful in predicting the onset of instability, the growth rates, and the wave velocities of small (infinitesimal) amplitude waves [7]. The waves are spatially developing: they grow as they travel downstream. For the experiment analyzed in this work, the typical wavelength is several centimeters while the average film thickness is about one millimeter.

Initial waves are two-dimensional (i.e., invariant in the y-direction) and can be described by the film thickness $h = h(x,t)$ as a function of one space dimension and time, otherwise they are called three-dimensional. Because the primary instability

is convective and sensitive to noise at the source [7, 14, 15], the spontaneous waves due to ambient noise are always irregular. To investigate the evolution of initially sinusoidal waves, it is common to apply a small sinusoidal forcing. The perturbation frequency f then becomes an experimentally controlled parameter.

The nonlinear development of initially sinusoidal waves depends strongly on their frequency (or wavenumber). At low frequencies, the nonlinear interaction leads to the development of localized solitary waves, each consisting of a large maximum and several bow waves in front (see Fig. 1.1a). At high frequencies, saturated nearly sinusoidal waves occur close to the neutral frequency $f_c(Re)$. At intermediate frequencies, nonlinear effects may still be sufficiently strong to produce several subsidiary maxima in one period, but separate pulses cannot be formed and the primary wavefronts are close together (see Fig. 1.1b). A boundary in the (Re, f) plane separating saturated single peaked waves from multipeaked and solitary waves has been identified experimentally [7].

Both two- and three-dimensional instabilities can occur, they are frequency dependent and they both lead to a transition to spatiotemporal chaos downstream. In the two-dimensional (high viscosity) case, Jun *et al.* [16] showed the occurrence of secondary subharmonic and sideband instabilities, but for different ranges of frequencies. Subharmonic instabilities appear at low frequencies, while sideband instabilities predominate at high frequencies. Using a center manifold analysis, Cheng *et al.* [17] predicted that finite amplitude monochromatic states become unstable to subharmonic instabilities. Lin [18, 19] carried out a sideband stability analysis of sinusoidal waves by deriving a complex Ginzburg-Landau equation. A more general and modern approach using center manifold analysis were performed by Cheng *et al.* [20] and Fujimura [21]. At lower viscosities and high Re, the wavefronts are subject to transverse instabilities: a spatially synchronous instability dominates over a wide range

of frequencies, while subharmonic transverse modulations are found close to the neutral frequency [22]. After sufficient nonlinear evolution, the flows are dominated by solitary waves whether they are forced periodically or not [23].

An equation that can capture most of the nonlinear phenomena accurately is not available. The full NS equations (1.1) with nonlinear free surface boundary conditions (1.2b) and (1.2c) are extremely complicated. Most investigations have been based on model equations which are much simpler than the NS equations [24, 25]. One approach is a long wave expansion requiring small wavenumbers $\alpha \ll 1$ and low Re. Two important model equations are the Benney equation [26] and the Kuramoto-Sivashinsky equation (KS) [24]. They have been used to predict the existence of solitary waves at small frequencies and nearly sinusoidal waves close to the neutral frequency. Some secondary instability analyses have also been based on these equations. However, their applicability is limited, for instance, the Benney equation can produce singularities at finite time [27, 28, 29], and the KS equation is limited to Re very close to criticality and small wave amplitudes.

Another approach, known as the boundary-layer (BL) approximation, was used by Chang *et al.* [24, 30], for instance, who investigated travelling waves on vertical falling films. Assuming long wavelength and strong surface tension, the BL [31] considerably simplifies the NS equations and boundary conditions into another group of equations that is appropiate for most flows with $Re < 500$, and is more convenient to study numerically. As Re approaches zero, stationary wave solutions of the BL equations collapse into those of the KS equation. Their approximation does not assume a self-similar velocity profile as in the boundary layer model of Trifonov and Tsvelodub [32, 33], then providing a better description. Chang, Demekhin and Kopelevich [30] found two nonlinear stationary wave families (γ_1 and γ_2) in the BL equations. A wave denoted γ_1 has a velocity smaller than the linear one of the same wavenumber,

while another one, denoted γ_2, travels faster. The γ_1 waves are nearly sinusoidal for wavenumbers close to the neutral curve while the γ_2 family possesses no such sinusoidal shape. The computed solitary wave profiles on vertically falling films compare well with those reported experimentally [30]. Because of the complication of the BL equations, a reduced version, known as the integral-boundary-layer equations [24], is sometimes used to obtain a qualitative picture of various secondary instabilities. Liu and Gollub [23] found their experimental results on inclined films to be in qualitative agreement with Chang *et al.*'s work to a certain extent, but many experimental results remain unexplained [34]. Furthermore, finite element calculations of the NS equations by Salamon, Armstrong and Brown [35] seem to question the validity of the BL equations over a certain range of Weber numbers.

In Chapter 4, I analyze two phenomena concerning the two-dimensional waves regime. The first one, not described elsewhere, consists of the splitting and coalescence of front waves as they travel downstream. The second one refers to the subharmonic instability, previously mentioned.

1.3 Turbulent Flows

The Navier-Stokes equations (1.1) establish that once the flow geometry is fixed, the fluid dynamics is completely characterized by a unique parameter, the Reynolds number $Re = UL/\nu$ and the initial condition. Here U and L are any characteristic velocity and length of the systems, and ν is the kinematic viscosity. If, for example, we consider a jet flow, U is the mean velocity and L is the diameter at the jet exit.

As Re increases, flows lose their smooth and laminar structure to become chaotic, in both space and time. The fluid is said to have become turbulent. In this general picture, for all fluids at high Re, large and small scale properties are observed. Large

scale fluctuations (e.g. big eddies) are geometry dependent and are of high interest for technological purposes. The small scale fluctuations are Re dependent and influence the large scale behavior.

Much of the (limited) understanding of fully turbulent flows lies on simple scaling laws. The first one was derived by Kolmogorov (K41) for the spatial Fourier spectrum of homogeneous turbulence (the $k^{-5/3}$ universal law). Its success has been such that any new model of turbulence is compared with this result. Kolmogorov assumed the existence of a length scale interval,

$$\eta \ll r \ll L \ ,$$

the so-called inertial subrange, where η is referred to as the Kolmogorov microscale. In this range, since $r \ll L$, the flow is considered isotropic, and since $\eta \ll r$, the effect of viscosity is neglected. The average rate of energy dissipation per unit mass ε plays a fundamental role. It governs the dynamics of the energy transfer from large scales to small scales. Kolmogorov's theory then predicts, through simple dimensional analysis, that the energy spectrum $E_1(k)$ is given by the scaling law

$$E_1(k) = \varepsilon^{2/3} k^{-5/3} f(k\eta)$$

where f is an unknown function. In this energy transfer from large to small scales, the energy dissipated rate is constant for all scales, which is a self-similarity assumption.

The above model does not account for the strong intermittency observed in the local rate of energy dissipation. For explaining these fluctuations, Obukhov [37] and Kolmogorov [38] introduced the *log-normal* model, namely a refined similarity hypothesis. Mandelbrot [39] and Frisch *et al.* [40] introduced fractal and multifractal models of turbulence giving a geometrical interpretation of the intermittency.

The hypothesis of homogeneity is fundamental in Kolmogorov's derivation. For inhomogeneous flows, the above arguments no longer hold and the expansion into

Fourier modes is no longer valid. There is no universal scaling theory for inhomogeneous turbulent flows.

In this work I attempt to address the above question by means of symmetry considerations. If there is a universal law comprising all fluid systems, it must lie, as in other areas of physics (e.g. quantum mechanics) and in mathematics (e.g. dynamical systems theory), in the concept of invariance. In Chapter 5, I apply the spatio-temporal scale symmetry properties of NS as a starting point for a scaling theory of wall bounded turbulence.

References for Chapter 1

[1] G. W. Bluman and S. Kumei, "Symmetries and Differential Equations," Applied Mathematical Sciences (Springer-Verlag, New York, 1989), Vol.**81**.

[2] P. Olver, "Applications of Lie Groups to Differential Equations", Graduate text in mathematics **107**.

[3] M. Hamermesh, "Group Theory and its Applications to Physical Problems" (Dover Publications, New York, 1989).

[4] G. K. Batchelor, An Introduction to Fluid Dynamics (Cambridge University Press, Cambridge, 1967).

[5] L. D. Landau and E. M. Lifshitz, "Fluid Mechanics", Course of Theoretical Physics (Pergamon Press, Oxford, 1980), Volume 6.

[6] P. L. Kapitza, S. P. Kapitza, Wave flow of thin viscous fluid layers, Zh. Eksp. Teor. Fiz. **19** 105 (1949); also in Collected Papers of P L. Kapitza, edited by D. Ter Haar (Pergamon, Oxford, 1965).

[7] J. Liu, J. D. Paul, and J. P. Gollub, Measurements of the primary instabilities of film flows, J. Fluid Mech. **250**, 69 (1993).

[8] J. Kim, P. Moin, and R. Moser, Turbulence in fully developed channel flow at low Reynolds number, J. Fluid Mech. **177**, 133 (1987).

[9] P. Moin and R. D. Moser, Characteristic-eddy decomposition of turbulence in a channel," J. Fluid Mech. **200**, 471 (1989).

[10] N. Aubry, R. Guyonnet, and R. Lima, Spatio-temporal analysis of complex signals: theory and applications, J. Stat. Phys. **64**, 683 (1991).

[11] N. Aubry, R. Guyonnet, and R. Lima, Spatio-temporal symmetries and bifurcations via biorthogonal decompositions. J. Nonlinear Sci. **2**, 183 (1992).

[12] N. Aubry, R. Guyonnet, and R. Lima, Turbulence Spectra, J. Stat. Phys. **67**, 183 (1992).

[13] P. Kolodner, S. Slimani, N. Aubry and R. Lima, Characterization of dispersive chaos and related states of binary-fluid convection, Physica D, **85**, 165 (1995).

[14] R. J. Deissler, Physica (Amsterdam) **25D**, 233 (1987).

[15] S. W. Joo, S. H. Davis, Instabilities of three-dimensional viscous falling films, J. Fluid Mech. **242**, 529 (1992).

[16] J. Liu and J. P. Gollub, Onset of spatially chaotic waves on flowing films, Phys. Rev. Lett. **70**, 2289 (1993).

[17] M. Cheng and H.-C. Chang, "Subharmonic instabilities of finite amplitude monochromatic waves,'' Phys. Fluids A **4**, 505 (1992).

[18] S. P. Lin, Finite-amplitude stability of a parallel flow with a free surface, J. Fluid Mech. **36**, 113 (1969).

[19] S. P. Lin, Finite amplitude side-band stability of a viscous film, J. Fluid Mech. **63**, 417 (1974).

[20] M. Cheng and H.-C. Chang, A generalized sideband stability theory via center manifold projection, Phys. Fluids A **2**, 1364 (1990).

[21] K. Fujimura, Method of center manifold and multiple scales for weakly nonlinear stability of fluid motions. Proc. R. Soc. Lond. A **434**, 719-733 (1991).

[22] J. Liu, J. Schneider and J. P. Gollub, Three-dimensional instabilities of film flows Phys. Fluids **7**, 55 (1995).

[23] J. Liu and J. P. Gollub, Solitary wave dynamics of film flows, Phys. Fluids **6**, 1702 (1994).

[24] H.-C. Chang, Wave evolution on a falling film, Annu. Rev. Fluid Mech. **26**, 103 (1994).

[25] S. P. Lin and C. Y. Wang, Modeling wavy film flows, in *Encyclopedia of Fluid Mechanics*, edited by N. P. Cheremisinoffs (Gulf, Houston, 1985), Vol. 1, p. 931.

[26] J. Benney, Long waves on liquid films, J. Math. Phys. **45**, 150 (1966).

[27] S. W. Joo, S. H. Davis, S. G. Bankoff, On falling film instabilities and wave breaking, Phys. Fluids A **3**: 231-32 (1991)

[28] A. Pumir, P. Manneville, and Y. Pomeau, On solitary waves running down an inclined plane, J. Fluid Mech. **135**, 27 (1983).

[29] P. Rosenau and A. Oron, Bounded and unbounded patterns of the Benney equation, Phys. Fluids A **4**, 1102 (1992).

[30] H.-C. Chang, E. A. Demekhin, and D. I. Kopelevich, Nonlinear evolution of waves on a vertically falling film, J. Fluid Mech. **250**, 433 (1993).

[31] E. A. Demekhin, I. A. Demekhin, and V. Y. Shkadov, Solitons in flowing layer of a viscous fluid, Izv. Akad. Nauk. SSSR, Mekh. Zhid. Gaza, No. 4, 9 (1983) [English translation: Fluid Dyn. **18**, 500 (1983)].

[32] Yu. Ya. Trifonov and O. Yu. Tsvelodub, Nonlinear waves on the surface of a falling liquid film. Part 1. Waves of the first family and their stability, J. Fluid Mech. **229**, 531 (1991).

[33] O. Yu. Tsvelodub and Yu. Ya. Trifonov, Nonlinear waves on the surface of a falling liquid film. Part 2. Bifurcations of the first-family waves and other types of nonlinear waves, J. Fluid Mech. **244**, 149 (1992).

[34] J. Liu, Nonlinear dynamics of wavy film flows, Ph.D. Thesis, University of Pennsylvania (1994), available through University Microfilms, Inc.

[35] T. R. Salamon, R. C. Armstrong, and R. A. Brown, Traveling waves on vertical films: Numerical analysis using the finite element method, Phys. Fluids **6**, 2202 (1994).

[36] A. N. Kolmogorov, "The local structure of turbulence in incompressible viscous fluid for very large Reynolds number," Dokl. Acad. Nauk SSSR **30**, 301 (1941).

[37] A. M. Obukhov, J. Fluid Mech. **13**, 77 (1962).

[38] A. N. Kolmogorov, J. Fluid Mech. **13**, 82 (1962).

[39] B. Mandelbrot, J. Fluid Mech. **62**, 331 (1974).

[40] U. Frisch, P. L. Sulem, and M. Nelkin, J. Fluid Mech. **87**, 719 (1978).

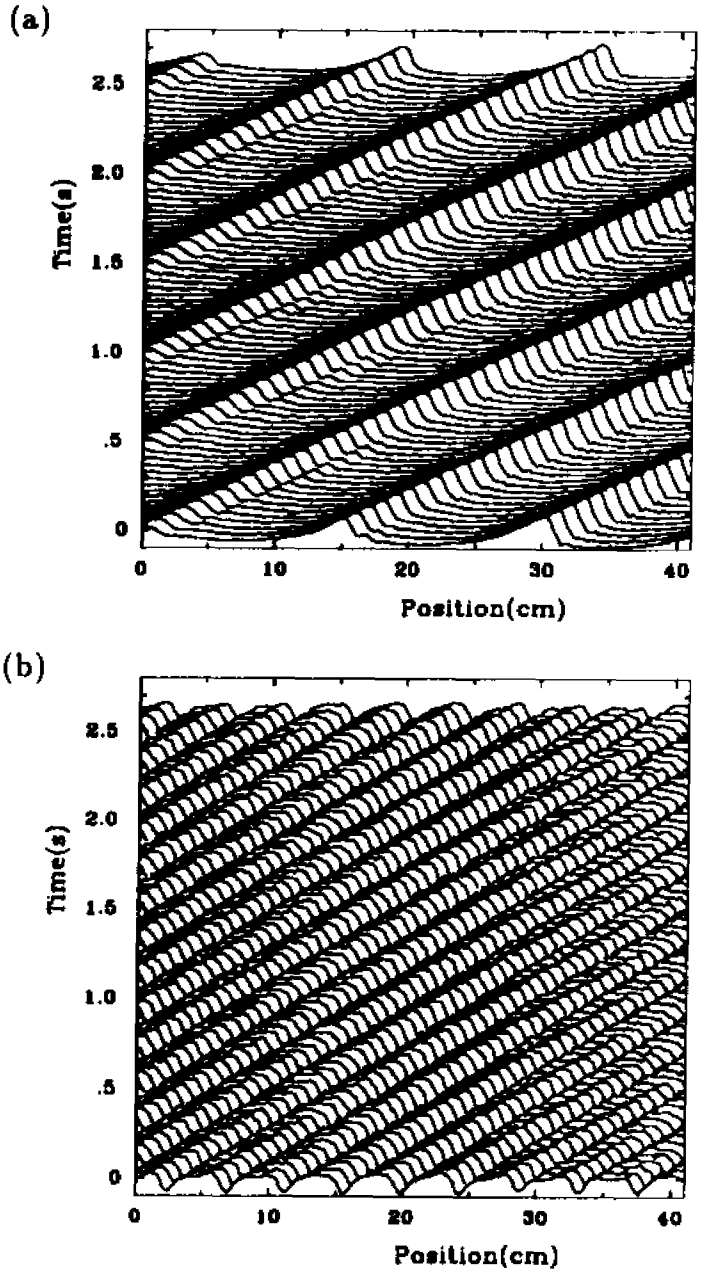

Figure 1.1: Space-time evolution of the film flow thickness for different perturbation frequencies. (a) $f = 2$Hz and $Re = 37.9$ the initial sinusoidal waves develop to solitary waves. (b) $f = 5$Hz and $Re = 30.3$ the primary wave fronts are close together.

Chapter 2

Space-Time Analysis

When analyzing a function, it is often convenient to expand the latter in terms of basis modes adapted to the symmetry of the function considered. Two classical examples are furnished by the Fourier analysis, convenient for expanding periodic functions, and the expansion into Bessel functions, often used in cylindrical geometry. A more general approach is to seek a set of modes which necessarily adapts itself to the symmetry of the function considered. Biorthogonal decompositions (BOD), which are considered at the beginning of this chapter, achieve this goal in space and time [2] by introducing linear operators defined from the function itself.

In this linear operator framework space-time symmetries, which incorporate the powerful techniques of group theory, are naturally introduced. In the present chapter I consider three examples of such symmetries. The first one consists of the group of space-time translations, a group particularly useful for traveling waves. The second symmetry group arises from the consideration of space-time modulations of a given (referential) dynamics. The latter will be fundamental in the study of signal discretization in the BOD framework (Chapter 3). It will also lead to a model of the coalescence and splitting of wave fronts observed in the film flow experiment when

modulated traveling waves are assumed (Chapter 4). Finally, the group of dilations (in space-time) will be crucial in modeling inhomogeneous turbulence in general and turbulent channel flow in particular (Chapter 5).

2.1 Biorthogonal decompositions

Such decompositions [1] consist in expanding the dynamics $u(x,t)$ considered into spatial and temporal orthogonal modes in $\mathcal{H}(X)\oplus\mathcal{H}(T)$ ($x \in X$, and $t \in T$) for which there is an isomorphic correspondence between the spatial and temporal modes. Here $\mathcal{H}(X)$ and $\mathcal{H}(T)$ are appropriate Hilbert spaces of spatial and temporal functions respectively. Such expansions correspond to the spectral decomposition of the self-adjoint matrix operator

$$\mathbf{V} = \begin{pmatrix} O & U^* \\ U & O \end{pmatrix}, \tag{2.1}$$

which acts on $\mathcal{H}(X) \oplus \mathcal{H}(T)$ where O is the null operator, and U the linear operator from $\mathcal{H}(X)$ to $\mathcal{H}(T)$ defined as

$$\forall\, \varphi \in \mathcal{H}(X),\ (U\varphi)(t) = \int_X u(x,t)\varphi(x)dm(x) \tag{2.2}$$

with $dm(x)$ the measure defining the scalar product in $\mathcal{H}(X)$. U^* is the adjoint operator of U. Clearly from the definition (2.2), the obtained modes are associated with $u(x,t)$ itself. If the space-time domain is discretized, then $u(x_j,t_i)$ can be seen as a matrix, and the operator $\mathbf{V}$ takes the form

$$\begin{pmatrix} O & u(x_i,t_j) \\ u(x_j,t_i) & O \end{pmatrix}.$$

When the spectrum of eigenvalues of $\mathbf{V}$ is discrete (the treatment of a continuous spectrum is also possible [3]), then the eigenvalue/eigenfunction problem can be writ-

ten as

$$\mathbf{V}\Phi_n = A_n\Phi_n,$$

or, equivalently,

$$U\varphi_n = A_n\psi_n \tag{2.3a}$$

$$U^*\psi_n = A_n\varphi_n \tag{2.3b}$$

where the eigenvectors of $\mathbf{V}$ are $\Phi_n = \begin{pmatrix}\varphi_n \\ \psi_n\end{pmatrix}$. The previous spectral decomposition permits a *biorthogonal* expansion of the flow into spatial modes of $\mathcal{H}(X)$ and temporal orthogonal modes of $\mathcal{H}(T)$:

$$u(x,t) = \sum_{n=1}^{N} A_n\varphi_n(x)\psi_n(t), \tag{2.4}$$

with

$$A_1 \geq A_2 \geq \ldots \geq A_N > 0\ ,$$

and

$$\langle\varphi_n|\varphi_m\rangle_{\mathcal{H}(X)} = \langle\psi_n|\psi_m\rangle_{\mathcal{H}(T)} = \delta_{n,m}\ .$$

The brackets denote the scalar products in $\mathcal{H}(X)$ and $\mathcal{H}(T)$, respectively. The spatial functions φ_n are called *topos* and the temporal functions ψ_n *chronos*. When some eigenvalues are degenerate, such functions are not unique, nor is the decomposition (2.4). The topos φ_n and the chronos ψ_n are related by an isomorphism given by the operator U itself, $U\varphi_n = A_n\psi_n$. The choice of the Hilbert spaces $\mathcal{H}(X)$ and $\mathcal{H}(T)$ depends on the particular situation. For data analysis purposes, $\mathcal{L}^2(X)$ and $\mathcal{L}^2(T)$ can always be used, but other choices may be more convenient and/or necessary, in

particular when the operator U is an unbounded operator, possibly with a singular kernel (see [3]).

The spatio-temporal dynamics can then be studied in the characteristic space $\mathcal{X}(T) = Ker(U^*)^\perp$ spanned by the chronos and the characteristic space $\mathcal{X}(X) = Ker(U)^\perp$ spanned by the topos. These spaces are the equivalents of the notion of phase space in temporal dynamical systems theory since the orbit η_x (described as x varies) in $\mathcal{X}(T)$ is defined as

$$\forall\, t \in T,\ \eta_x(t) = h(x,t), \tag{2.5}$$

and, similarly, the orbit ξ_t (described as t varies) in $\mathcal{X}(X)$ is defined as

$$\forall\, x \in X,\ \xi_t(x) = h(x,t)\,. \tag{2.6}$$

In addition, the subspace $\mathcal{X}(T)$ (resp. $\mathcal{X}(X)$) is the smallest linear subspace of $\mathcal{H}(X)$ (resp. $\mathcal{H}(T)$) that contains the orbit η_x (resp. ξ_t) and these subspaces, related by the isomorphism U, have the same dimension N.

It is conventional to define a global quantity, the entropy, by

$$H = -\frac{1}{\ln N}\sum_{n=1}^{N} p_n \ln p_n, \tag{2.7}$$

where $p_n = A_n^2 / \sum_{j=1}^{N} A_j^2$. The entropy H describes the distribution of the eigenvalue squares along the spectrum, or equivalently the distribution of the energy (in the sense of the norms of the Hilbert spaces $\mathcal{H}(X)$ and $\mathcal{H}(T)$) among the biorthogonal terms of (2.4). Such a global quantity can be used to detect spatio-temporal changes and bifurcations [1, 4].

When the norms used are the $\mathcal{L}^2$-norm, the spectral decomposition of the operator U^*U (acting on $\mathcal{H}(X)$), coincides with the probability theory tool called the proper orthogonal decomposition (POD), Karhunen-Loeve expansion or principal component

analysis [5, 6], when the (statistical) averaging procedure in the latter is the time average. Then, the problem reduces to

$$(U^*U)\varphi_n = A_n^2\varphi_n \ , \tag{2.8}$$

where U^*U is the spatial two-point correlation operator whose kernel is

$$R(x,x') = \int_T u(x,t)u(x',t)dm(t).$$

In this analogy, the data need to be measured at multiple positions instantaneously (which is not necessarly the case for the POD). The application of the POD to turbulence was first proposed and developed by Lumley [7, 8]. It was used in a dynamical systems perspective in [9, 10, 11] to explain intermittency in the wall region of a turbulent boundary layer, and has been applied to a large number of flows (see [12, 13] and references therein). Similarly, the decomposition of the temporal two-point correlation reads

$$(UU^*)\psi_n = A_n^2\psi_n \ , \tag{2.9}$$

where UU^* is the spatial two-point correlation operator whose kernel is

$$L(t,t') = \int_X u(x,t)u(x,t')dm(x).$$

Briefly the difference between the spectral decompositions of the operators UU^* and/or U^*U and the spectral decomposition of $\mathbf{V}$, is that the latter maintains the one-to-one correspondence between space and time, which is not the case for the former. In other words, the dynamics $u(x,t)$ is uniquely defined from the operator $\mathbf{V}$ and its spectral analysis, which is not the case when the operators UU^* and/or U^*U are considered: one can find all space-time functions which have the same correlations, namely all operators U for which UU^* and/or U^*U coincide [14].

2.2 Space-time symmetries

Space-time *symmetries* are introduced in the biorthogonal decompositions context [2] in terms of a commutation relation between the matrix operators

$$\mathbf{VS} = \gamma \mathbf{SV} \ , \tag{2.10}$$

with $\gamma \in \mathbf{R}$, $\mathbf{V}$ being defined as in (2.1), and

$$\mathbf{S} = \begin{pmatrix} S & O \\ O & \tilde{S} \end{pmatrix},$$

acting on $\mathcal{H}(X) \oplus \mathcal{H}(T)$. The pair of operators, S acting on $\mathcal{H}(X)$ and $\tilde{S}$ acting on $\mathcal{H}(T)$, defines a *spatio-temporal symmetry*.

2.2.1 Space-time translations

Consider now a function invariant under the group of translations in two variables, that is a wave traveling at constant velocity c

$$h_0(x - x_0, t) = h_0(x, t + t_0) \tag{2.11}$$

for all $x, x_0 \in X$, $t, t_0 \in T$ such that $x_0 + ct_0 = 0$.

In this case (see [2]), the symmetry operators are regular representations of the group of real numbers $\mathbf{R}$, namely translations:

$$(S_{x_0}\varphi)(x) = \varphi(x - x_0)$$

$$(\tilde{S}_{t_0}\psi)(t) = \psi(t - t_0)$$

such that $x_0 + ct_0 = 0$; the matrix symmetry operator is then

$$\mathbf{R_0} = \begin{pmatrix} S_{x_0} & O \\ O & \tilde{S}_{t_0} \end{pmatrix},$$

so that $\mathbf{V}\mathbf{R}_0 = \mathbf{R}_0\mathbf{V}$. The spectrum of $\mathbf{V}$ is then degenerate of order two and a set of topos and chronos can be identified with Fourier modes.

2.2.2 Space-time modulations

A possible route toward space-time complexity as a control parameter varies consists of modulations of an original state of the system $h_0(x,t)$,

$$h_{mod}(x,t) = g_1(x)g_2(t)h_0(x,t)\ ,$$

where $g_1(x)$ is a spatial modulation and $g_2(t)$ is a temporal modulation, both bounded and real functions. The consideration of spatial as well as temporal modulations seems natural from a spatio-temporal viewpoint. Such a scenario can be seen as a consequence of nonlinear interactions. Spatially and temporally modulated dynamics $h_{mod}(x,t)$ have been compared with the reference dynamics $h_0(x,t)$ by means of biorthogonal decompositions in [15]. I summarize here some results particularly relevant to the present work.

The introduction of the operators G_1 acting on $\mathcal{H}(X)$ such that $[G_1(\varphi)](x) = g_1(x)\varphi(x)$, and G_2 acting on $\mathcal{H}(T)$ such that $[G_2(\psi)](t) = g_2(t)\psi(t)$, permits a description of the dynamics $h_{mod}(x,t)$ in terms of the reference dynamics $h_0(x,t)$. The matrix dynamic operator $\mathbf{V}_{mod}$ of $h_{mod}(x,t)$ can be written as the product $\mathbf{V}_{mod} = \mathbf{G}\,\mathbf{V}_0\,\mathbf{G}$, where $\mathbf{V}_0$ is the matrix operator corresponding to $h_0(x,t)$, and $\mathbf{G}$ is

$$\mathbf{G} = \begin{pmatrix} G_1 & O \\ O & G_2 \end{pmatrix}.$$

The orbits described by the vectors ξ_t^{mod} and η_x^{mod} in the spatial and temporal characteristic spaces $\mathcal{X}_{mod}(X)$ and $\mathcal{X}_{mod}(T)$ are expressed in terms of the reference dynamics in $\mathcal{X}_0(X)$ and $\mathcal{X}_0(T)$ by

$$\xi_t^{mod} = g_2(t)G_1\xi_t^0, \tag{2.12}$$

and

$$\eta_x^{mod} = g_1(x) G_2 \eta_x^0. \tag{2.13}$$

The action of the operator G_1 in (2.12) corresponds to a change of coordinates in $\mathcal{H}(X)$ which conserves the dimension [15] but not the orthogonality. In this new coordinates system, the dynamics is, of course, topologically unchanged. It corresponds to a stretching and a rotation of the original phase space dynamics. Once the orbit has been globally deformed by the action of G_1, the new orbit $\{\xi_t^{mod},\ t \in T\}$ undergoes a temporal modulation $g_2(t)$ with respect to the reference orbit $\{\xi_t^0,\ t \in T\}$. A similar geometrical description can be given for the orbit $\{\eta_x^{mod},\ x \in X\}$.

The above modulations not only affect the phase space dynamics, but also have a significant impact on the original symmetries. The extent of change have been fully analysed in [15]. It has been proven that under the non-resonant condition (NR) and the local isotropy condition (LI), the original symmetries get deformed but not broken, in a sense that will be made clear below. The NR condition can be mathematically expressed in the form:

$$[\mathbf{V_0 G^2 V_0}, \mathbf{V_0}] = \mathbf{0}\ , \tag{2.14}$$

where $[A, B] = AB - BA$ denotes the commutator of A and B. It basically means that the "sidebands" created in each eigenspace of $\mathbf{V_0}$ by the action of $\mathbf{G}$ do not intersect. Even if this commutation relation is satisfied, the action of G may still break some degeneracies present in $\mathbf{V_0}$. This effect can be avoided by imposing the following LI condition: *for each n, there exists a unique pair of real numbers* $(c_k, \tilde{c}_k)$ *such that*

$$\forall \varphi_n^0 \in P_n^0 \mathcal{X}_0(X),\ \ \|G_1 \varphi_n^0\| = c_k \|\varphi_n^0\|\ , \tag{2.15a}$$

and

$$\forall \psi_n^0 \in \tilde{P}_n^0 \mathcal{X}_0(T), \quad \|G_2 \psi_n^0\| = \tilde{c}_k \|\psi_n^0\| . \tag{2.15b}$$

The operators, P_n^0 and $\tilde{P}_n^0$ are the projectors onto the spatial and temporal eigenspaces in $\mathcal{X}_0(X)$ and $\mathcal{X}_0(T)$ associated with the eigenvalue A_n^0.

The above (2.14) and (2.15) conditions guarantee that the images of the eigenspaces of $\mathbf{V_0}$ by the modulation operator **G** are invariant. Therefore $\mathbf{V_{mod}}$ maintains a block structure and satisfies the symmetry

$$\mathbf{T V_{mod}} = \mathbf{V_{mod} T} . \tag{2.16}$$

Here **T** denotes the matrix operator

$$\mathbf{T} = \begin{pmatrix} T & O \\ O & \tilde{T} \end{pmatrix},$$

where

$$T = \sum_k P_k T_k P_k ,$$

$$\tilde{T} = \sum_k \tilde{P}_k \tilde{T}_k \tilde{P}_k ,$$

and

$$T_k = G_1^{-1} S_{x_k} G_1 ,$$

$$\tilde{T}_k = G_2 \tilde{S}_{t_k} G_2^{-1} .$$

In this case, the topos and chronos of $\mathbf{V_{mod}}$ are the modulations of the topos and chronos of $\mathbf{V_0}$,

$$\varphi_n^{mod} = \frac{1}{c_n} G_1 \varphi_n^0, \tag{2.17a}$$

$$\psi_n^{mod} = \frac{1}{\tilde{c}_n} G_2 \psi_n^0, \tag{2.17b}$$

and

$$A_n^{mod} = c_n \tilde{c}_n A_n^0 \,. \tag{2.17c}$$

The operator $\mathbf{T}$ thus acts on each eigenspace differently. However, it is interesting to note that, independently of the non-resonant or resonant condition, $\mathbf{V_{mod}}$ intertwines $(\mathbf{T}^{-1})^*$ and $\mathbf{T}$, so that $(\mathbf{T}^{-1})^* \mathbf{V_{mod}} = \mathbf{V_{mod}} \mathbf{T}$. For the resonant case, $(\mathbf{T}^{-1})^*$ may be different from $\mathbf{T}$ and the symmetry may no longer hold. The loss of the space-time symmetry in the sense of the commutation relation (2.10) is due to the fact that, in general, $\mathbf{T}$ is not a unitary operator. Under the (2.14) and (2.15) conditions, $\mathbf{T}$ becomes unitary. The intersection of the spatial and/or temporal sidebands, under the resonant condition, creates spatio-temporal resonances which couple the equations of the biorthogonal decomposition, so that the block structure of the reference dynamic operator is not maintained. This is equivalent to a rotation of the topos in $\mathcal{X}_0(X)$ and a rotation of the chronos in $\mathcal{X}_0(T)$.

Consider now a particular case in which the original dynamic function is a travelling wave of constant speed c, say $h_0(x,t) = g_0(x-ct)$. Also assume that the dynamics of $h_{mod}(x,t)$ and $h_0(x,t)$ are defined in a finite space-time domain $X \times T$, such that the lengths of the intervals $|X|$ and $|T|$ satisfy $N|X| = cM|T|$, where N and M are integers, and $g_1(x)$, $g_2(t)$ are periodic with periods $|X|$ and $|T|$, respectively. I can then decompose g_0, g_1 and g_2 into Fourier series such that

$$g_0(x-ct) = \sum_k g_0^k e^{i2\pi k(x-ct)M/|X|} \,,$$

$$g_1(x) = \sum_l g_1^l e^{i2\pi lx/|X|} \,,$$

$$g_2(t) = \sum_m g_2^m e^{-i2\pi mt/|T|} \,,$$

and the modulated dynamics $h_{mod}(x,t)$ can be decomposed as

$$h_{mod}(x,t) = \sum_{k,l,m} g_0^k \, g_1^l \, g_2^m \, e^{i2\pi(Mk+l)x/|X|} \, e^{-i2\pi(Nk+m)t/|T|}. \tag{2.18}$$

Although it is clear from (2.18) that the modulation increases the number of Fourier modes, as mentioned before, the number of topos and chronos (2.4) of the modulated function is *smaller than or equal to* that of the non-modulated function. The terms $Mk+l$ and $Nk+m$ in (2.18) express the interactions between the Fourier modes of g_0, g_1, and g_2. The terms containing $Mk+l$, for fixed k and all l, and those containing $Nk+m$ for fixed k and all m, are often referred to as *sidebands* in the literature when l and m are small. Various sidebands correspond to various wavenumbers k and frequencies l. Whether the wavenumbers and frequencies of the modulations are small or not, I keep this terminology and refer to *spatial and temporal sidebands*. For this particular case, the above NR condition (2.14) can be re-formulated saying that: g_1 is *non-resonant* with respect to g_0 if,

$$\forall\, k,k' \in \mathcal{K}\ (k \neq k'),\ \text{and}\ \forall\, l,l' \in \mathcal{L}\ (l \neq l'),\qquad Mk+l \neq Mk'+l'\ , \tag{2.19}$$

and *resonant* otherwise. Similarly, I say that g_2 is *non-resonant* with respect to g_0 if,

$$\forall\, k,k' \in \mathcal{K}\ (k \neq k'),\ \text{and}\ \forall\, m,m' \in \mathcal{M}\ (m \neq m'),\qquad Nk+m \neq Nk'+m'\ , \tag{2.20}$$

and *resonant* otherwise. Here, $\mathcal{K}$, $\mathcal{L}$, and $\mathcal{M}$ are the sets of integers k, l, and m, for which the corresponding Fourier coefficients of g_0, g_1, and g_2 are non-zero, respectively.

It has been proved [15] that, in the non-resonant conditions (2.19) and (2.20), the local isotropy condition is also true in a global sense. The c_n and $\tilde{c}_n$ are independent of n. For every set of topos and chronos decomposing h_0, the corresponding set of modulated spatial and temporal functions

$$\varphi_n^{mod}(x) = \frac{1}{c} g_1(x) \varphi_n^0(x), \tag{2.21a}$$

and

$$\psi_n^{mod}(t) = \frac{1}{\tilde{c}} g_2(t)\psi_n^0(t), \tag{2.21b}$$

is a set of topos and chronos decomposing h_{mod}. Recall that, since h_0 is a uniformly traveling wave, there is always a set of topos and chronos that coincides with Fourier modes, i.e. $\varphi_n^0(x) \sim e^{i2\pi Mknx/|X|}$ and $\psi_n^0(t) \sim e^{i2\pi Nkt/|T|}$. Moreover, the (normalized) biorthogonal spectra of the modulated and non-modulated traveling waves stay the same. In particular, the spectrum stays degenerate of order two and $h_{mod}(x,t)$ still satisfies a space-time symmetry.

Finally, suppose that the modulation functions g_1 and g_2 are wavenumber dependent and the non-resonant condition still holds. In this case, both the symmetry and the expression (2.21a), (2.21b) of the topos and chronos are still valid if g_1 and g_2 are respectively replaced by g_1^k and g_2^k. However, the normalized spectrum is no longer invariant under the action of the modulation.

2.2.3 Space-time dilations

The Navier-Stokes equations (1.1) are invariant under the following scale transformation

$$\begin{aligned} \boldsymbol{x} &\longrightarrow \lambda \boldsymbol{x} \\ t &\longrightarrow \lambda^{1-h} t \\ \nu &\longrightarrow \lambda^{1+h} \nu \\ \boldsymbol{u} &\longrightarrow \lambda^{h} \boldsymbol{u} \end{aligned} \tag{2.22}$$

for all $\lambda \in \mathbf{R}_{>0}$ and $h \in \mathbf{R}$. Although this invariance does not mean that all solutions of the Navier-Stokes equations are self-similar under the above transformations, it is reasonable to assume that fluid flows, in a certain "inertial" range of their spectrum, do satisfy such a scale invariance in their fully developed turbulent regime [3, 17]. I

thus consider a function with the following symmetry

$$\boldsymbol{u}(\boldsymbol{x},t) = \lambda^h \boldsymbol{u}(\lambda^{-1}\boldsymbol{x}, \lambda^{h-1}t), \quad \forall\, \boldsymbol{x} \in \mathbf{R}^3, t \in \mathbf{R}. \tag{2.23}$$

For the sake of simplicity, I now consider the stretching of one component of the velocity, say $u(x,t)$, in one spatial direction (the generalization to full three-dimensionality is straightforward but makes the notation more complex [18]). The operator commutation relation (2.10) is then rewritten in the case of (2.23) ([2, 3]) as

$$\mathbf{V}\mathbf{S}_\lambda = \lambda^h \mathbf{S}_\lambda \mathbf{V}. \tag{2.24}$$

and the symmetry operators are the spatial and temporal dilations

$$(S_\lambda \varphi)(x) = \varphi(\lambda^{-1}x), \tag{2.25a}$$

$$(\tilde{S}_\lambda \psi)(t) = \psi(\lambda^{-(1-h)}t). \tag{2.25b}$$

This implies that there are self-similar families for which the spectrum of eigenvalues A_n is exponentially decaying

$$A_n = (\lambda^h)^{N-n} A_N \tag{2.26}$$

and all the modes φ_n and ψ_n are images of two basic functions φ_N and ψ_N by the action of S_λ and $\tilde{S}_\lambda$:

$$\varphi_n = (S_\lambda)^{N-n} \varphi_N, \tag{2.27a}$$

$$\psi_n = (\tilde{S}_\lambda)^{N-n} \psi_N, \tag{2.27b}$$

where N denotes the index of the last mode within the family. The sequence generated by equations (2.26) and (2.27) leads to a hierarchy of modes [3].

The existence of a space-time symmetry (2.10) (including the case where $\gamma = 1$) implies statistical symmetries, in the sense that S can be seen at the level of the spatial correlation (2.8), and, similarly, $\tilde{S}$ can be seen at the level of the temporal correlation (2.9). This property is due to the commutation relation of U^*U with S and the commutation of UU^* with $\tilde{S}$, in the sense that

$$S^{-1}U^*US = \gamma^2 U^*U, \tag{2.28a}$$

$$\tilde{S}^{-1}UU^*\tilde{S} = \gamma^2 UU^*, \tag{2.28b}$$

which are direct consequences of (2.10). Conversely, we can now suppose that a spatial (statistical) symmetry is detected at the level of the spatial correlations. In this case, there exists a spatio-temporal symmetry $(S, \tilde{S})$ satisfied by the flow itself. The same remark is true if a temporal (statistical) symmetry exists for the temporal correlations. Statistical symmetries thus reflect the presence of deterministic symmetries [3, 14]. In the statistical context of the POD, symmetries are sometimes included in the "ensemble average" needed to compute the correlations. This was proposed to enlarge the statistical ensemble of data [12]. Such a technique is not adapted to the present purpose since it does not permit the detection of the symmetries satisfied by the flow. Moreover, it would lead to the systematic (artificial) scaling of the *entire* spectrum.

The fact that the correlation operators U^*U and UU^* possess the symmetries (2.28) implies that their spectral decomposition consist of hierarchical collections of modes in the sense of (2.26) and (2.27). In particular, for the case of the spatial correlation, we have

$$A_n^2 = (\lambda^{2h})^{N-n} A_N^2, \tag{2.29}$$

and

$$\varphi_n = (S_\lambda)^{N-n} \varphi_N. \tag{2.30}$$

Such a generation of eigenvalues and eigenvectors from a basic one is a well-known feature of the spectral decomposition of linear operators which are invariant under a Lie group. The harmonic oscillator and angular momentum are well-known examples from elementary Quantum Mechanics having similar properties. Returning to the dilation symmetry (2.23), it is formally valid in case of infinite boundary conditions. The effect of the presence of finite boundary conditions is unknown and will be investigated in Chapter 5. This question is fundamental for understanding the structure of bounded flows. Some deformation of (2.23) is expected.

When various symmetry groups are present in the flow, the above formalism is easily extended. Each symmetry defines invariant subspaces in $\mathcal{H}(X) \oplus \mathcal{H}(T)$ on which the other symmetries act. Suppose, for example, that, in addition to (2.23), the flow possesses a spatial reflection symmetry. Because the reflection group has two irreducible representations of character one, $Ker(\mathbf{V})^{\perp}$ is split into two subspaces invariant under the spatial reflection symmetry operator, thus satisfying (2.10) with $\gamma = 1$. In other words, in one (space) dimension, there is always a set of topos which are either odd or even. The subspace spanned by odd (resp. even) topos satisfies the dilation symmetry (2.27a) [18].

References for Chapter 2

[1] N. Aubry, R. Guyonnet, and R. Lima, Spatio-temporal analysis of complex signals: theory and applications, J. Stat. Phys. **64**, 683 (1991).

[2] N. Aubry, R. Guyonnet, and R. Lima, Spatio-temporal symmetries and bifurcations via biorthogonal decompositions. J. Nonlinear Sci. **2**, 183 (1992).

[3] N. Aubry, R. Guyonnet and R. Lima, "Turbulence Spectra," J. Stat. Phys. **67**, 203 (1992).

[4] P. Kolodner, S. Slimani, N. Aubry and R. Lima, Characterization of dispersive chaos and related states of binary-fluid convection, Physica D **85**, 165 (1995).

[5] K. Karhunen, "Zur spektral theorie stochatischer prozesse," Ann. Acad. Sci. Fennicae Ser. A **1**, 34 (1944).

[6] M. Loeve, "Probability Theory," Van Nostrand, New York (1955).

[7] J. L. Lumley, The structure of inhomogeneous turbulent flows, in: Atmospheric turbulence and radio wave propaganon, eds. A.M. Yaglom and V.I. Tatarski:, Moscow: Nauka, 166 (1967).

[8] J. L. Lumley, Stochasnc Tools in Turbulence, Academic (1970).

[9] N. Aubry, P. Holmes, J. L. Lumley and E. Stone, The Dynamics of Coherent Structures in the Wall Region of a Turbulent Boundary Layer, J. Fluid Mech. **192**, 115 (1988).

[10] G. Berkooz, P. Holmes and J. L. Lumley, Intermittent dynamics in simple models of the wall layer, J. Fluid Mech. **230** 75 (1991).

[11] S. Sanghi and N. Aubry, Interaction mode models of near wall turbulence, J. Fluid Mech. **247**, 455 (1993).

[12] L. Sirovich. Turbulence and the dynamics of coherent structures: I, II, III Q. Appl. Maths **5**, 561 (1987).

[13] G. Berkooz, P. Holmes and J. L. Lumley, The proper orthogonal decomposition in the analysis of turbulent flows, Annu. Rev. Fluid Mech. **25**, 539 (1993).

[14] N. Aubry and R. Lima, "Spatio-temporal and statistical symmetries," J. Stat. Phys. **81**, 793 (1995). (1995).

[15] N. Aubry and R. Lima, "The dynamics of spatio-temporal modulations," Chaos **5**, 578 (1995).

[16] N. Aubry, F. Carbone, R. Lima, and S. Slimani, Wave propagation phenomena from a spatio-temporal viewpoint: resonances and bifurcations, J. Stat. Phys. **76**, 1005 (1994).

[17] U. Frisch, From Global (Kolmogorov 1941) scaling to local (multifractal) scaling in fully developed turbulence, Proc. Roy. Soc. **A**, (1991).

[18] N. Cao, "Analysis of reduced simulations of laminar/turbulent wake flows," Ph.D. thesis, Levich Institute, the City University of New York, New York, NY (1993).

Chapter 3

Discretely Sampled Data

Inherent to any numerical calculation or experimental measurement is the problem of discretization. Although the functions are assumed to be defined on a continuous domain, the signals are recorded on a discrete domain given by the mesh, the position of the probes, the acquisition frequency, etc. This problem, intrinsic to numerical analysis, cannot be avoided. Particularly when the discrete signal is analyzed, it is crucial to isolate the effect of the discretization. Obviously, we expect that the refinement of the grid will allow us to recover an increasing number of details present in the original function, i.e. improve the accuracy. This expectation, however, is not always met.

One can get an idea of the possible effects by using the discrete Fourier analysis. In this case, the lack of adequate resolution can make the observed Fourier transform erroneous, in which case the Fourier modes are *aliased*. The Nyquist [1] condition establishes the minimal sampling required to prevent aliasing from occurring. Only under such a condition, the discretized Fourier transform is simply the discretized version of the continuous (Fourier) transform. In this chapter I show that a similar criterion can be derived for biorthogonal decompositions. More precisely, I will prove

that there exists a minimal grid size required such that the BOD of the discretized function coincides with the discretization of the BOD of the continuous function. This chapter is organized as follows. I start by setting up the problem in the appropriate mathematical framework. I then consider the particular case of traveling waves before generalizing to any space-time function.

3.1 The Mathematical Problem

Consider a space-time function $u(x,t)$ defined on the space-time domain $X \times T$. As in Chapter 2, the $\mathcal{L}^2(X)$ and $\mathcal{L}^2(T)$ Hilbert spaces are used for the numerical implementation of the biorthogonal decomposition. I now assume that, as it is usually the case for most experimental data and many numerical computations, the space-time signal describing $u(x,t)$ is sampled over a uniform spatio-temporal mesh (x_i, t_k), such that

$$x_i = \Delta i, \quad 1 \leq i \leq NX \tag{3.1}$$

and

$$t_k = \tau k, \quad 1 \leq k \leq NT \tag{3.2}$$

where NX and NT denote the number of discretized points in space and time respectively, $\Delta = |X|/NX$, $\tau = |T|/NT$, and $|X|$ and $|T|$ refer to the size of the space and time domains.

I now show that the values of the sampling frequencies in space and time, $1/\Delta$ and $1/\tau$, are critical for the correct interpretation and understanding of $u(x,t)$ through its discretized version $u(x_i, t_k)$. For this purpose, we write the discretized function in terms of Dirac delta functions, i.e.

$$d_1(x)d_2(t)u(x,t)\ ,$$

with

$$d_1(x) = \sum_{i=1}^{NX} \delta(x - x_i) \ , \tag{3.3}$$

and

$$d_2(t) = \sum_{k=1}^{NT} \delta(t - t_k) \ . \tag{3.4}$$

It is then clear that the problem is equivalent to modulating $u(x,t)$ with the particular spatial and temporal modulations (3.3) and (3.4). In Section 2.2.2, it was shown that, as proven in Reference [2], under the *non-resonant* condition (2.14) and the *local isotropy* condition (2.15), the symmetries of the modulated signal get deformed but not broken, and the topos and chronos are the modulated topos and chronos of the reference dynamics. In the present situation, it is thus fundamental to determine a criterion which guarantees the non-resonant and local isotropy conditions, in which case we can find a set of topos and chronos of the discretized function which are simply the discretized topos and chronos of the continuous signal. Otherwise, a major distortion, due to a rotation in phase space (described earlier in Section 2.2.2), will occur in the resulting eigenmodes of equation (2.3) where $u(x_i, t_k)$ rather than $u(x,t)$ is used.

In what follows, unless otherwise noticed, I assume that the size of the X and T domains, ($|X|$ and $|T|$), are large enough compared with the characteristic length and time scales of the analyzed function such that the terms of order $\mathcal{O}(1/|X|)$ and $\mathcal{O}(1/|T|)$ can be neglected (see Fig. 3.1). The mathematical reason for such an assumption will be clear in the next sections.

3.2 Case of a Uniform Traveling Wave

In this section I consider the case of $u(x,t)$ being a uniform traveling wave moving at constant speed c, that is $u(x,t) = g(x - ct)$. The following general lemma will be useful:

Lemma 3.1 *The decomposition*

$$u(x,t) = \sum_k \beta_k f_k(x) e_k(t)$$

is the biorthogonal decomposition of u if and only if the sets $\{f_k\}_{k\in\mathbf{N}}$ and $\{e_k\}_{k\in\mathbf{N}}$ are orthonormal functions and $\{\beta_k\}_{k\in\mathbf{N}}$ is a sequence of strictly positive numbers.

Proof: The first implication is trivial. Conversely, supposing that the f_k's and e_k's are orthonormal, we now show that they are eigenvectors of the operator U. Using the definition of the latter (2.2) and the orthonormality hypothesis, we can write

$$\begin{aligned} Uf_n(x) &= \int_X \sum_k \beta_k f_k(x) e_k(t) f_n(x) dm(x) \\ &= \beta_n e_n(t) , \end{aligned}$$

and, similarly

$$U^* e_n(t) = \beta_n f_n(x).$$

Since $\beta_k > 0\ \forall n \in \mathbf{N}$, then the f_k's and e_k's are solutions of the biorthogonal equations (2.3).

Q.E.D.

Proposition 3.2 *Let $u(x,t) = g(x - ct)$ be a uniformly traveling wave defined on $X \times T$ complete domains such that the lengths of the intervals $|X|$ and $|T|$ satisfy*

$N|X| = cM|T|$, where N and M are integers. Let (x_i, t_k) $i,k \in \mathbf{N}$ be a uniform spatio-temporal mesh defined by equations (3.1) and (3.2). If d_1 and d_2 are defined as (3.3) and (3.4), and k_{max} is the largest integer for which the k-th Fourier coefficient g is non-zero, then the following conditions are equivalent:

i. the BOD of $d_1(x)d_2(t)u(x,t)$ is the discretization of the BOD of u

ii. $d_1(x)d_2(t)u(x,t)$ is non-resonant

iii. $\frac{Mk_{max}}{|X|} \leq \frac{1}{2\Delta}$ *and* $\frac{Nk_{max}}{|T|} \leq \frac{1}{2\tau}$.

Proof: Since the functions d_1 and d_2 are periodic, Fourier modes are the natural basis. The Fourier transform of the modulations (3.3) and (3.4) are given by the expressions

$$d_q^1 = \begin{cases} 1/|X| & \text{if } q \neq l\,NX \\ 1/\Delta & \text{if } q = l\,NX \end{cases} \tag{3.5a}$$

and

$$d_p^2 = \begin{cases} 1/|T| & \text{if } p \neq m\,NT \\ 1/\tau & \text{if } p = m\,NT. \end{cases} \tag{3.5b}$$

As stated before I neglect, in (3.5a) and (3.5b), the Fourier coefficients whose values are $1/|X|$ and $1/|T|$ corresponding to wavenumbers and frequencies which are not multiple numbers of NX or NT. I recall from Chapter 2 equation (2.18) which becomes

$$u(x,t)d_1(x)d_2(t) = \sum_{k,l,m} \frac{g^k}{\Delta\tau}\, e^{i2\pi(Mk+l\,NX)x/|X|} e^{-i2\pi(Nk+m\,NT)t/|T|} \tag{3.6}$$

for this particular case. In virtue of Lemma 3.1, the above decomposition (3.6) is the BOD of $u(x,t)d_1(x)d_2(t)$ if and only if the sets $e^{i2\pi(Mk+l\,NX)x/|X|}$ and $e^{-i2\pi(Nk+m\,NT)t/|T|}$ are orthonormal sets of functions, or, equivalently, if the spatial wavenumbers $Mk + l\,NX$

(resp. the temporal sidebands $Nk + m\,NT$) do not coincide for any pair of (k, l) (resp. (k, m)). This is fulfilled if and only if

$$\frac{Mk + l\,NX}{|X|} = \frac{Mk' + l'\,NX}{|X|} \Longleftrightarrow k = k', l = l' \ ,$$

and

$$\frac{Nk + m\,NT}{|T|} = \frac{Nk' + m'\,NT}{|T|} \Longleftrightarrow k = k', m = m' \ ,$$

which are precisely the non-resonant conditions (2.19) and (2.20). By rewriting the spatial term, we obtain

$$\frac{M(k - k')}{|X|} = \frac{(l' - l)}{\Delta} \Longleftrightarrow k = k', l = l' \ . \tag{3.7}$$

If k_{max} is the largest integer k for which g^k is non- zero, it follows that a necessary and sufficient condition for spatial non-resonance is

$$\frac{M\ 2k_{max}}{|X|} < \frac{|l' - l|}{\Delta} \ .$$

A similar expression for the temporal non-resonant condition can be derived in the same manner. The non-resonant conditions are thus fulfilled if and only if

$$\frac{Mk_{max}}{|X|} \leq \frac{1}{2\Delta} \qquad and \qquad \frac{Nk_{max}}{|T|} \leq \frac{1}{2\tau} \ . \tag{3.8}$$

Q.E.D.

Remark 3.3 If the terms of order $\mathcal{O}(1/|X|)$ and $\mathcal{O}(1/|T|)$ had not been neglected, all terms would have been resonant, but the energy content and therefore the influence of such terms would have been rather insignificant (see Fig. 3.1).

Remark 3.4 Equation (3.6) is general and shows all the possible Fourier components of $u(x,t)d_1(x)d_2(t)$, whether they are resonant or not.

Example: Before generalizing the previous result, let us consider a simple example illustrating our point. Suppose the following traveling wave:

$$u(x,t) = \cos[2\pi(.17x - 5t)] + .6\cos[2\pi(.34x - 10t)] \; . \tag{3.9}$$

For this case, we have

$$\frac{Mk}{|X|} = \begin{cases} \pm.17 \\ \pm.34 \end{cases} \quad \text{and} \quad \frac{Nw}{|T|} = \begin{cases} \pm 5 \\ \pm 10 \end{cases} \; .$$

If we take a spatial sampling wavenumber $1/\Delta = 12.12$ and a temporal sampling frequency $1/\tau = 30$, proposition 3.2 guarantees a faithful biorthogonal decomposition. In contrast, if we now fix $1/\Delta$ to the previous value and consider $1/\tau = 15$, then there should be resonant temporal terms since the temporal limit $1/2\tau$ is 7.5. The spatial sampling is well below the limit condition (3.8), therefore there is no need to worry about possible intersections of the spatial Fourier sidebands. Whether there are resonances or not can be clearly seen from Tables 3.1 and 3.2 below, in which the terms $Nw/|T| + m/\tau$ involved in expression (3.6) are explicitly given for this example. Note that, although there is no intersection between the spatial sidebands, the topos may still get deformed. In Table 3.1 in which $1/\tau$ is 30, the values in the different possible temporal sidebands do not coincide. There is no resonance. Instead, in Table 3.2 corresponding to $1/\tau = 15$, the appearance of equal values for different sidebands indicates that the latter intersect due to insufficient sampling. Figures 3.2 and 3.3 show the corresponding biorthogonal spectra, as well as topos and chronos in both their physical and Fourier representations. In Figure 3.2, the biorthogonal spectra display two pairs of degenerate eigenvalues (the remaining values being due to numerical noise). The topos and chronos associated with each pair of eigenvalues are single Fourier modes (with well defined waves numbers .17 and .34, and

m	$-10+m/\tau$	$-5+m/\tau$	$5+m/\tau$	$10+m/\tau$
-2	-70	-65	-55	-50
-1	-40	-35	-25	-20
0	-10	-5	5	10
1	20	25	35	40
2	50	55	65	70

Table 3.1: $1/\tau = 30$. All exponents are different.

m	$-10+m/\tau$	$-5+m/\tau$	$5+m/\tau$	$10+m/\tau$
-2	-40	-35	-25	-20
-1	-35	-20	-10	-5
0	-10	-5	5	10
1	5	10	20	35
2	20	25	35	40

Table 3.2: $1/\tau = 15$. There are resonant terms, some of the exponents coincide.

frequencies 5 and 10). When an insufficient temporal mesh size is used, the description is incorrect. More precisely, only one degenerate subspace (of dimension two) is obtained, and neither topos nor chronos are well defined. Consistently with Table 3.2, the frequencies 5 and 10 are resonant and both frequencies (resp. wavenumbers) appear in the Fourier representation of individual chronos (resp. topos) (see also Remark 3.4).

3.3 Case of a Generic Function

Note that the proof in the previous section is particular to a function whose topos and chronos are Fourier modes so that the NR conditions (2.19) and (2.20) can be applied. In order to extend it to *any* function, we need to go back to the more general non-resonant and local isotropy conditions (2.14) and (2.15). Note that the NR condition can be expressed in terms of the operators U and U^* as

$$U_0^* U_0 G_1^2 U_0^* = U_0^* G_2^2 U_0 U_0^* \ , \tag{3.10a}$$

and

$$U_0 U_0^* G_2^2 U_0 = U_0 G_1^2 U_0^* U_0 \ . \tag{3.10b}$$

Theorem 3.5 *Let $u(x,t)$ be defined on X and T complete domain of lengths $|X|$ and $|T|$ and let (x_i, t_k) $i,k \in \mathbf{N}$ be a uniform spatio-temporal mesh defined by equations* (3.1) *and* (3.2). *If d_1 and d_2 are defined as* (3.3) *and* (3.4), *and the pair (k_{max}, w_{max}) are the largest integers for which the spatial and temporal Fourier coefficients of g are non-zero, then $d_1(x)d_2(t)u(x,t)$ satisfies the non-resonant and local isotropy conditions* (2.14) *and* (2.15) *if and only if*

$$\frac{k_{max}}{|X|} \leq \frac{1}{2\Delta} \qquad \textit{and} \qquad \frac{w_{max}}{|T|} \leq \frac{1}{2\tau} \ . \tag{3.11}$$

Proof: It is sufficient to check conditions (2.19) and (2.20) for any basis of $\mathcal{X}(X) \otimes \mathcal{X}(T)$, in particular for the topos and chronos of the biorthogonal decomposition of $u(x,t)$. We then introduce $\varphi_n^a(x)$ and $\psi_n^a(t)$ such that

$$U\varphi_n^a = A_n \psi_n^a \ , \tag{3.12a}$$

$$U^*\psi_n^a = A_n \varphi_n^a \ , \tag{3.12b}$$

where α is a number labeling the possible degenerate eigenmodes, $\alpha = 1, \ldots, \alpha^n_{max}$.

Once again, the periodicity of the functions d_1 and d_2 makes the use of Fourier expansions natural and I neglect the terms of order $\mathcal{O}(1/|X|)$ and $\mathcal{O}(1/|T|)$ in equations (3.5). Topos and chronos are then expressed as

$$\varphi^\alpha_n(x) = \sum_k \hat{\varphi}^\alpha_n(k) e^{i2\pi kx/|X|}$$

$$\psi^\alpha_n(t) = \sum_w \hat{\psi}_n{}^\alpha(w) e^{i2\pi wt/|T|} .$$

The strategy then consists in seeking conditions under which equations (3.10) hold. Starting on the left hand side of (3.10a) we can write

$$\begin{aligned}
(U_0^* U_0 G_1^2 U_0^*)\ \psi^\alpha_n(t) &= A_n \left(U_0^* U_0 G_1^2\right)\ \varphi^\alpha_n(x) \\
&= A_n\ (U_0^* U_0) \left(\sum_j \delta(x - \Delta j)\right) \left(\sum_m \delta(x - \Delta m)\right)\ \varphi^\alpha_n(x) \\
&= A_n\ (U_0^* U_0) \sum_p \frac{1}{\Delta} e^{i2\pi pNXx/|X|} \sum_q \frac{1}{\Delta} e^{i2\pi qNXx/|X|} \\
&\quad \sum_k \hat{\varphi}^\alpha_n(k) e^{i2\pi kx/|X|} \\
&= \frac{A_n}{\Delta^2} \sum_{p,q,k} (U_0^* U_0)\ e^{i2\pi[(p+q)NX+k]x/|X|}\, \hat{\varphi}^\alpha_n(k) \\
&= \frac{A_n}{\Delta^2} \sum_{p,q,k} U_0^* \left(\int_X u(x,t) e^{i2\pi[(p+q)NX+k]x/|X|}\, dx\right)\ \hat{\varphi}^\alpha_n(k) .
\end{aligned}$$

Hence

$$(U_0^* U_0 G_1^2 U_0^*)\ \psi^\alpha_n(t) = \frac{A_n}{\Delta^2} \frac{|X|}{2} \sum_{p,q,k} U_0^*\, \hat{u}((p+q)NX + k, t)\, \hat{\varphi}^\alpha_n(k) , \qquad (3.13a)$$

where $\hat{u}((p+q)NX + k, t)$ denotes the spatial Fourier transform of u. Now, by working out the right hand side of (3.10a), one obtains

$$(U_0^* G_2^2 U_0 U_0^*)\ \psi^\alpha_n(t) = \frac{A_n}{\tau^2} \frac{|T|}{2} \sum_{r,s,w} \hat{u}(x, (r+s)NT + w)\, \hat{\psi}^\alpha_n(w) , \qquad (3.13b)$$

where $\hat{u}(x,(r+s)NT+w)$ denotes the temporal Fourier transform of u. By developing (3.10b) in a similar manner, one can write

$$(U_0U_0^*G_2^2U_0)\ \varphi_n^\alpha(x) = \frac{A_n}{\tau^2}\frac{|T|}{2}\sum_{r,s,w} U_0\,\hat{u}(x,(r+s)NT+w)\,\hat{\psi}_n^\alpha(w)\ , \qquad (3.13c)$$

$$(U_0G_1^2U_0^*U_0)\ \varphi_n^\alpha(x) = \frac{A_n}{\Delta^2}\frac{|X|}{2}\sum_{p,q,k} \hat{u}((p+q)NX+k,t)\,\hat{\varphi}_n^\alpha(k)\ . \qquad (3.13d)$$

Substituting equations (3.13) in conditions (3.10) leads to the non-resonant condition in terms of $\varphi_n^\alpha(x)$ and ψ_n^α, which can be equivalently written as the following system

$$\sum_{p,q,k}\hat{\varphi}_n^\alpha(k)\left[U_0U_0^*\,\hat{u}((p+q)NX+k,t) - A_n^2\,\hat{u}((p+q)NX+k,t)\right] = 0 \quad \forall x\in X\ , \qquad (3.14a)$$

$$\sum_{r,s,w}\hat{\psi}_n^\alpha(w)\left[U_0^*U_0\hat{u}(x,(r+s)NT+w) - A_n^2\,\hat{u}(x,(r+s)NT+w)\right] = 0 \quad \forall t\in T\ . \qquad (3.14b)$$

The above system (3.14) has a solution if and only if

$$U_0^*U_0\,\hat{u}(x,(r+s)NT+w) = A_n^2\,\hat{u}(x,(r+s)NT+w) \quad \forall\, r,s,w\in\mathbb{Z}\ ,$$

and

$$U_0U_0^*\hat{u}((p+q)NX+k,t) = A_n^2\hat{u}((p+q)NX+k,t) \quad \forall\, p,q,k\in\mathbb{Z}\ .$$

Hence, $\hat{u}(x,(r+s)NT+w)$ and $\hat{u}((p+q)NX+k,t)$ are solutions of the BOD equations (3.12), and therefore they must be linear combinations of topos and chronos of the subspace associated with the eigenvalue A_n, i.e.

$$\hat{u}(x,(r+s)NT+w) = \sum_{\alpha=1}^{\alpha_{max}} c_\alpha\varphi_n^\alpha(x)\ , \qquad (3.15a)$$

$$\hat{u}((p+q)NX+k,t) = \sum_{\alpha=1}^{\alpha_{max}} \tilde{c}_\alpha \psi_n^\alpha(t) \,. \tag{3.15b}$$

In addition, by using the definition of $\hat{u}$ and the BOD of u, we can write

$$\begin{aligned} \hat{u}(x,(r+s)NT+w) &= \frac{2}{|X|}\int_T u(x,t)\, e^{i2\pi[(r+s)NT+k]w/|T|}\, dt \\ &= \frac{2}{|X|}\sum_m A_m^\beta \sum_{\beta=1}^{\beta_{max}} \varphi_m^\beta(x) \int_T u(x,t)\, e^{i2\pi[(r+s)NT+k]w/|T|}\, dt \,, \end{aligned}$$

$$\hat{u}(x,(r+s)NT+w) = \sum_m A_m^\beta \sum_{\beta=1}^{\beta_{max}} \varphi_m^\beta(x)\, \hat{\psi}_m^\beta((r+s)NT+w) \,. \tag{3.16a}$$

A similar procedure results in the identity

$$\hat{u}((p+q)NX+k,t) = \sum_m A_m^\beta \sum_{\beta=1}^{\beta_{max}} \psi_m^\beta(t)\, \hat{\varphi}_m^\beta((p+q)NX+k) \,. \tag{3.16b}$$

Equations (3.15) and (3.16) match simultaneously if and only if

$$\begin{gathered} \hat{\varphi}_m^\beta((p+q)NX+k) = 0 \quad \forall\, k,p,q \in \mathbf{Z} \\ \forall\, m \neq n \qquad\qquad \textit{and} \qquad\qquad (3.17) \\ \hat{\psi}_m^\beta((r+s)NT+w) = 0 \quad \forall\, r,s,w \in \mathbf{Z}, \end{gathered}$$

namely the Fourier sidebands do not intersect for $m \neq n$. If k_m and w_m are integers associated with the Fourier components of φ_m^β and ψ_m^β, then the sidebands do not intersect if and only if

$$k_m \neq (p+q)NX+k \qquad \textit{and} \qquad w_m \neq (r+s)NT+w$$

or,

$$\frac{k_m}{|X|} \neq \frac{(p+q)}{\Delta} + \frac{k}{|X|} \qquad \textit{and} \qquad \frac{w_m}{|T|} \neq \frac{(r+s)}{\tau} + \frac{w}{|T|} \,.$$

Now setting $k_{max} = \max_n\{k_n\}$ and $w_{max} = \max_n\{w_n\}$, we conclude that conditions (3.17) hold if and only if

$$\frac{k_{max}}{|X|} \leq \frac{1}{2\Delta} \qquad \textit{and} \qquad \frac{w_{max}}{|T|} \leq \frac{1}{2\tau} \,.$$

There remains to prove that under (3.11), the LI condition is also valid. The procedure is very similar; by expanding in Fourier series, we calculate the norms

$$\begin{aligned}
\|d_1\varphi_n^\alpha\|^2 &= \int_X (d_1\varphi_n^\alpha)^*(x)\,(d_1\varphi_n^\alpha)(x)\,dx \\
&= \sum_{k,m,p,q} \frac{1}{\Delta^2}\,(\hat{\varphi}_n^\alpha(m))^*\;\hat{\varphi}_n^\alpha(k) \int_X e^{-i2\pi[qNX+m]x/|X|}\,e^{i2\pi[pNX+k]x/|X|}\,dx \\
&= \sum_{k,m,p,q} \frac{1}{\Delta^2|X|}\,(\hat{\varphi}_n^\alpha(m))^*\,\hat{\varphi}_n^\alpha(k)\;\delta_{qNX+m,\,pNX+k} \\
&= \sum_{k,p} \frac{1}{\Delta^2|X|}\,\|\hat{\varphi}_n^\alpha(k)\|^2
\end{aligned}$$

where (3.11) has been used. Finally by Parseval's equality, we obtain

$$\|d_1\varphi_n^\alpha\|^2 = \frac{1}{\Delta^2}\,\|\varphi_n^\alpha\|^2\,, \tag{3.18a}$$

and similarly

$$\|d_2\psi_n^\alpha\|^2 = \frac{1}{\tau^2}\,\|\psi_n^\alpha\|^2\,, \tag{3.18b}$$

Q.E.D.

Remark 3.6 The two inequalities (3.11), which are the equivalents of the Nyquist limit for the Fourier analysis, establishes the minimal value of the mesh size required for a correct interpretation of the biorthogonal decomposition of the function $u(x,t)$. Under (3.11) not only do we know that the discrete BOD is the discretization of the BOD, but also we have the exact deformation undergone by the (space-time) symmetries due the discretization process (see equation (2.16)).

Remark 3.7 The theorem establishes that, under conditions (3.11), the local isotropy is valid *globally* as shown in equations (3.18). This implies that the entropy will be unchanged as proven in Reference [2].

Remark 3.8 In general, given a signal, we know a priori neither its wavelength nor its frequency content. At first, we thus have to guess the discretization to use. Both the Nyquist limit for Fourier decompositions and its counterpart for biorthogonal decompositions establish a minimal mesh size required so that if the real values of the wave numbers and frequencies to measure are below that threshold, then they will be correctly observed. ***The converse is not true*** for either the Fourier expansion, or the biorthogonal decomposition. In other words, if the condition (3.11) is not satisfied and the observed frequency and wavenumber values fall below the limit, this does not mean that they are correct. We have seen such an example in Section 3.2 in which the sampling frequency was 15 and therefore the highest readable frequency is 7.5. However, we have observed that the observed value of 5 was incorrect. This problem originates in the above proof itself where we have seen that the position of the Fourier components will change unless the condition (3.11) is fulfilled. This point can be detected by varying the mesh size: if different meshes make the decomposition vary, the sampling has to be refined. Of course, from the experimental point of view, filtering the signal before the analysis is a much simpler solution.

Examples: I now give two illustrations of the previous theorem. First, as in Section 3.2, I perform the BOD of the function

$$\begin{aligned} u(x,t) &= \cos[2\pi(.2x)]\cos[2\pi(.5x-2t)] \\ &\quad +.6\cos[2\pi(.3x)]\,[1+\cos(2\pi t)]\cos[2\pi(.17x-13t)]\,, \end{aligned} \tag{3.19}$$

under two different temporal meshes. I recall that the above function is not a traveling wave, but a superposition of distinct (spatially and temporally) modulated waves propagating at various speeds. The meshes are $1/\Delta = 10$ and $1/\tau = 30$, in the first case and $1/\Delta = 10$ and $1/\tau = 15$, in the second case. Figures 3.4 and 3.5 display the decomposition for both samplings, the results are similar to those reported in Section

3.2. For $1/\tau = 30$, the right decomposition is obtained, while the resonances due to the temporal grid mesh frequency at 15 distort the original subspaces. Note that here there is no decrease in the signal dimension as observed in Section 3.2.

The second case illustrates the convergence of the biorthogonal entropy (2.7) towards its true value as the temporal mesh is refined. For this purpose, I add a 0.5% uniform noise to the above signal (3.19). Figure 3.6 shows the variation of the entropy with $1/\tau$: a good agreement with equation (3.6) and Reference [2] is found.

References for Chapter 3

[1] H. Joseph Weaver, "Theory of Discrete and Continuous Fourier Analysis," (John Whiley and Sons, New York, 1989).

[2] N. Aubry and R. Lima, "The dynamics of spatio-temporal modulations," Chaos **5**, pp. 578-588 (1995).

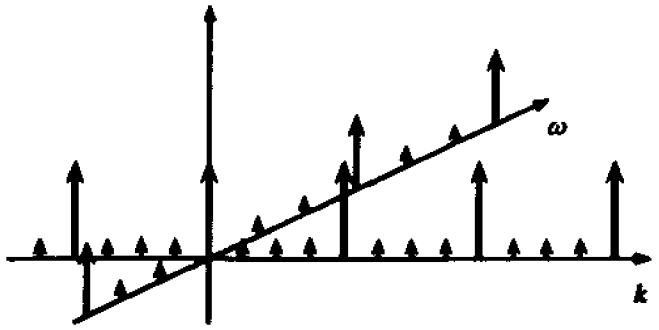

Figure 3.1: Diagram showing the Fourier coefficients of the functions d_1 and d_2 in equations (3.3) and (3.4) in (k, w) space. The large arrows represent coefficients at multiples of NX or NT, the small arrows correspond to the terms of order $\mathcal{O}(1/|X|)$ and $\mathcal{O}(1/|T|)$ which are neglected in Sections 3.1, 3.2 and 3.3.

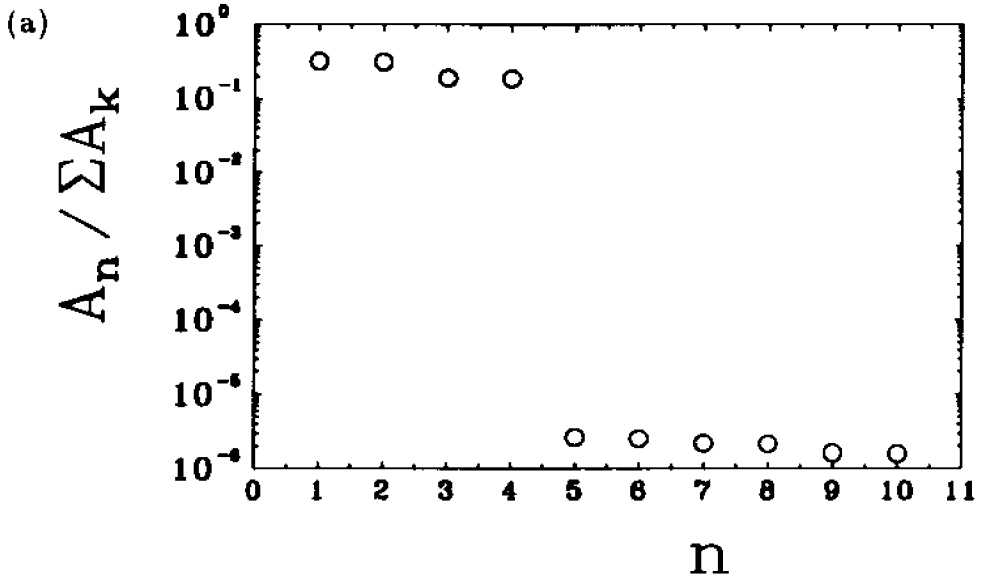

Figure 3.2: BOD of the traveling wave (3.9) in Section 3.2 for the sampling wavenumber $1/\Delta = 12.12$ and frequency $1/\tau = 30$; in agreement with condition (3.11) the description is correct. (a) The biorthogonal spectrum; next page (b) topos and chronos in their spatial and temporal representations; (c) topos and chronos in their Fourier representation.

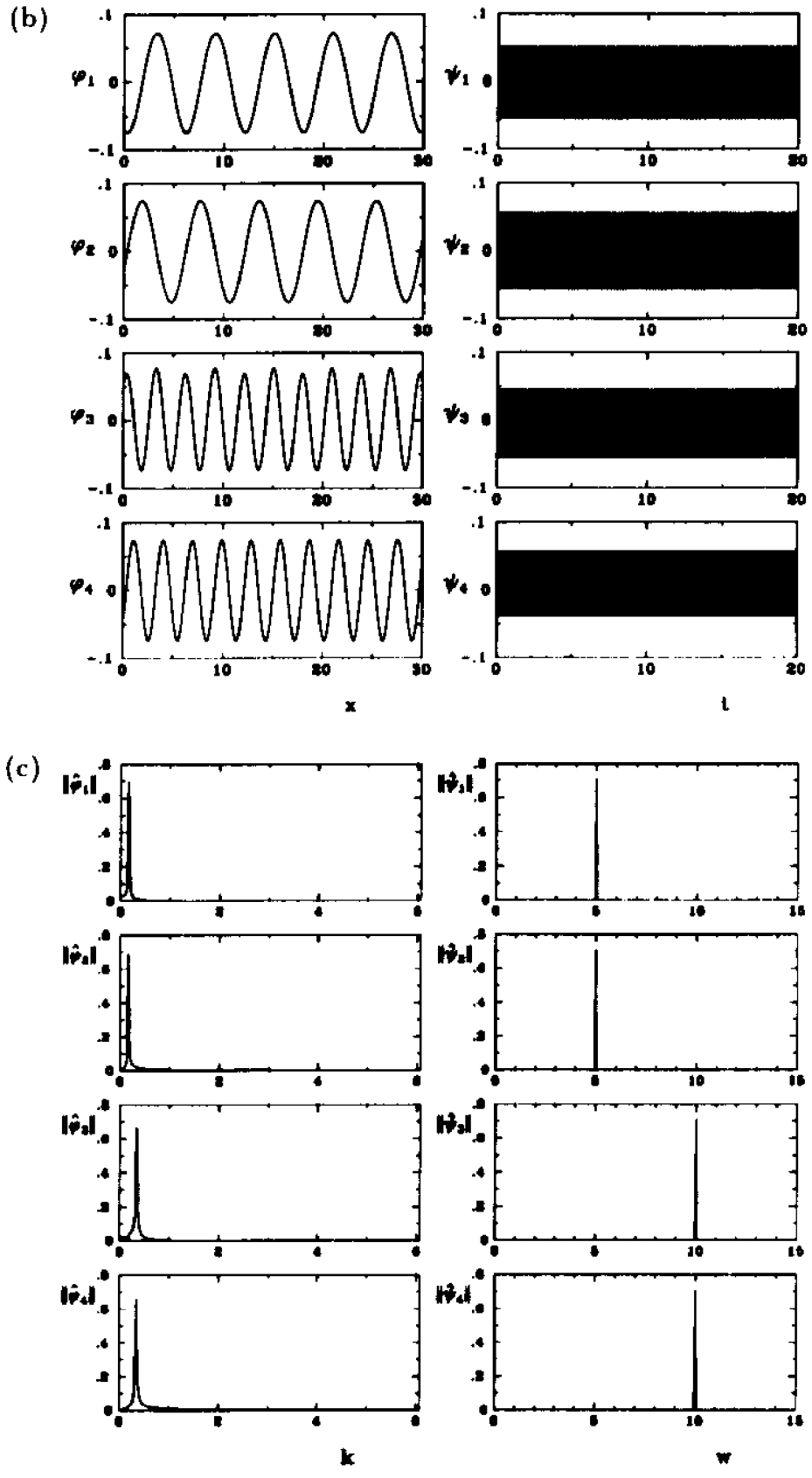

Figure 3.2 continued.

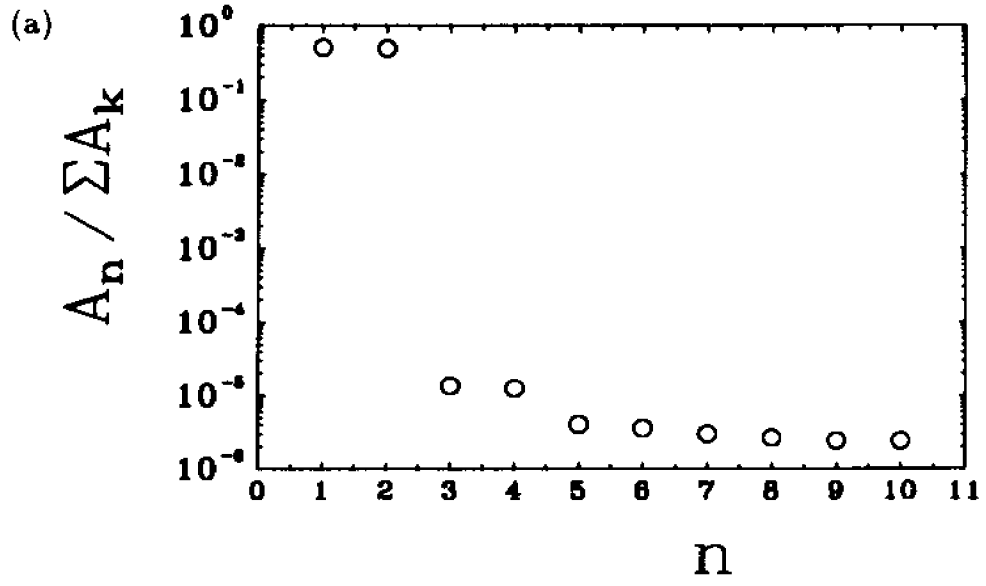

Figure 3.3: BOD of the traveling wave (3.9) in Section 3.2 for the sampling wavenumber $1/\Delta = 12.12$ and frequency $1/\tau = 15$ showing that the resonances introduced by the discretization process distort the eigenspaces. (a) The biorthogonal spectrum showing a decrease in the signal dimension; next page (b) deformed topos and chronos in their spatial and temporal representations; (c) topos and chronos in their Fourier representations displaying a mixture of the involved frequencies and wavenumbers.

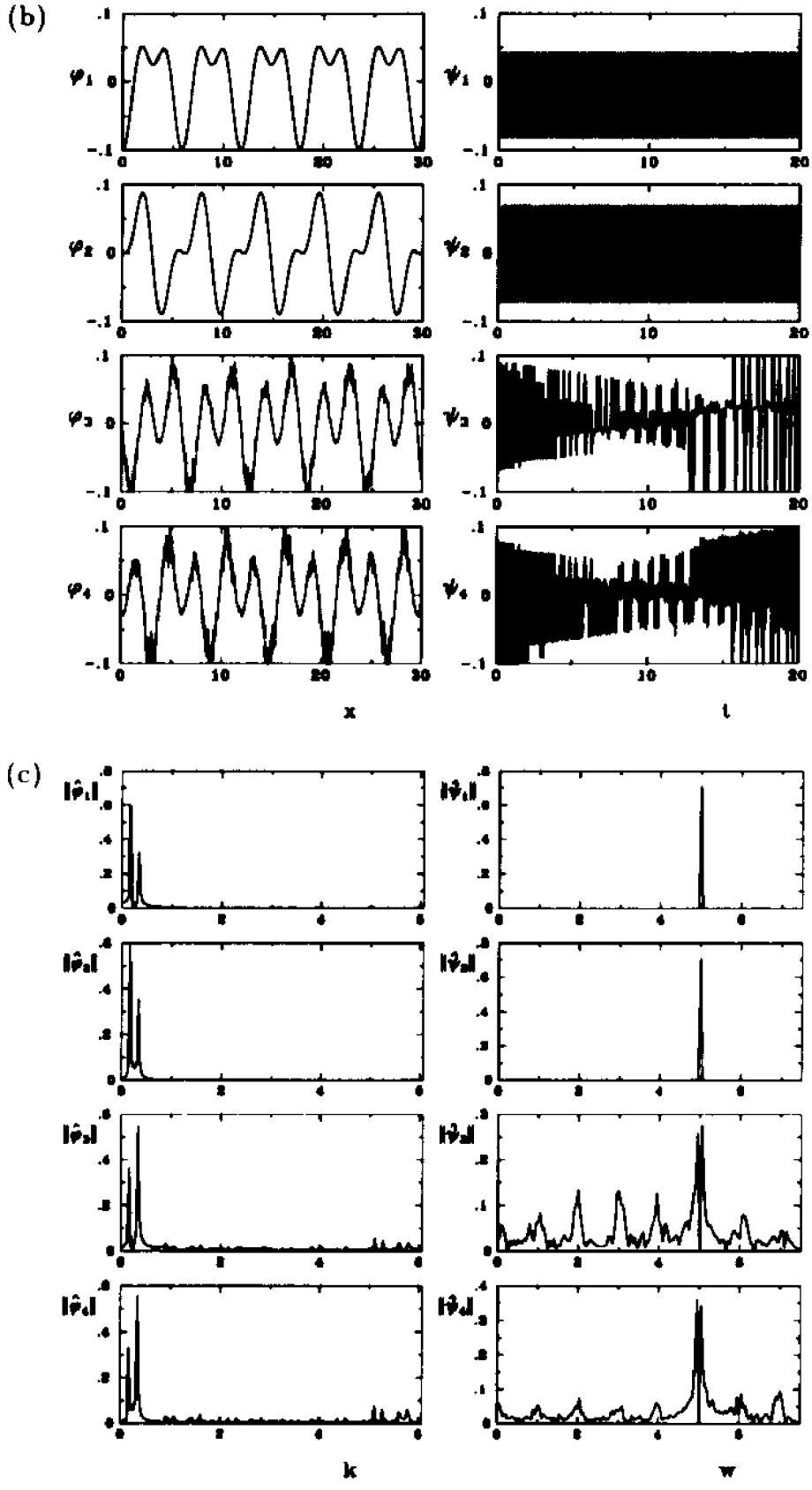

Figure 3.3 continued.

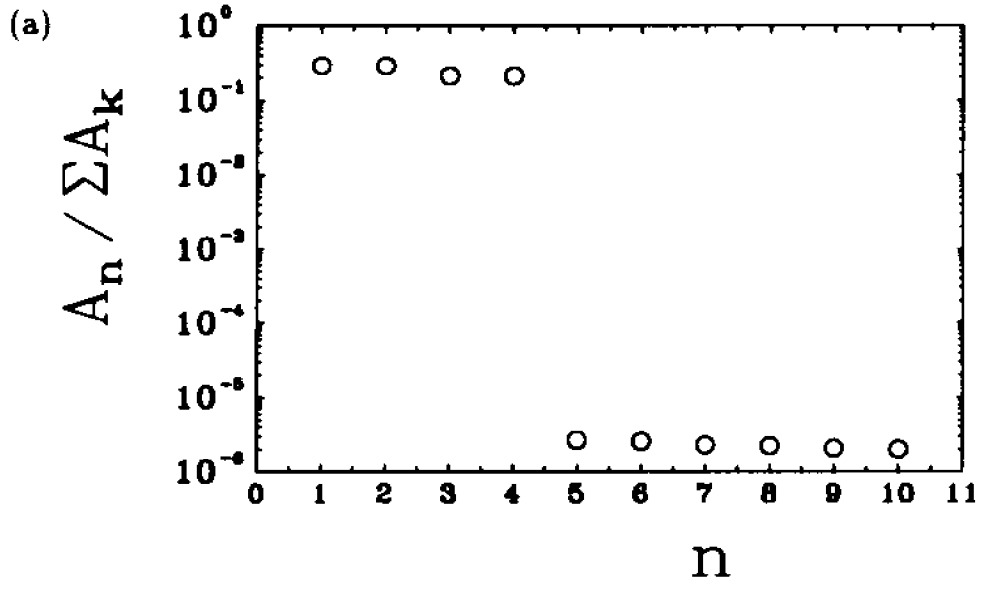

Figure 3.4: BOD of the signal (3.19) for the sampling wavenumber $1/\Delta = 10$ and frequency $1/\tau = 30$; in agreement with condition (3.11), the description is correct. The function (3.19) is the superposition of two modulated monochromatic plane waves. (a) The biorthogonal spectrum; next page (b) topos and chronos in their spatial and temporal representations; (c) topos and chronos in their Fourier representations.

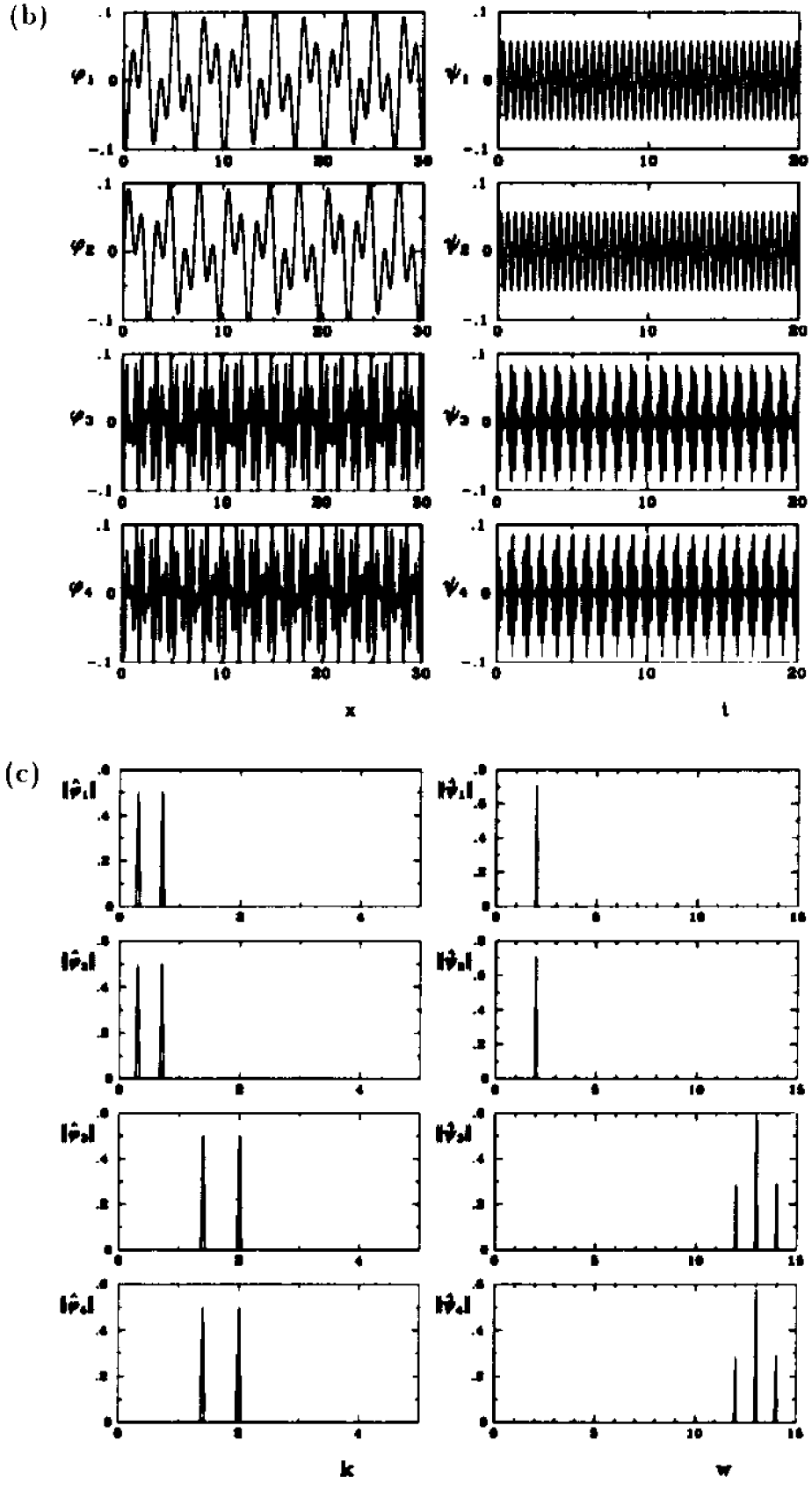

Figure 3.4 continued.

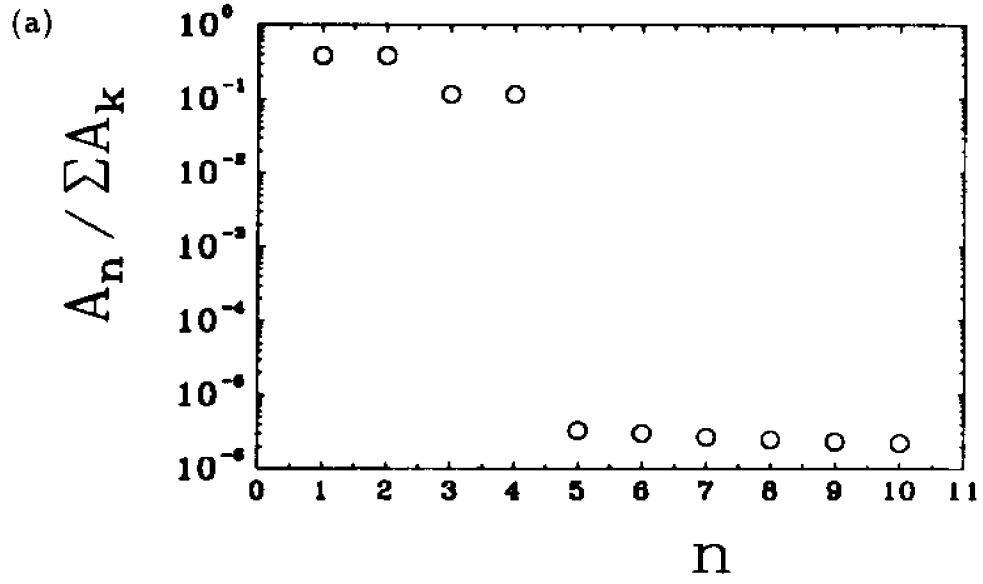

Figure 3.5: BOD of the function (3.19) for the sampling wavenumber $1/\Delta = 10$ and frequency $1/\tau = 15$, showing that the insufficient temporal sampling produces resonances. (a) The biorthogonal spectrum; next page (b) topos and chronos in their spatial and temporal representations; (c) topos and chronos in their Fourier representation. Note the appearance of all involved wave numbers and frequencies in all eigenvectors.

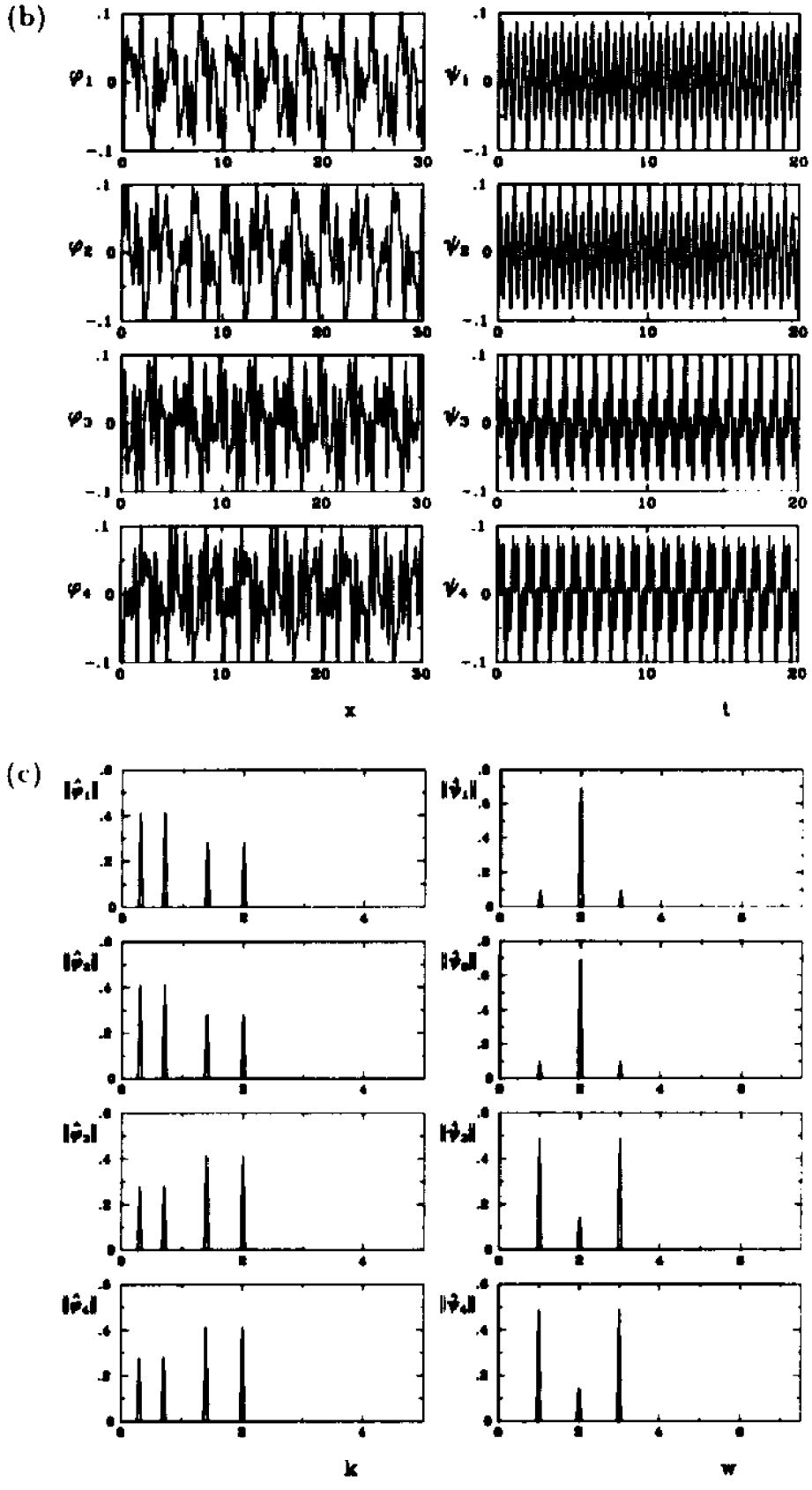

Figure 3.5 continued.

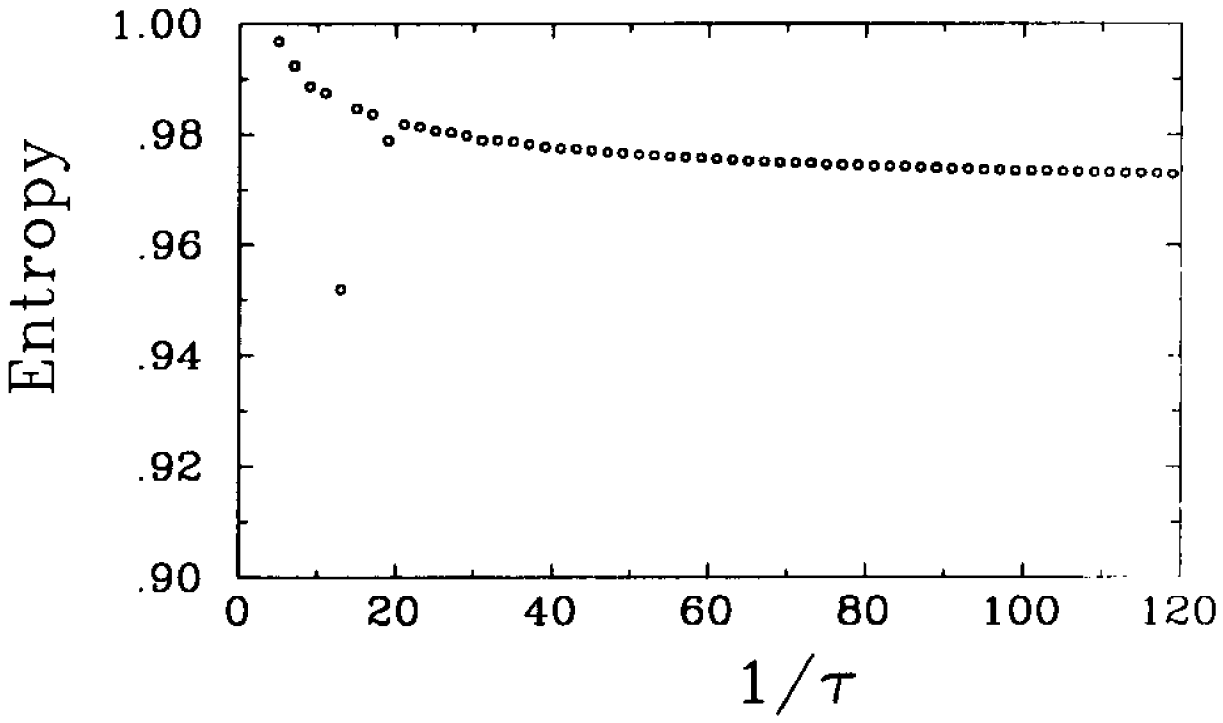

Figure 3.6: The biorthogonal entropy as a function of the temporal sampling frequency $1/\tau$ of the signal (3.19), showing convergence as $1/\tau$ increases.

Chapter 4

Falling Film Flows

As described in Chapter 1 when the Reynolds number (Re) is larger than a critical value, flowing films are unstable for sufficiently long wavelength disturbances. The observed interfacial waves show solitary waves, various secondary instabilities, and complex disordered patterns [1, 2, 3, 4, 6]. The great variety of nonlinear phenomena, and the fairly low flow rate at which they occur make the system ideal for studies of dynamical complexity in open flows. In addition, the flow may be specified by a single scalar field, the film thickness $h(x,t)$, which greatly simplifies the analysis.

In this chapter I present a quantitative analysis of spatio-temporal experimental data of the above system. I focus on two different phenomena both concerning two-dimensional waves. For the first one, the waves, initially travelling at constant speed, become unstable as Re is increased. Above the instability onset, the wave fronts split and coalesce and no single propagation speed can be identified; the original space-time translation symmetry no longer holds. The second phenomenon is the secondary instability the system undergoes due to the nonlinear interaction between the harmonic and subharmonic components present in the flow. In the subharmonic instability the fundamental mode and its harmonics (e.g. $k, 2k$, etc.) are resonant

with their subharmonic ($k/2, 3k/2$, etc.).

The experimental data were studied at a variety of Reynolds numbers and perturbation frequencies, via both Fourier and biorthogonal decompositions. I find that the free-surface evolution can be described by a spatio-temporal modulation of a uniformly traveling wave which develops gradually above a threshold. The contribution to the flow evolution originating in the subharmonic instability is captured by the biorthogonal analysis which also shows its convective nature.

4.1 Experimental Considerations

4.1.1 Experimental Method

The experiment performed by Jun Liu and J. P. Gollub at Haverford College is described as follows; a detailed description can be found in [5, 6, 7]. A schematic diagram of the experimental apparatus is shown in Fig. 4.1. The film plane is 200 cm long by 50 cm transverse to the flow; relatively small inclination angles from 4° to 10° are employed. The entrance flow rate is perturbed at frequency f and amplitude A by applying small pressure variations to the entrance manifold. Aqueous solutions of glycerin (about 52% by weight) are used in this experiment; the kinematic viscosity and surface tension are 5.55 ± 0.10 cs and 67 ± 2 dyn/cm, respectively, at 22.5°C. The control parameters varied in this experiment are the external forcing frequency f and the Reynolds number Re.

A fluorescence imaging method is used to measure the film thickness $h(x, y, t)$ in real time with a sensitivity of 8-10 μm. Initially two-dimensional (i.e., invariant in the y-direction), the waves can be described only as a function of one space dimension and time. In this regime, the data $h(x, t)$ were taken along the center strip of the film plane. There are 640 pixels in the flow direction with a spatial resolution 0.065

cm/pixel. The time step is 1/60 s and 1536 images were taken for each set of data. The Nyquist wavenumber and frequency are 7.75 1/cm and 30 Hz, respectively. (In Chapter 3, I have derived the equivalent of the Nyquist condition in the biorthogonal decomposition context).

4.1.2 Secondary Instability of Multipeaked Waves

As mentioned in Section 1.2 the nonlinear evolution of initially sinusoidal waves depends strongly on the frequency f. A boundary $f_s(Re)$ separates two types of nonlinear evolution. Solitary and multipeaked waves appear below $f_s(Re)$, while single-peaked, nearly sinusoidal waves occur above the boundary. Subtle differences between various multipeaked and solitary waveforms have been illustrated by Liu and Gollub [7].

For a fixed Re, when f is increased from that of a solitary wave train, the solitary wavefronts become closer to each other. As the frequency is increased further, separated pulses are not formed. Instead, subsidiary waves develop through the growth of small depressions on the primary peaks: each primary peak splits into two peaks. The phenomenon can also be observed by increasing Re with a fixed frequency near $f_s(Re)$. In Fig. 4.2, we present the data at $f = 5$ Hz and $\beta = 6.4°$. The spatiotemporal data of film thickness $h(x,t)$ are taken in a window of length 41.6 cm centered at $x = 82$ cm from the entrance. At $Re = 25.6$, we observe waves which travel at a constant velocity without deformation (Fig. 4.2a). When Re is larger than 30, the small depressions described above can be observed (Fig. 4.2b for $Re = 35.2$). It appears that the wave crests split and coalesce as they travel downstream. As Re increases further, the position where the splitting-coalescence process begins moves upstream. At $Re = 67.7$ (Fig. 4.2c), the wave structure inside the sampling window becomes substantially more complex: the large waves have steep fronts and stretched tails,

and their shape is close to that of solitary waves. In addition, the nonlinear interactions lead to strongly disorganized waves downstream. In all cases, the space-time translation symmetry characteristic of stationary waves at $Re = 25.6$ is lost as Re is increased.

Jun and Gollub have reported that periodic waves are unstables to subharmonic instability over a wide interval of perturbation frequencies [8]. I illustrate the instability in the space-time representation of Fig. 4.3, that correspond to a perturbation frequency $f = 7$Hz, $Re = 37.4$, and $\beta = 6.4^o$. As the waves travel down the plane the wavelength of the waves is roughly halved: an apparent spatial period doubling occurs.

4.2 The Splitting and Coalescence of the Front Waves

In this section I focus the attention on the understanding of the instability from a spatio-temporal viewpoint. I use several different techniques for this purpose: the Fourier decomposition, a biorthogonal decomposition, and entropy considerations [9]. Although the study was performed for many Reynolds numbers and perturbation frequencies, the discussions emphasize the data obtained at $Re = 25.6$, $Re = 35.2$ and $Re = 67.7$, at $f = 5$Hz (Fig. 4.2).

4.2.1 Fourier analysis

I first study the flows displayed in Fig. 4.2 by Fourier decomposition, a common tool for the study of wave propagation phenomena. Specifically, I compute the norm of the one-dimensional spatial Fourier transform of $h(x,t)$, $\|\hat{h}(k,t_o)\|$ and average

in time, assuming stationarity. Similarly, I calculate the one-dimensional temporal Fourier spectra of $\hat{h}(x_i, \omega)$ at two different spatial locations: $x_1 = 10.3$ and $x_2 = 41.1$ cm. These temporal and spatial points are chosen to belong to the $X \times T$ window of the biorthogonal analysis described in the next section. The resulting spectra, corresponding to $Re = 25.6$, $Re = 35.2$ and $Re = 67.7$, are shown in Fig. 4.4. The spatial spectra present high peaks at a fundamental value k_{Re} and its harmonics up to the third one. As Re increases, new Fourier components appear, and the spectrum eventually becomes quite broad.

The temporal Fourier spectra present peaks at the forcing frequency (5 Hz) and its harmonics, independently of the Reynolds number considered. As Re is increased, the relative energy of the peaks changes between the forcing frequency and its first harmonic, the latter becoming dominant downstream at $Re = 35.2$. This observation, particularly clear in the last panel of Fig. 4.4b, indicates the increased splitting of the wave fronts at the end of the spatial window. At $Re = 67.7$, the forcing frequency is dominant once again and the broad spectral background is much larger: the flow is now weakly turbulent.

In view of Fig. 4.2a and Fig. 4.4a the assumption of a unique propagation speed, i.e. $h(x,t) = g(x - ct)$, seems reasonable for the lowest Re. But the appearance of new peaks in $\|\hat{h}(k)\|$ at the higher Re's may correspond to various possible scenarios from a spatio-temporal viewpoint. The Fourier analysis carried above cannot discern among the different possibilities. I show below how the biorthogonal decomposition tool allows to identify the particular form for $h(x,t)$ after the secondary instability has occurred.

4.2.2 Biorthogonal Decomposition Analysis

In this section I characterize the wavefront splitting and coalescence process using the biorthogonal decomposition. Figure 4.5 presents the first fifteen normalized eigenvalues for the Re investigated Section 4.2.1. Since the first five modes capture more than 99.7% of the energy of the flows, I concentrate on these modes hereafter. The eigenvalues A_2, A_3, and A_4, A_5 are degenerate (with good numerical accuracy) (note that this feature seems to remain valid up to the fifteenth eigenvalue). The first five topos and chronos are shown in Fig. 4.6. The first topo and chrono φ_1 and ψ_1 are constants, and the term $A_1\varphi_1(x)\psi_1(t)$ of (2.4) represents the spatio-temporal average of the film thickness (the mean of all other topos and chronos, therefore, being zero [10]). At $Re = 25.6$ (Fig. 4.6a), topos and chronos are sinusoidal and regrouped by pairs (φ_2, φ_3), (φ_4, φ_5), (ψ_2, ψ_3), and (ψ_4, ψ_5), each pair corresponding to a degenerate eigenvalue. As shown in Section 2.2.1 of Chapter 2, this is a characteristic property of traveling waves, as well as the fact that topos and chronos of a given pair are translations of each other [10, 11]. As Re is increased to 35.2, the pairs (φ_2, φ_3) and (φ_4, φ_5) become modulated in amplitude (see Fig. 4.6b). Meanwhile, their corresponding chronos remain sinusoidal. At $Re = 67.7$, both the topos and the chronos are modulated in amplitude. The flow, at $Re = 25.6$, can thus be written as

$$h(x,t) = \sum_{n=1}^{N} A_n\varphi_n(x)\psi_n(t) = \sum_{n=1}^{N} g_n(x - ct) = g(x - ct),$$

where the topos φ_n and chronos ψ_n are Fourier modes. The functions $g_n(x - ct)$ are the various uniformly traveling sinusoidal waves characterizing each biorthogonal eigenspace. For $Re = 35.2$ and $Re = 67.7$, the flow becomes

$$h(x,t) = \sum_{n=1}^{N} A_n' g_n^1(x) g_n^2(t)\varphi_n'(x)\psi_n'(t) = \sum_{n=1}^{N} g_n^1(x) g_n^2(t) g_n'(x - ct), \qquad (4.1)$$

where the φ_n' and ψ_n' remain Fourier modes and $g_n'(x - ct)$ is a sinusoidal stationary wave. At $Re = 35.2$, the temporal functions $g_n^2(t)$ are close to one. In (4.1), the

fact that the functions $g_n^1(x)\varphi_n'(x)$ and $g_n^2(t)\psi_n'(t)$ remain topos and chronos (as in equations (2.21a) and (2.21b)) is due to the fact that the Fourier sidebands generated by the modulations do not intersect and, therefore, do not interact: the *non-resonant* condition (2.19), (2.20) in Chapter 2 is satisfied. Here, the spatial modulations g_n^1 have long wavelengths of (or larger than) the size of the spatial window. The persistence of the order-two degeneracy of the spectrum at higher Reynolds number in (4.1) indicates that there still exists a spatio-temporal symmetry satisfied by the flow; this is also consistent with the presence of a modulated uniformly traveling wave satisfying the non-resonant condition. The spatio-temporal symmetry of the modulated traveling wave with non-resonant sidebands is not a simple pair of translations in space and time, it involves the modulations as well (see equation (2.16)). The space-time symmetry satisfied by the uniformly traveling wave observed at $Re = 25.6$ is then deformed at $Re = 35.2$ and $Re = 67.7$. At $Re = 35.2$ the modulation can be seen among the topos only; it seems to be uniquely spatial at this Reynolds number (equation (2.21a) has a modulation different from a constant function). At $Re = 67.7$ the modulation is both spatial and temporal (both equations (2.21a) and (2.21b) have a modulation different from a constant function).

These features of the waves at different Reynolds numbers can also be observed in phase space. At $Re = 25.6$ the projection of the normalized trajectory η_x (2.5) onto the subspace spanned by the vectors ψ_2 and ψ_3, i.e.

$$P_{2,3}\eta_x = \varphi_2(x)\psi_2 + \varphi_3(x)\psi_3,$$

and similarly the projection onto the subspace spanned by ψ_4 and ψ_5, i.e.

$$P_{4,5}\eta_x = \varphi_4(x)\psi_4 + \varphi_5(x)\psi_5,$$

are both quasi-circles (Fig. 4.7a). This behavior is a clear indication of the spatial translation symmetry. However, a small amplitude modulation, responsible for the

broadening of the trajectory around the circle, can already be observed. The projections of the orbit η_x onto the subspaces spanned by ψ_2, ψ_3 and ψ_4, ψ_5 at both $Re = 35.2$ and $Re = 67.7$ (Figures 4.7b, c) display, from a geometrical point of view, the changes which have occurred in the dynamics: quasi-circles, due to the spatial modulation, have significantly thickened (equation (2.13)). Likewise, in order to observe the effect of the temporal modulation in phase space, I consider the projection of the normalized trajectory ξ_t (2.6) onto the subspace spanned by the vectors φ_2 and φ_3, i.e.

$$\tilde{P}_{2,3}\xi_t = \varphi_2(x)\psi_2 + \varphi_3(x)\psi_3,$$

and similarly the projection onto the subspace spanned by φ_4 and φ_5. Fig. 4.7d, e display quasi-circles at both $Re = 25.6$ and $Re = 35.2$ while Fig. 4.7f shows that a considerable thickening of the circles occurs at $Re = 67.7$. The latter is due to the effect of the temporal modulation, which appears at a higher value of Re than does the spatial modulation.

The reconstruction of the flow with the first five terms of (2.4) only is shown in Fig. 4.8. While uniformly traveling wave fronts are observed in Fig. 4.8a at $Re = 25.6$, the splitting and coalescence of the waves at $Re = 35.2$ are clearly reproduced in Fig. 4.8b. These phenomena are thus due to the development of spatial modulations in the flow. The reconstruction with only the second and third modes in Fig. 4.8c shows neither splits nor coalescences of the wave fronts, *the profile being modulated spatially* as a whole. (The same picture with a different wavenumber and frequency is obviously obtained by restricting the reconstruction to another (degenerate) biorthogonal eigenspace.) This observation shows the complex effect of the modulation on a traveling wave in physical space. Both the modulation and the presence of harmonics in the carrier wave are therefore crucial in reproducing basic features of the dynamics such as splitting and coalescence of wave fronts. Moreover, the spatial modulation functions

g_n^1 seem to be different for the various harmonic terms in (4.1). The more complicated spatial and temporal modulations at $Re = 67.7$ are also easily represented using the first five terms (Fig. 4.8d).

The use of biorthogonal decompositions allows to identify the instability in contrast with the Fourier analysis. In the later the modes are already prescribed and therefore the information is carried in the energy of the modes only, they cannot *adapt* themselves to the particular symmetries of the system in study, as it is the case for the biorthogonal modes.

4.2.3 Entropy Considerations

Since the previous pointwise description through topos and chronos is of a "microscopic" nature, it is interesting to know whether or not there is any indication of the dynamical change described earlier in the global entropy defined in (2.7). For that purpose, I calculate the entropy as a function of Reynolds number $H(Re)$ for the interval $25.6 \leq Re \leq 67.7$. Because the first mode (representing the spatio-temporal average of the film thickness) contains a large percentage of the total energy, its inclusion in the entropy will hide the contribution of the dynamically important, but less energetic, modes. For this reason, exclude the first mode in (2.7) and calculate

$$H = -\frac{1}{\ln(N-1)} \sum_{n=2}^{N} p_n \ln p_n,$$

with $p_n = A_n^2 / \sum_{j=2}^{N} A_j^2$. Figure 4.9a shows that the global entropy increases with Re until it reaches its maximal value (within the range of Reynolds numbers studied in this paper) at about $Re = 54$. Note that the growth of two different types of modulation, spatial and temporal, are evident as two distinct rises in Fig. 4.9a. In order to understand the connection (if any) between the entropy and the "microscopic" behavior of the dynamics in phase space, we have computed the average distance to

the origin of the projection $P_{2,3}\eta_x$ of the vectors η_x onto the plane (ψ_2, ψ_3) in the temporal phase space $\mathcal{X}(T)$, and the standard deviation σ around this average (see Fig. 4.9b). This gives us a quantitative measure of the deformation exhibited by the orbit in the $\mathcal{X}(T)$-phase space as Re increases. The same procedure was applied to the vectors $P_{4,5}\eta_x$. It is interesting to note that the entropy and the standard deviation corresponding to the projection onto the (ψ_2,ψ_3)-plane both increase with Re up to $Re = 44$. The entropy increase is associated with a more uniform distribution of energy among the eigenvalues as the spatial modulation develops and deforms the dynamics in $\mathcal{X}(T)$ only. This effect does not persist when the orbit gets also deformed in $\mathcal{X}(X)$, under the action of temporal modulations. This occurs at higher Reynolds numbers ($Re > 44$).

4.3 The Subharmonic Instability

Jun and Gollub [8] have carried out an extensive analysis of the subharmonic instability, but their quantitative measurements are restricted to local wave slope data. The objective of this section is to study the instability from a spatiotemporal point of view.

The methodology is similar to that followed in Section 4.2. The data set containing records at many Re values are analyzed by Fourier and biorthogonal decompositions, but the discussion is restricted to the signals of Fig. 4.10. They correspond to an inclination angle $\beta = 6.4°$, a perturbation frequency $f = 7$Hz, and three Re values, $Re = 30.3$, $Re = 39.6$ and $Re = 67.7$. In the first two cases (see Fig. 4.10a and b), the interfacial waves are seen to travel at constant velocity and the wavelength is roughly halved as they travel downstream (the effect can only be seen at the end of the spatial window for $Re = 30.3$). As Re is further increased, the flow evolves to space-time

complexity as seen Fig. 4.10c. At this stage the splitting and coalescence of the front waves is observed again. Several questions then arise: can the instability be captured by a finite number of modes? Is the instability of the convective or absolute type? How is the process of splitting and coalescence of waves related to this instability?

4.3.1 Fourier Analysis

As in Section 4.2.1, I compute $\|\hat{h}(k, t_o)\|$ and $\|\hat{h}(x_i, \omega)\|$ corresponding to the wave profiles in Fig. 4.10 for the same location of the spatial window. The spatial Fourier spectra, displayed in Fig. 4.11, show peaks at the first and second harmonics, as well as moderate humps around the subharmonics. As Re increases the subharmonics fade in the background noise and the Fourier spectra become quite broad.

The temporal Fourier spectra deserve similar considerations. They present peaks at the forcing frequency (7 Hz) and its harmonics, independently of the Reynolds number and the location of the spatial windows at $x_1 = 10.3$ and $x_2 = 41.1$ cm as in Section 4.2. Weak subharmonic humps are seen at $Re = 30.3$ and $x_2 = 41.1$, and for both spatial positions when $Re = 39.6$. At higher Re the background noise renders any further comments difficult. The increased importance of the noise as Re increases is consistent with Liu *et al.*'s [5, 8] observation that the subharmonic instability is convective and therefore sensitive to noise.

4.3.2 Biorthogonal Decomposition Analysis

I now carry out the corresponding BOD analysis. Figure 4.12 presents the first fifteen normalized eigenvalues for the previous Reynolds numbers. As in Section 4.2.2, in the three cases, the eigenvalues A_2, A_3, and A_4, A_5 are degenerate (as well as A_6, A_7 for $Re = 39.6$). For reasons that will be clear below, I extend the study of the eigenvectors up to the thirteenth one. Fig. 4.13 displays topos and chronos in both

their spatial and temporal representations and their Fourier transforms. The first topo and chrono are constant at all Re's as in Section 4.2.2; they have thus identical interpretations and are not plotted. The picture is similar as that obtained in Section 4.2.2, Figures 4.13a, c, e, for the part of the flow consisting of the modes 2 to 5 display topos and chronos that are modulated sinusoids and regrouped by pairs: (φ_2, φ_3), (φ_4, φ_5), (ψ_2, ψ_3), and (ψ_4, ψ_5), each pair corresponding to a degenerate eigenvalue. The interpretation will be clear when I reconstruct the flow with these modes only. The Fourier representation in Figures 4.13b, d, f, supports the sinusoidal nature of these topos and chronos, and the presence of the (long wavelength) modulations cannot be detected from these Fourier transforms. Chronos (ψ_2, ψ_3) present peaks at 7Hz, and chronos (ψ_4, ψ_5) at the first harmonic, 14Hz.

Although it is difficult to characterize topos and chronos six to thirteen from their space and time representation, their corresponding Fourier representation $\hat{\varphi}_6, \ldots, \hat{\varphi}_{13}$ and $\hat{\psi}_6, \ldots, \hat{\psi}_{13}$ clearly enlights their nature (see Figures 4.13b, d, f). Broad subharmonic peaks are observed in both the wave number space and the frequency space. In addition, the amplification of the background noise at $Re = 67.7$ is evident. The biorthogonal analysis has thus clearly detected and identified the subharmonic instability.

The previous discussion differenciates two sets of modes: the first set (from modes 1 to 5) is of the kind seen in Section 4.2.2, the second one (from modes 6 to 13) is characterized by the subharmonic modes. Fig. 4.14 shows the (partial) reconstruction of the flow for each one of the two previous sets at the three Re's . Figures 4.14a, c, e encounters the first five terms of (2.4) only. The physical interpretation is clear: at $Re = 30.3$, the flow consists of a traveling wave moving at constant speed; the growth of φ_2, φ_3, φ_4, and φ_5 with x represents the global growth in amplitude of the waves as they travel downstream (see Figures 4.10a and 4.14a). At $Re = 39.6$, although the

topos and chronos become weakly modulated, this modulation can hardly be captured in physical space (see Fig. 4.14c). Instead, at $Re = 67.7$, the topos and chronos are strongly modulated (see Section 4.2.2) and the splitting and coalescence of the waves are clearly observed in Fig. 4.14e.

Figures 4.14b, d, f, represent the sum (2.4) of modes 6 to 13. The reconstructions capture both the spatio-temporal period doubling and the convective nature of the flow, two characteristic features of the secondary subharmonic instability in film flows. The waves grow in amplitude as they travel downstream, and the effect becomes increasingly important as Re increases. Figures 4.14b, d, f, support the Fourier spectra in Fig. 4.11: at $Re = 30.3$, the amplitude of the flow restricted to subharmonic modes only is close to zero in the upstream part of the window; this phenomenon is consistent with the absence of subharmonic peak in the Fourier spectrum at the (selected) upstream location. This is not the case for either $Re = 39.6$ or $Re = 67.7$ for which broad subharmonic peaks are detected both upstream and downstream. The increased noise level at $Re = 67.7$ renders the part of the flow exhibiting the subharmonic instability fairly complex in both space and time, as shown in Fig. 4.14f.

Two features deserve particular attention. First, despite the space-time complexity exhibited by the waves as Re increases, the latter travel at a roughly constant speed. Second, the spatio-temporal intermittent behavior is a solid feature of the subharmonic instability, clearly exhibited in the three previous examples.

Finally, it is important to note that the BOD analysis has shown that the instability is present at all Reynolds numbers. What changes as Reynolds number increases is the relative energy of the (subharmonic) modes compared with that of the primary waves (see Fig. 4.12).

4.4 Conclusions

In this chapter, I have shown that uniformly traveling waves on falling films become spatially modulated as Reynolds number increases. At higher Reynolds numbers, the modulation becomes spatial and temporal. This modulation, which is responsible for the deformation of the trajectory in phase space, produces the splitting and coalescence of the initially periodic wave fronts. The process is gradual and it is difficult to establish a precise threshold. The modulation was more easily distinguished from other types of deformation via the biorthogonal decomposition than by using Fourier analysis. Another significant point is that the presence of the modulation does not increase the number of degrees of freedom (i.e. modes) in the biorthogonal approach although the number of Fourier modes does increase.

The change in character of the modulations from spatial to spatiotemporal is clearly revealed by this analysis. I have also shown that the Fourier sidebands produced by the modulations are non-resonant and that the modulated wave thus enjoys a space-time symmetry. This symmetry is different from the simple space-time translation invariance of the stationary wave observed at low Reynolds number.

The analysis of the onset of the spatiotemporal chaos via the subharmonic instability confirms the convective origin of the instability and its period doubling effect in space and time, as previously described in References [5, 8]. In addition, it shows a space-time intermittent behavior.

References for Chapter 4

[1] P. L. Kapitza, S. P. Kapitza, Wave flow of thin viscous fluid layers, Zh. Eksp. Teor. Fiz. **19** 105 (1949); also in Collected Papers of P L. Kapitza, edited by D. Ter Haar (Pergamon, Oxford, 1965).

[2] A. E. Dukler, in *Progress in Heat and Mass Transfer*, ed. G. Hetsroni, S. Sideman and J. P. Hartnet (Pergamon, New York, 1972) Vol. 6, p. 207.

[3] S. V. Alekseenko, V. Y. Nakoryakov, and B. G. Pokusaev, Wave formation on a vertical falling liquid film, AIChE J. **31**, 1446 (1985).

[4] H.-C. Chang, Wave evolution on a falling film, Annu. Rev. Fluid Mech. **26**, 103 (1994).

[5] J. Liu, J. D. Paul, and J. P. Gollub, Measurements of the primary instabilities of film flows, J. Fluid Mech. **250**, 69 (1993).

[6] J. Liu, Nonlinear dynamics of wavy film flows, Ph.D. Thesis, University of Pennsylvania (1994), available through University Microfilms, Inc.

[7] J. Liu and J. P. Gollub, Solitary wave dynamics of film flows, Phys. Fluids **6**. 1702 (1994).

[8] J. Liu and J. P. Gollub, Onset of spatially chaotic waves on flowing films, Phys. Rev. Lett. **70**, 2289 (1993).

[9] F. Carbone, N. Aubry, Jun Liu, J. P. Gollub, and R. Lima, "Space-time description of the splitting and coalescence of wave fronts in film flows", PhysicaD (in press).

[10] N. Aubry, R. Guyonnet, and R. Lima, Spatio-temporal symmetries and bifurcations via biorthogonal decompositions. J. Nonlinear Sci. **2**, 183 (1992).

[11] N. Aubry, R. Guyonnet, and R. Lima, Turbulence Spectra, J. Stat. Phys. **67**, 183 (1992).

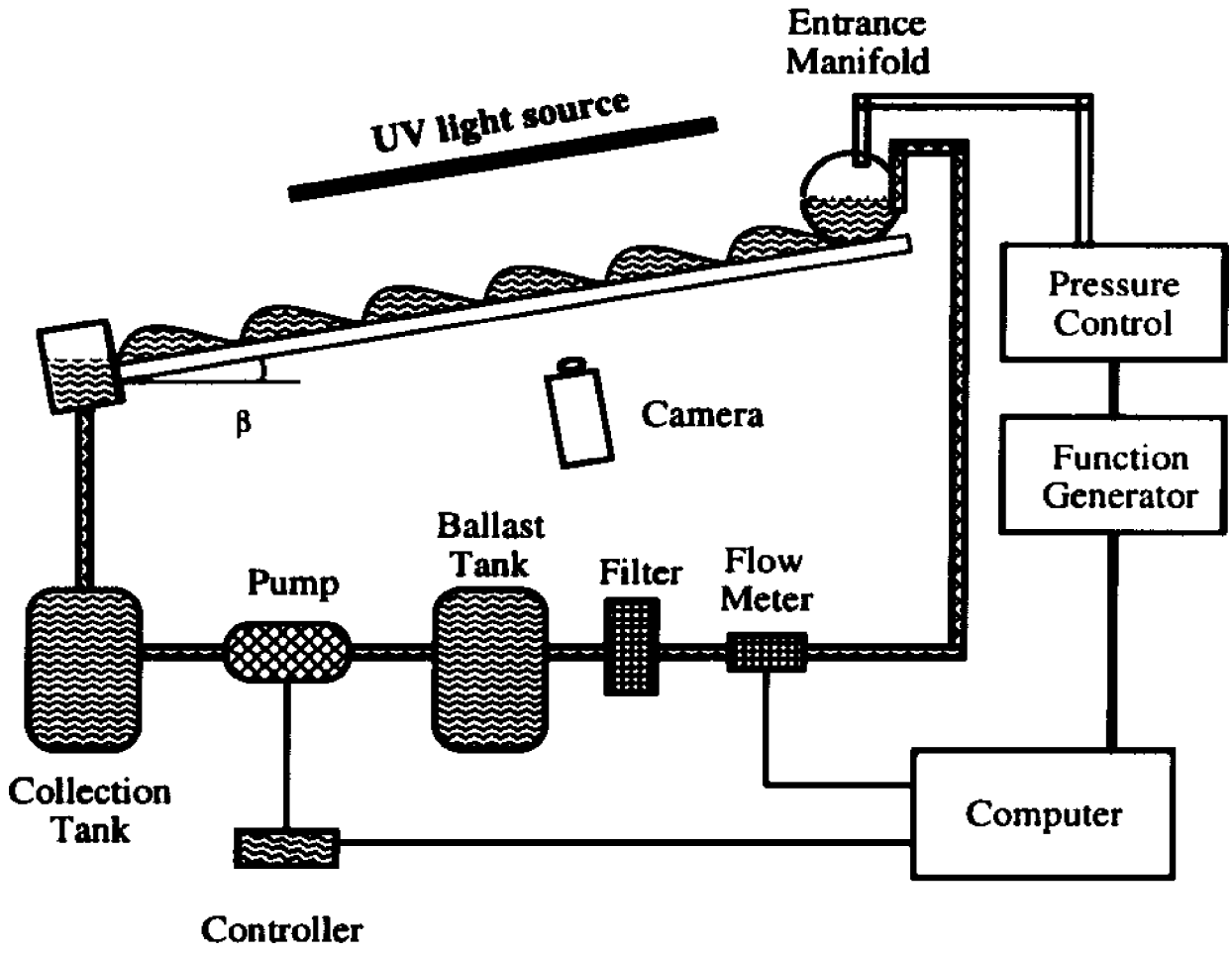

Figure 4.1: Schematic diagram of the film flow apparatus used by Jun and Gollub.

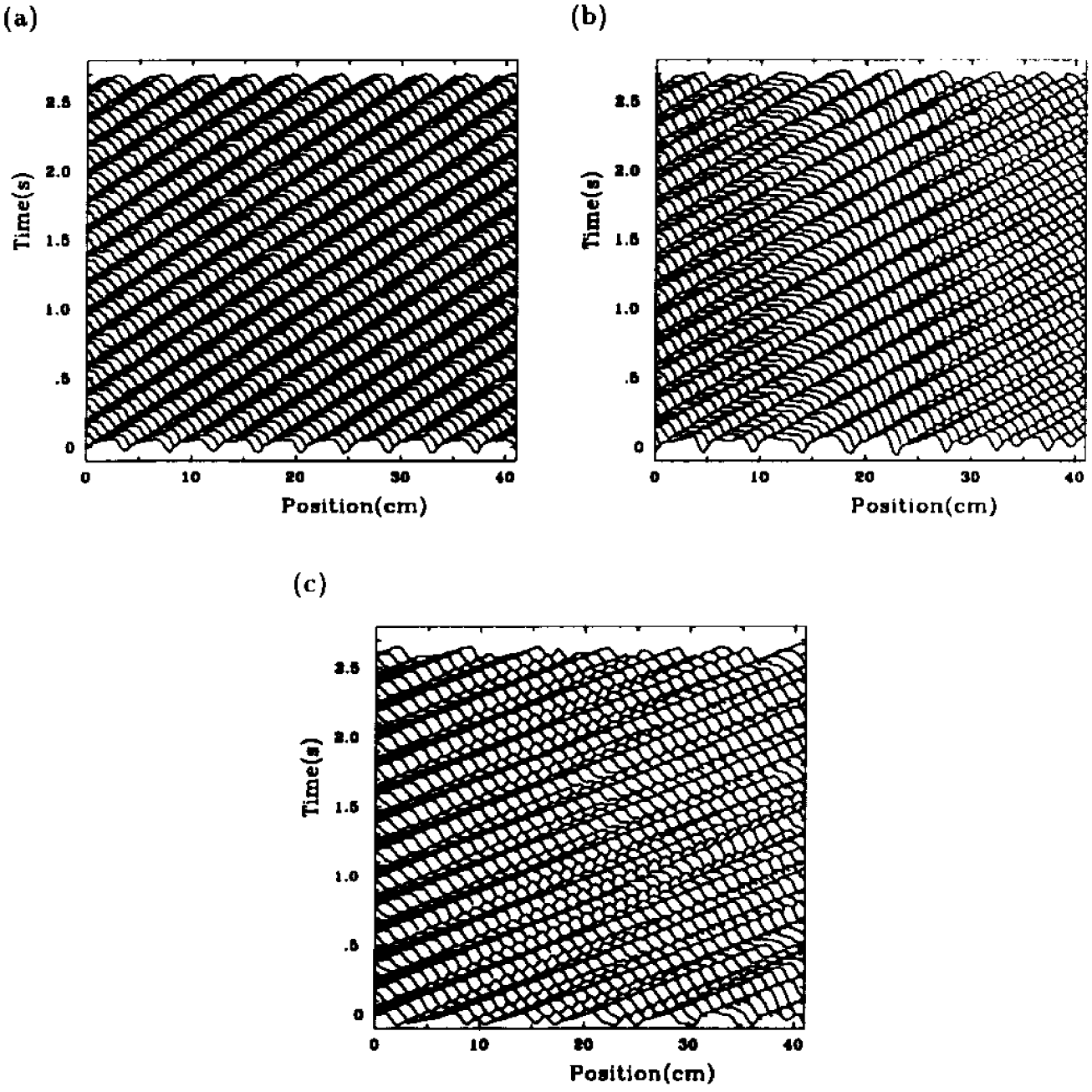

Figure 4.2: Spatio-temporal representation of the film thickness in a portion of the time domain used in this work, for $f = 5$Hz, $\beta = 6.4°$ and three Reynolds numbers. (a) $Re = 25.6$: the wave fronts travel at constant velocity; (b) $Re = 35.2$: the wave fronts split and coalesce as they travel. (c) $Re = 67.7$: the splitting and coalescence of wave fronts are more dramatic.

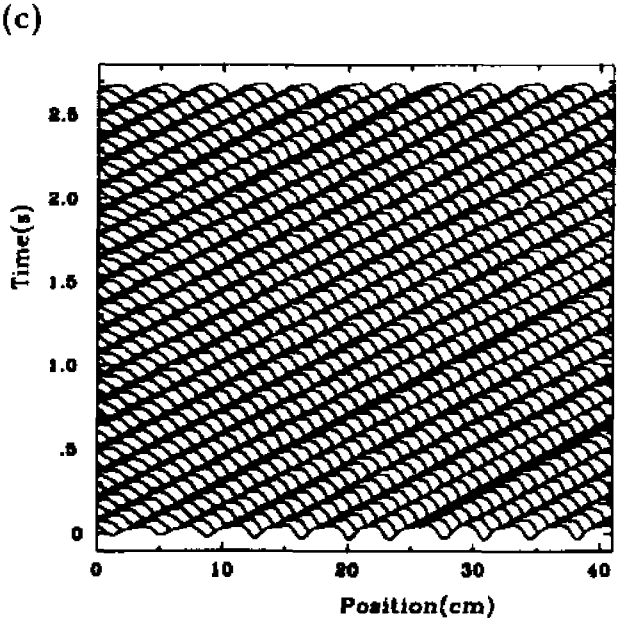

Figure 4.3: Spatio-temporal representation of the film thickness, for $f = 7$Hz, $\beta = 6.4°$ and $Re = 37.4$; the wavelength profiles roughly halve as they travel downstream in an apparent period doubling.

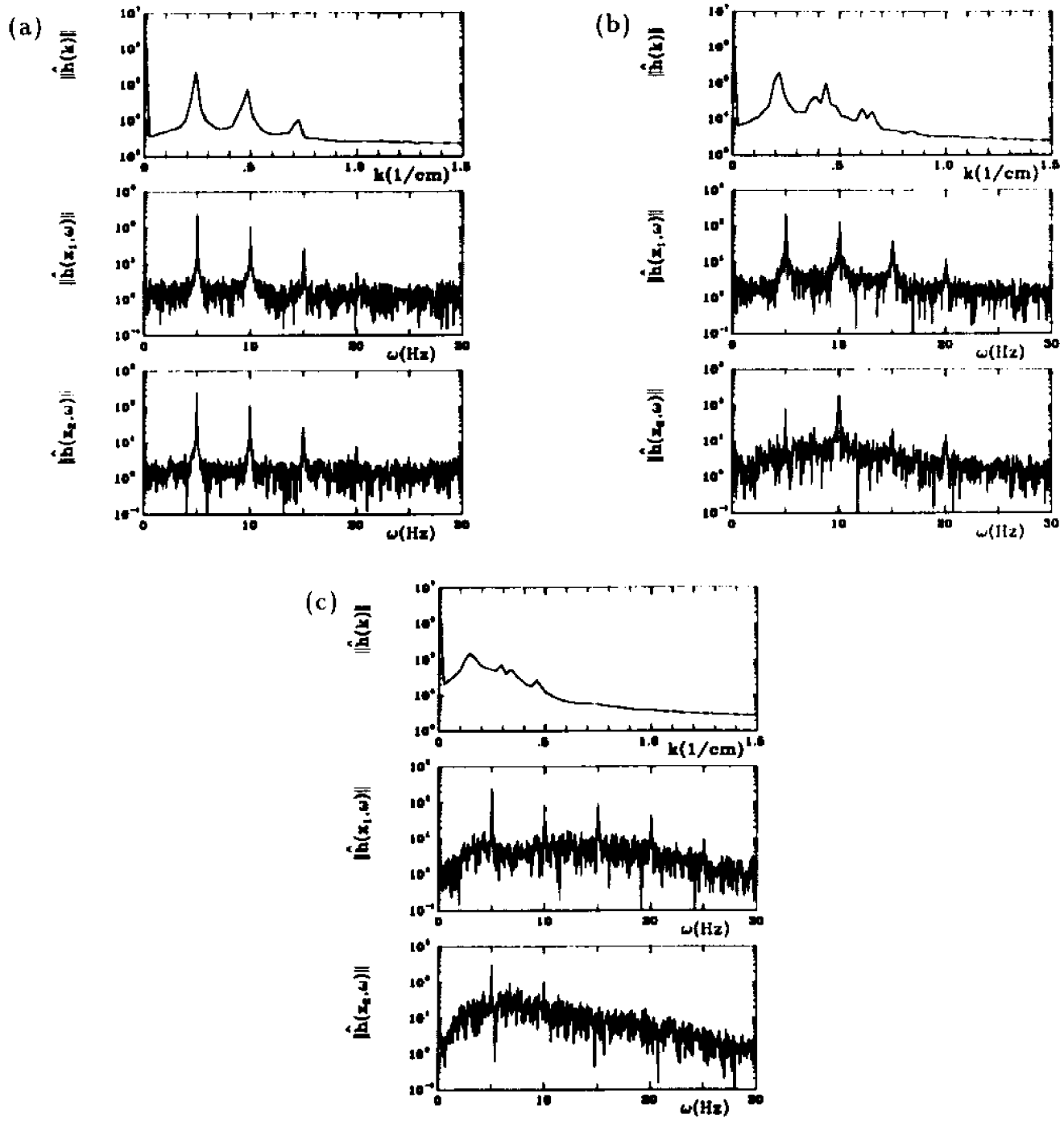

Figure 4.4: One-dimensional spatial Fourier spectra of the film thickness $h(x,t)$ averaged in time (top), and temporal Fourier spectra at fixed positions $x_1 = 10.3$ cm, and $x_2 = 41.1$ cm. (a) $Re = 25.6$, (b) $Re = 35.2$, (c) $Re = 67.7$. The spatial spectrum broadens as Re increases while both the harmonic content and the broad background of the temporal spectrum are augmented.

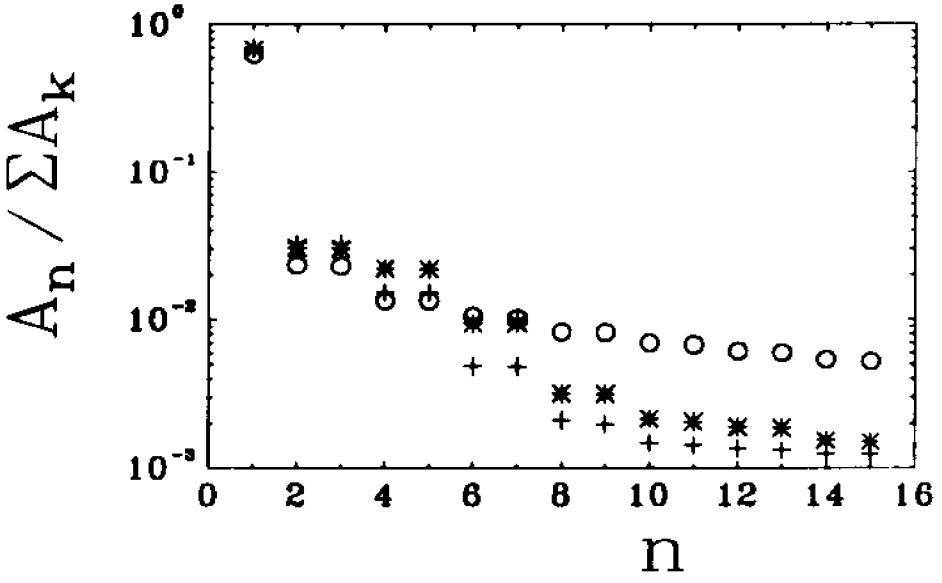

Figure 4.5: First fifteen eigenvalues of the normalized biorthogonal spectra. The crosses correspond to $Re = 25.6$, the asterix to $Re = 35.2$ and the circles to $Re = 67.7$.

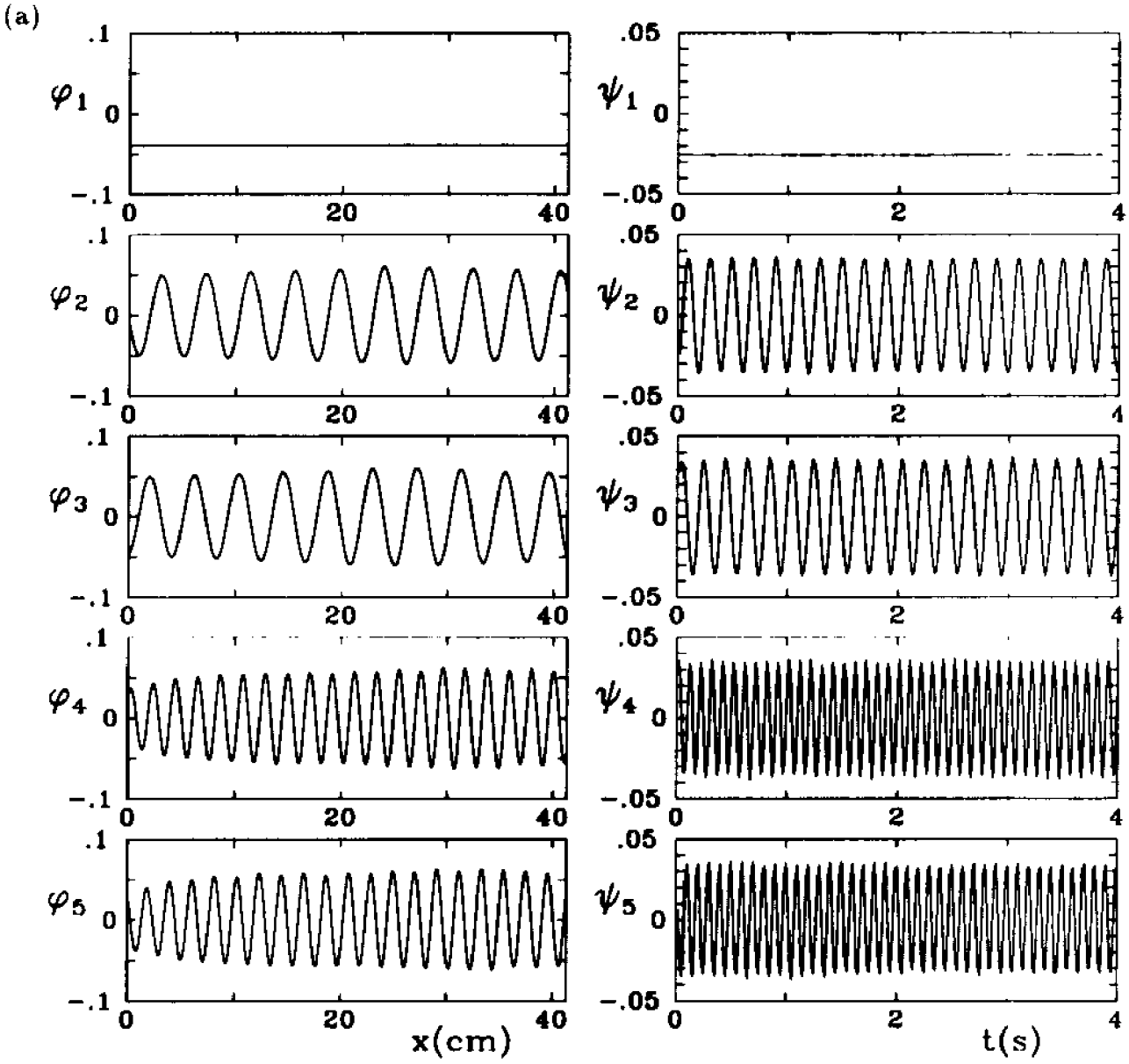

Figure 4.6: Topos $\varphi_1, \varphi_2, \varphi_3, \varphi_4, \varphi_5$ and chronos $\psi_1, \psi_2, \psi_3, \psi_4, \psi_5$. (a) $Re = 25.6$: the φ_n and ψ_n are sinusoids. Next pages, (b) $Re = 35.2$: the φ_n are spatially modulated sinusoids, while the ψ_n are not modulated. (c)$Re = 67.7$: both the φ_n and the ψ_n are modulated sinusoids. The time domain for the representation of the chronos includes only 4 s of the 25.6 s experimental record.

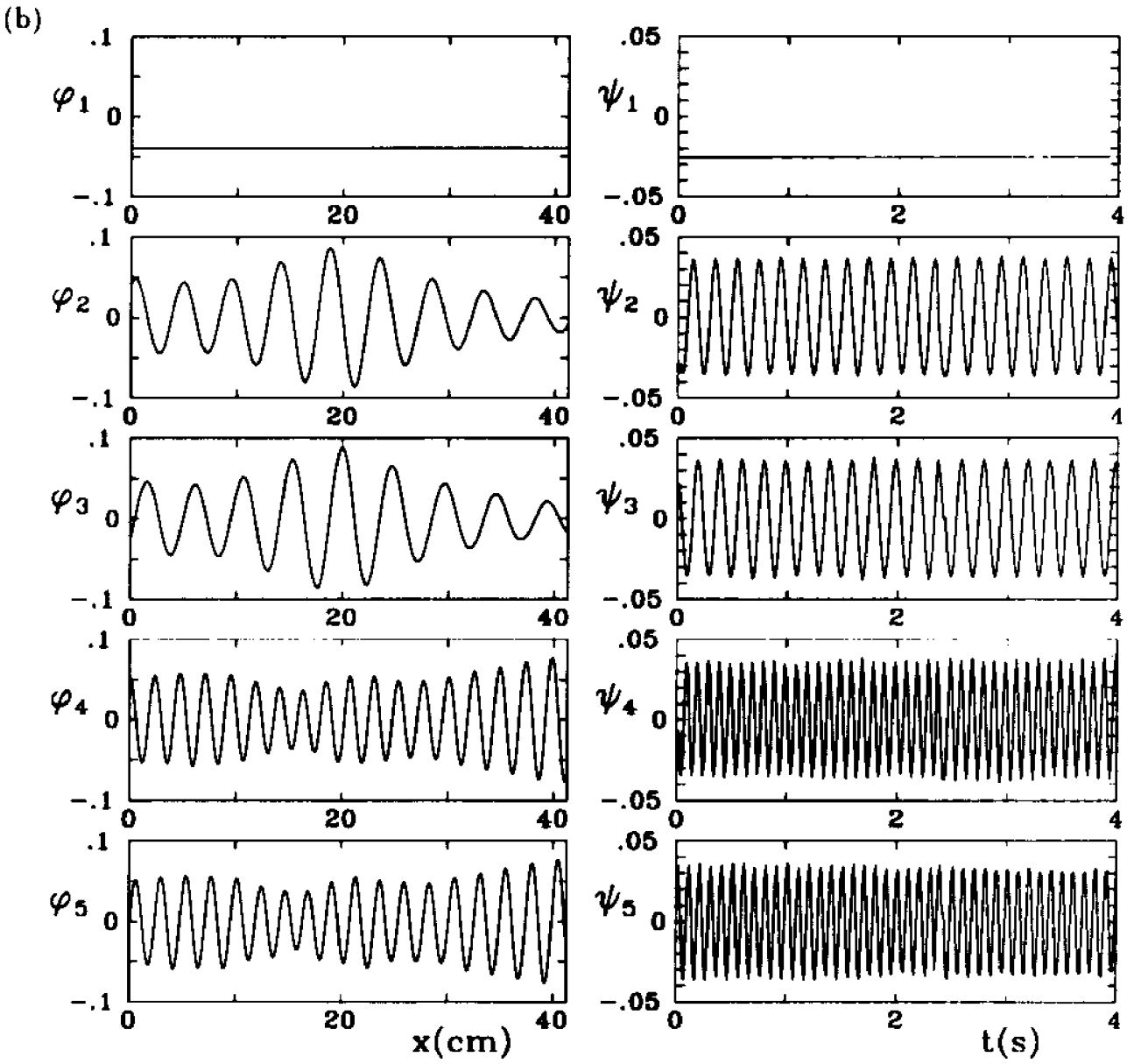

Figure 4.6 continued.

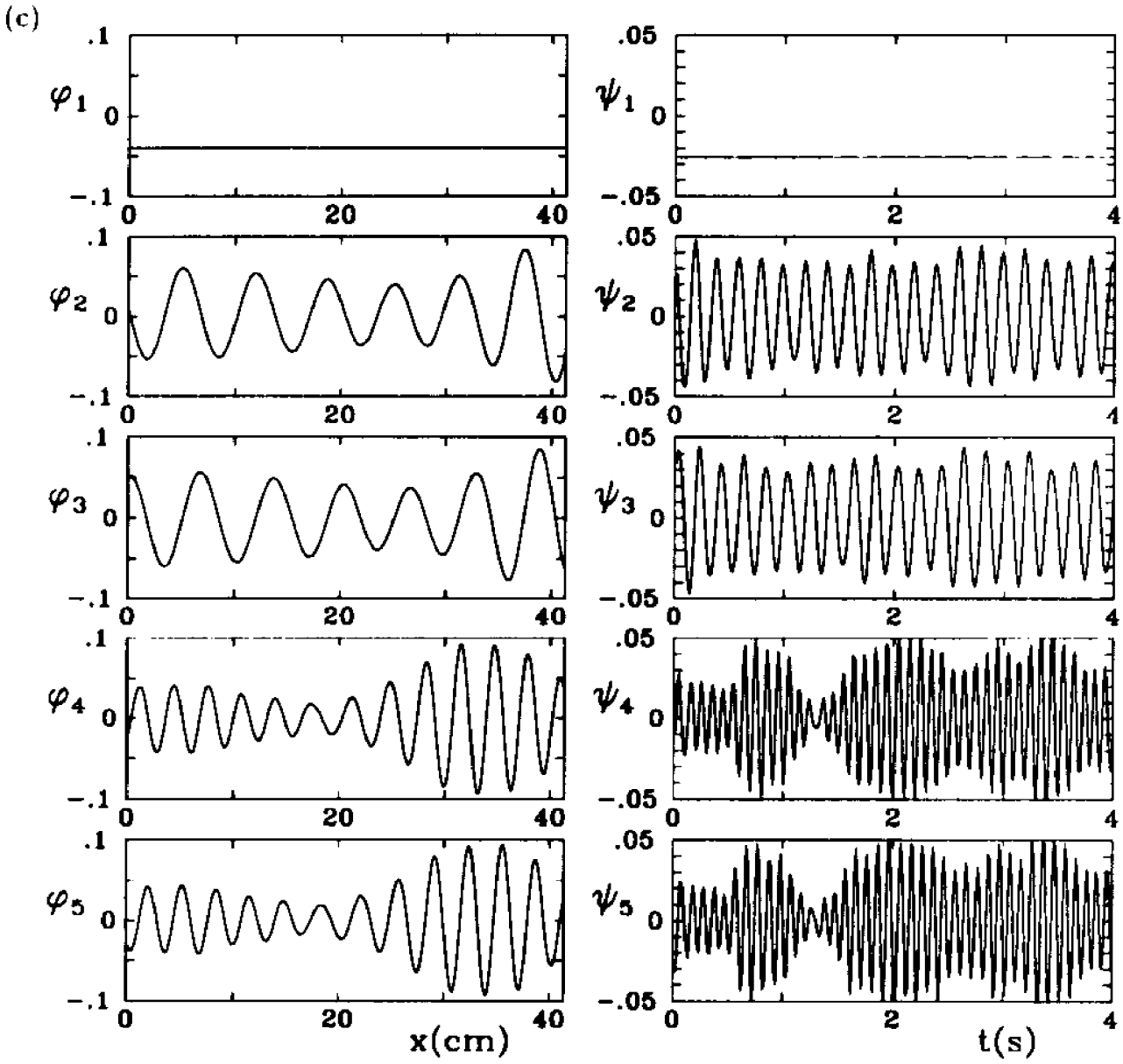

Figure 4.6 continued.

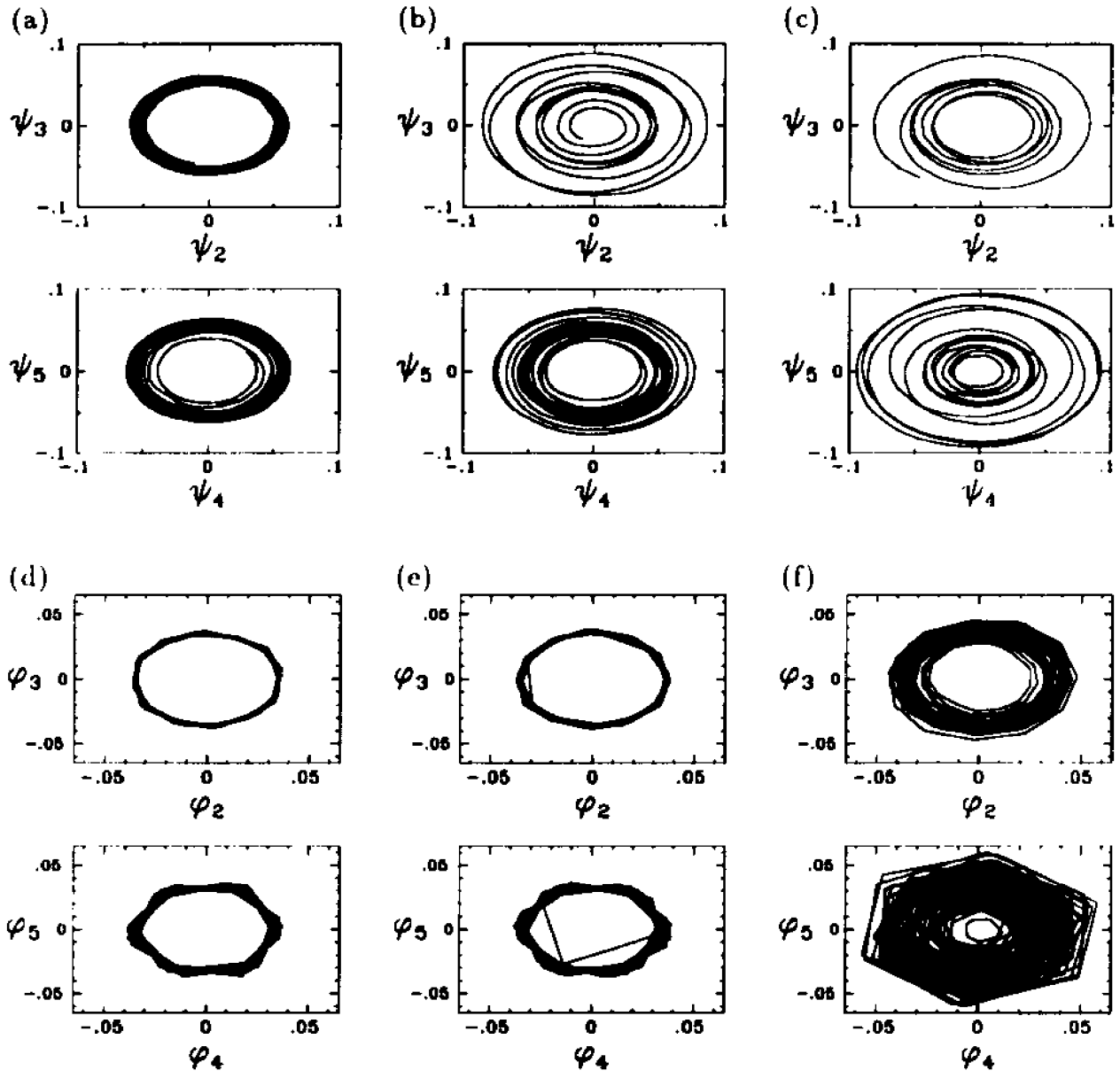

Figure 4.7: (a-c) Projections of the phase space dynamics $\eta_x(t)$ in $\mathcal{X}(T)$ onto the subspace spanned by (ψ_2, ψ_3) and (ψ_4, ψ_5). (a) $Re = 25.6$: the trajectory is a quasi-circle. (b) $Re = 35.2$: the spatial modulation "thickens" the quasi-circle. (c) $Re = 67.7$: the spatial modulation is more pronounced. (d-f) Projections of the phase space dynamics $\xi_t(x)$ in $\mathcal{X}(X)$ onto the subspace spanned by (φ_2, φ_3) and (φ_4, φ_5). (d) $Re = 25.6$: the trajectory is a quasi-circle. (e) $Re = 35.2$: the trajectory remains a quasi-circle. (f) $Re = 67.7$: the quasi-circle is considerably thickened, under the effect of the temporal modulation.

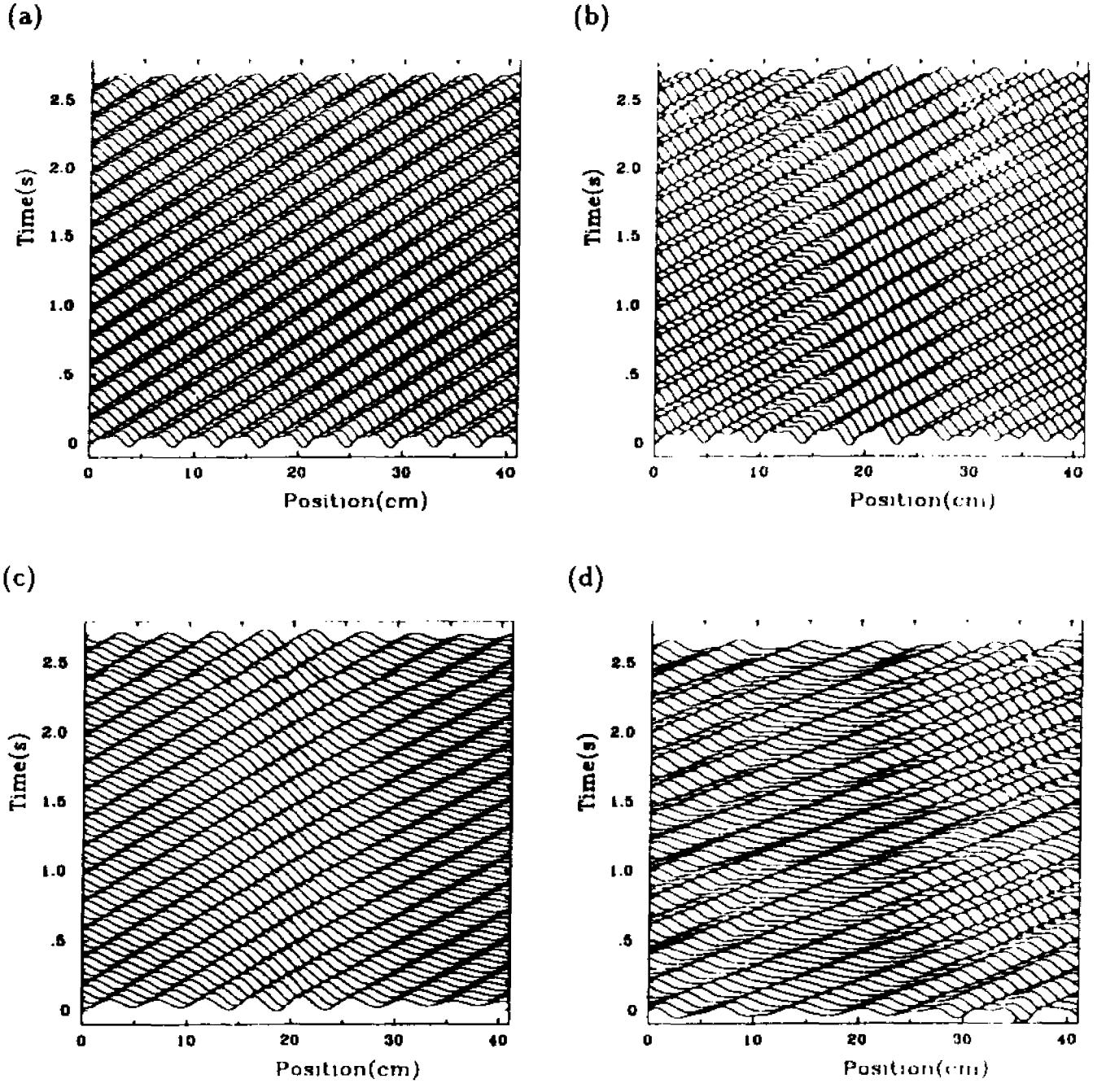

Figure 4.8: Reconstruction of the spatio-temporal representation of the film thickness with the first five modes of (2.4) for three Reynolds numbers. (a) $Re = 25.6$: the wave fronts travel at constant velocity. (b) $Re = 35.2$: the wave fronts split and coalesce as they travel downstream. (c) reconstruction of the film thickness with only the first three terms of the biorthogonal decomposition at $Re = 35.2$. The splittings are lost. (d) reconstruction with the first five terms of the biorthogonal decomposition at $Re = 67.7$: the spatio-temporal character of the modulations is captured

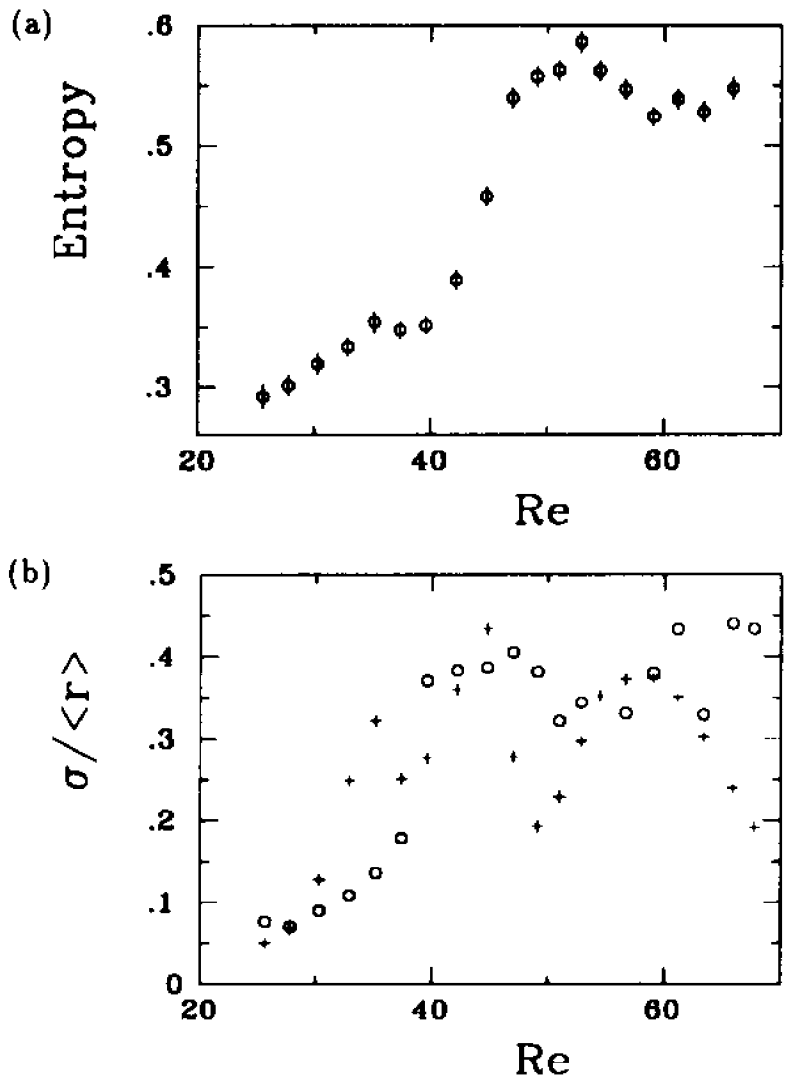

Figure 4.9: (a) Global entropy as a function of the Reynolds number. The large rise in entropy above $Re = 44$ is associated with the transition from spatial to spatiotemporal wave modulations. (b) Normalized standard deviation σ of the distance to the origin of the projections of the vector η_x in the temporal phase space $\mathcal{X}(T)$: Projection $\mathcal{P}_{2,3}\eta_x$ onto the plane (ψ_2, ψ_3) (crosses), projection $\mathcal{P}_{4,5}\eta_x$ onto the plane (ψ_4, ψ_5) (circles).

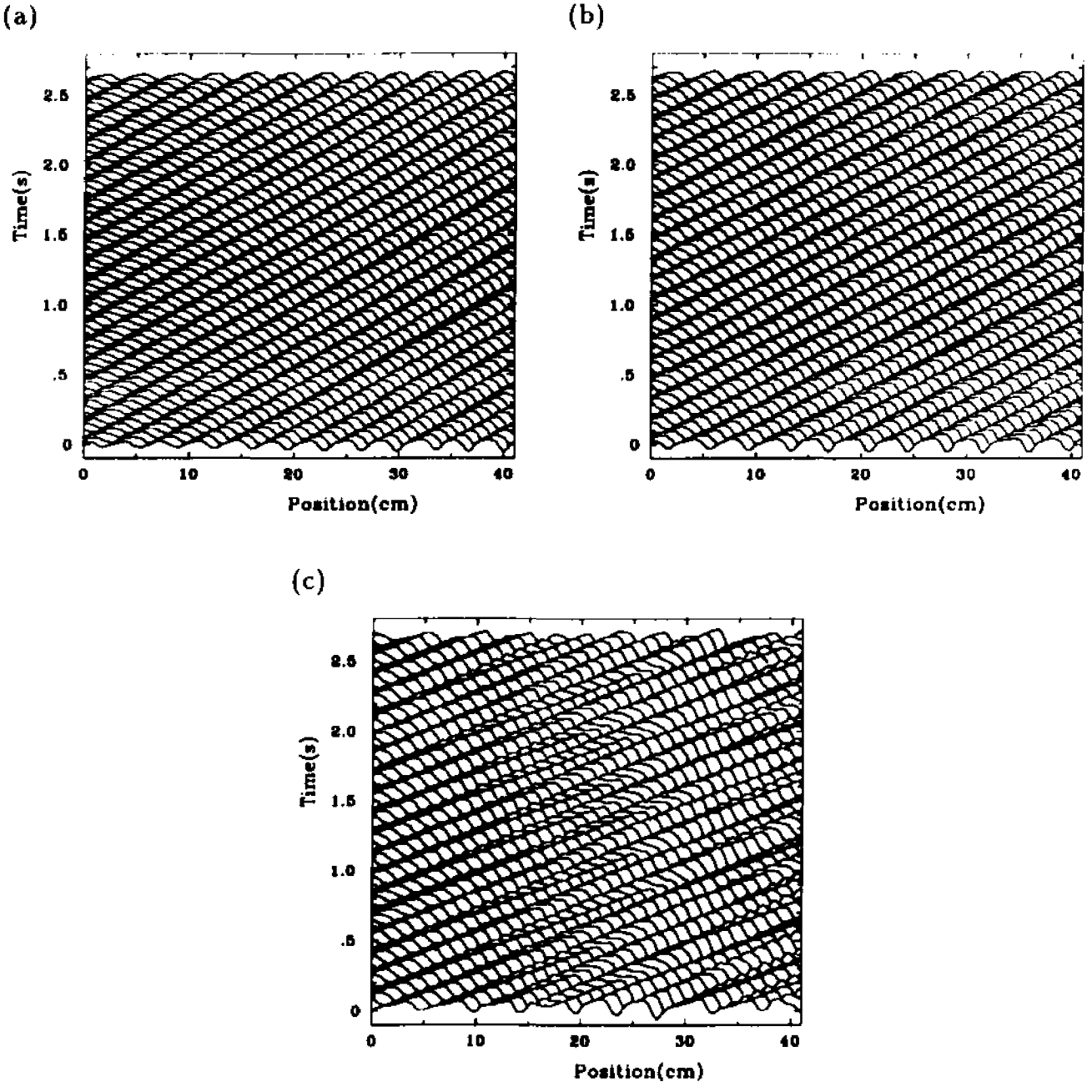

Figure 4.10: Spatio-temporal representation of the film thickness, for $f = 7$Hz, $\beta = 6.4°$ and three Reynolds numbers. (a) $Re = 30.3$: the waves travel at constant velocity; (b) $Re = 39.6$: the halving of the wavelengths is clearly exhibited; (c) $Re = 67.7$ the signal becomes complex in space and time.

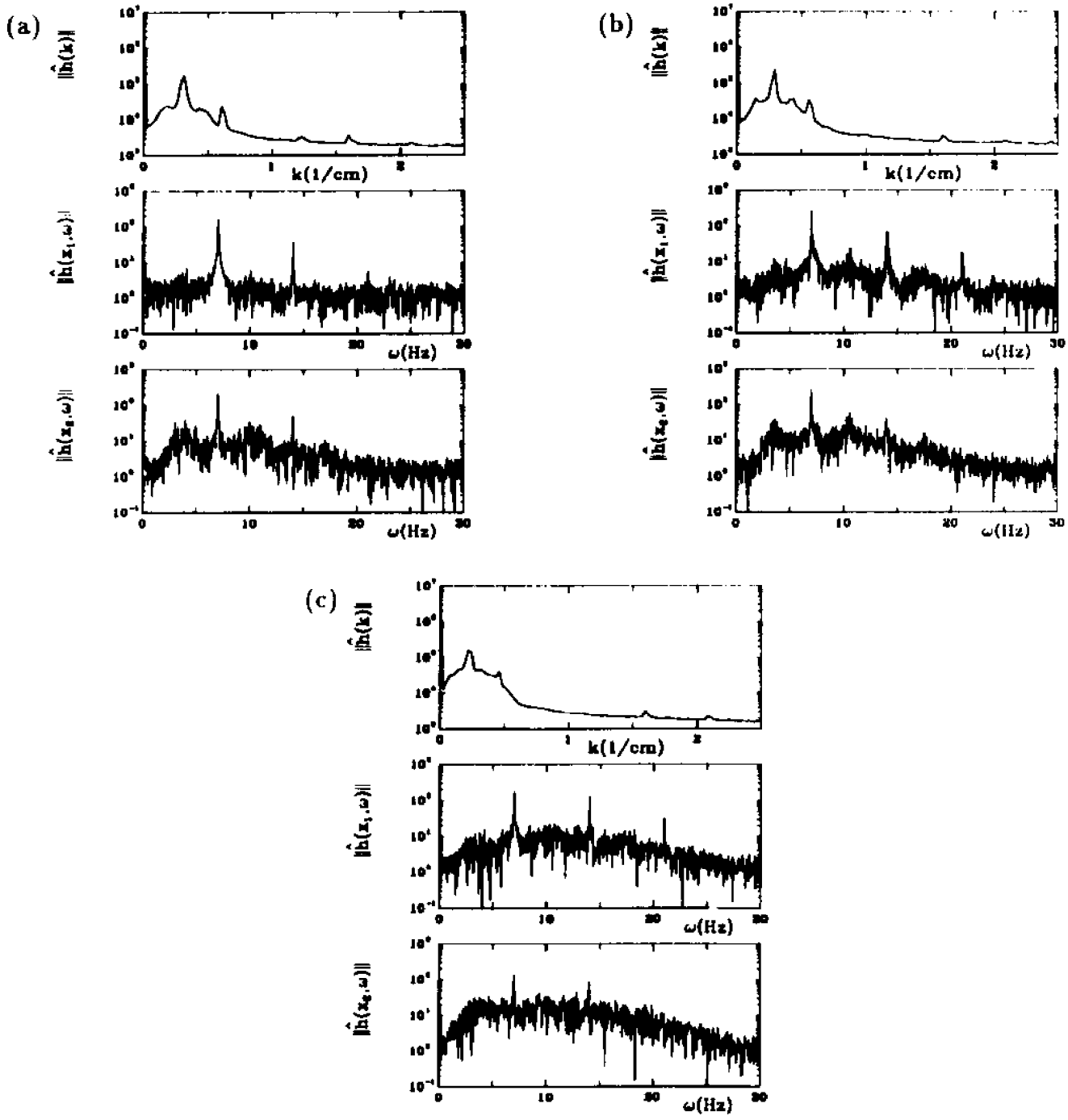

Figure 4.11: One-dimensional spatial Fourier spectra of the film thickness $h(x,t)$ averaged in time (top), and temporal Fourier spectra at fixed positions $x_1 = 10.3$ cm, and $x_2 = 41.1$ cm. (a) $Re = 30.3$: subharmonics are observed only downstream, (b) $Re = 39.6$: both temporal spectra present subharmonics, (c) $Re = 67.7$: the subharmonics disappear in the increasing background noise.

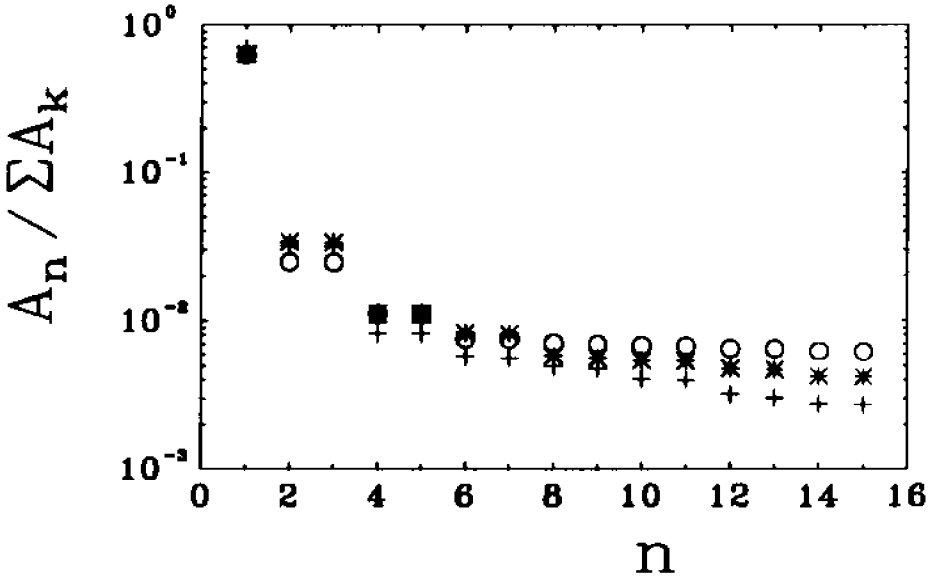

Figure 4.12: First fifteen eigenvalues of the normalized biorthogonal spectra. The crosses correspond to $Re = 25.6$, the asterix to $Re = 35.2$ and the circles to $Re = 67.7$.

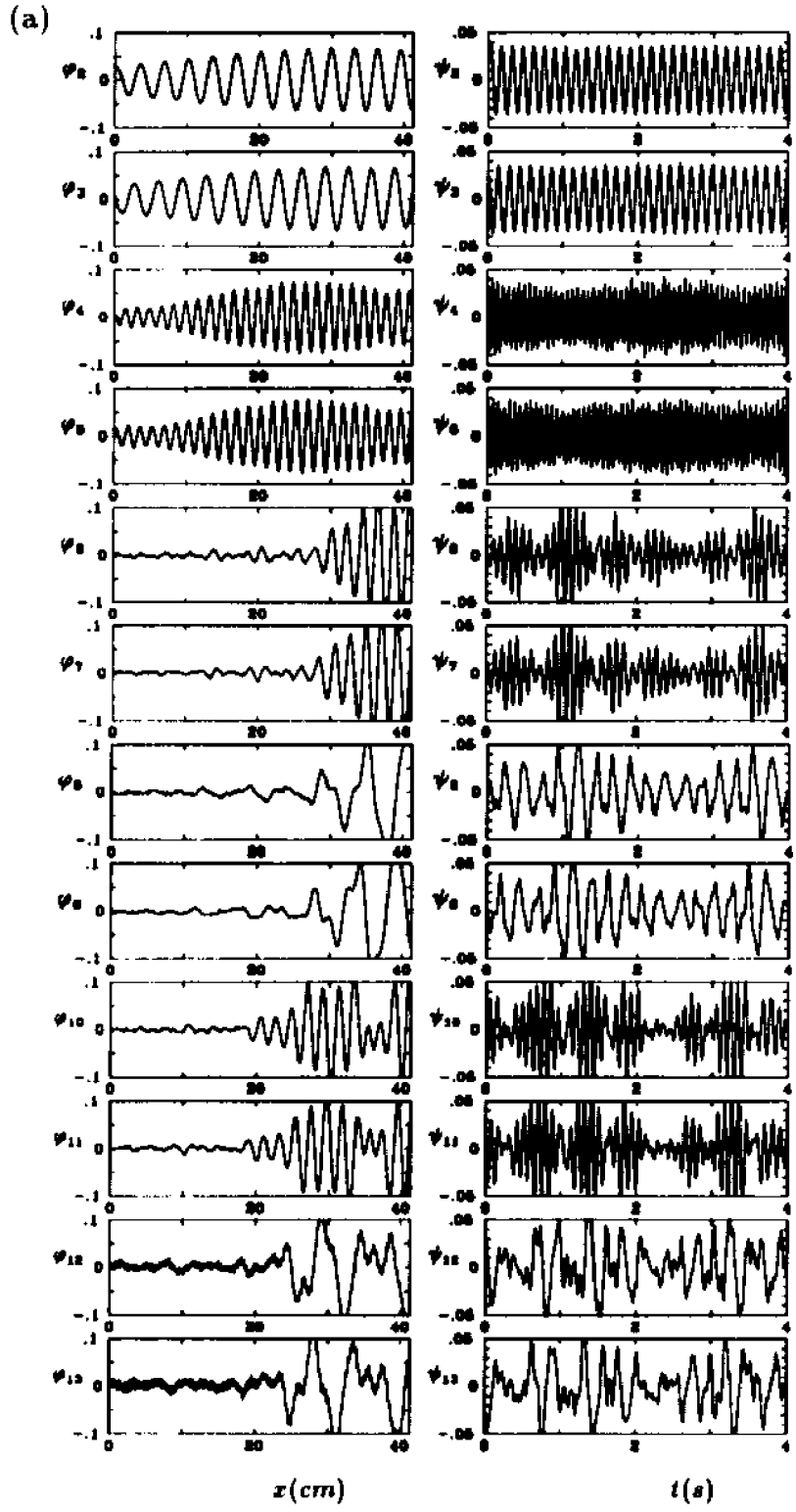

Figure 4.13: Topos φ_2 to φ_{13} and chronos ψ_2 to ψ_{13}, and their respective Fourier representation $\hat{\varphi}_2, \ldots, \hat{\varphi}_{13}$ and $\hat{\psi}_2, \ldots, \hat{\psi}_{13}$. (a) and (b) $Re = 30.3$; (c) and (d) $Re = 39.6$; (e) and (f) $Re = 67.7$. (See next pages for (c), (d), (e), and (f)).

(b)

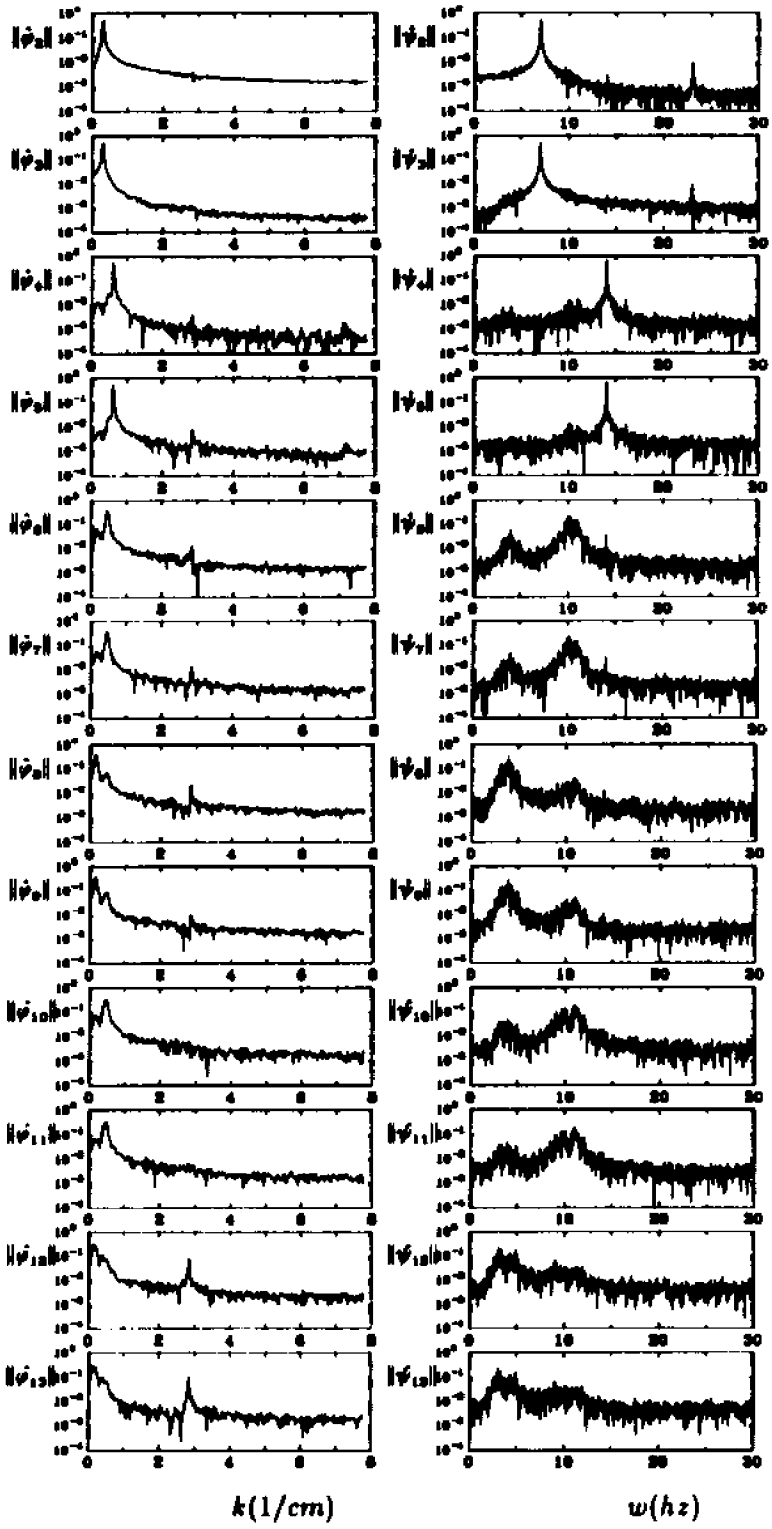

Figure 4.13 continued

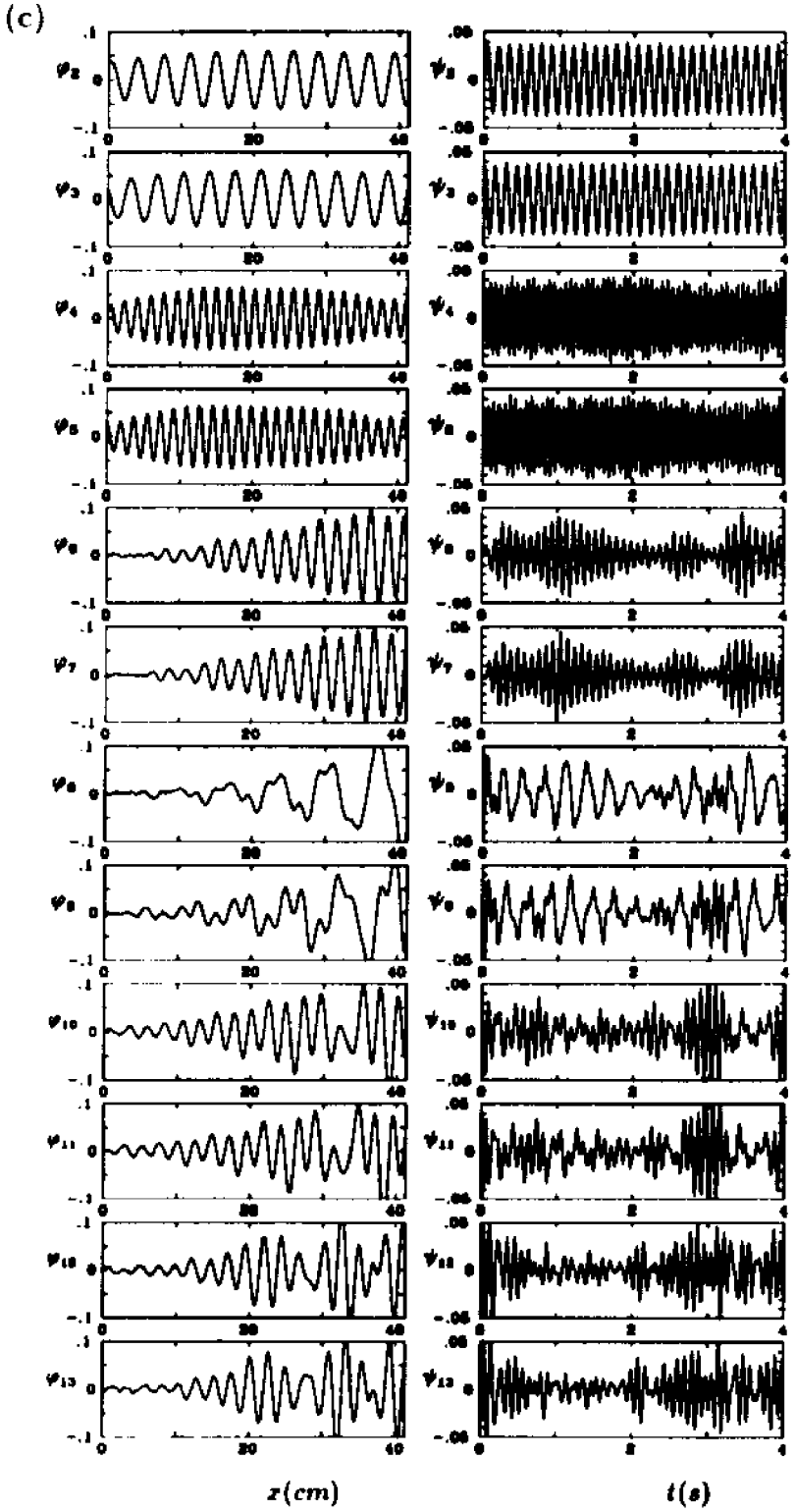

Figure 4.13 continued

(d)

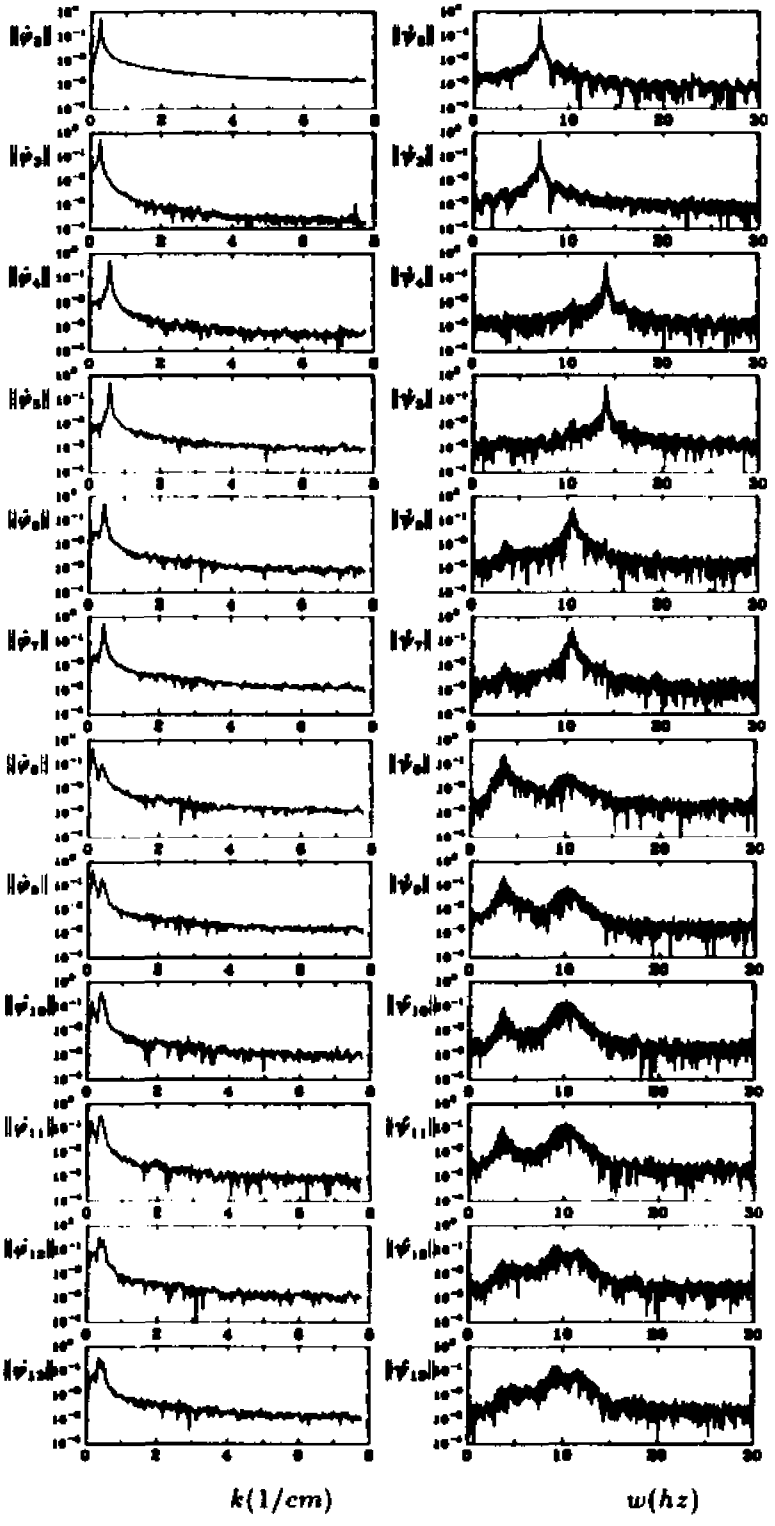

Figure 4.13 continued

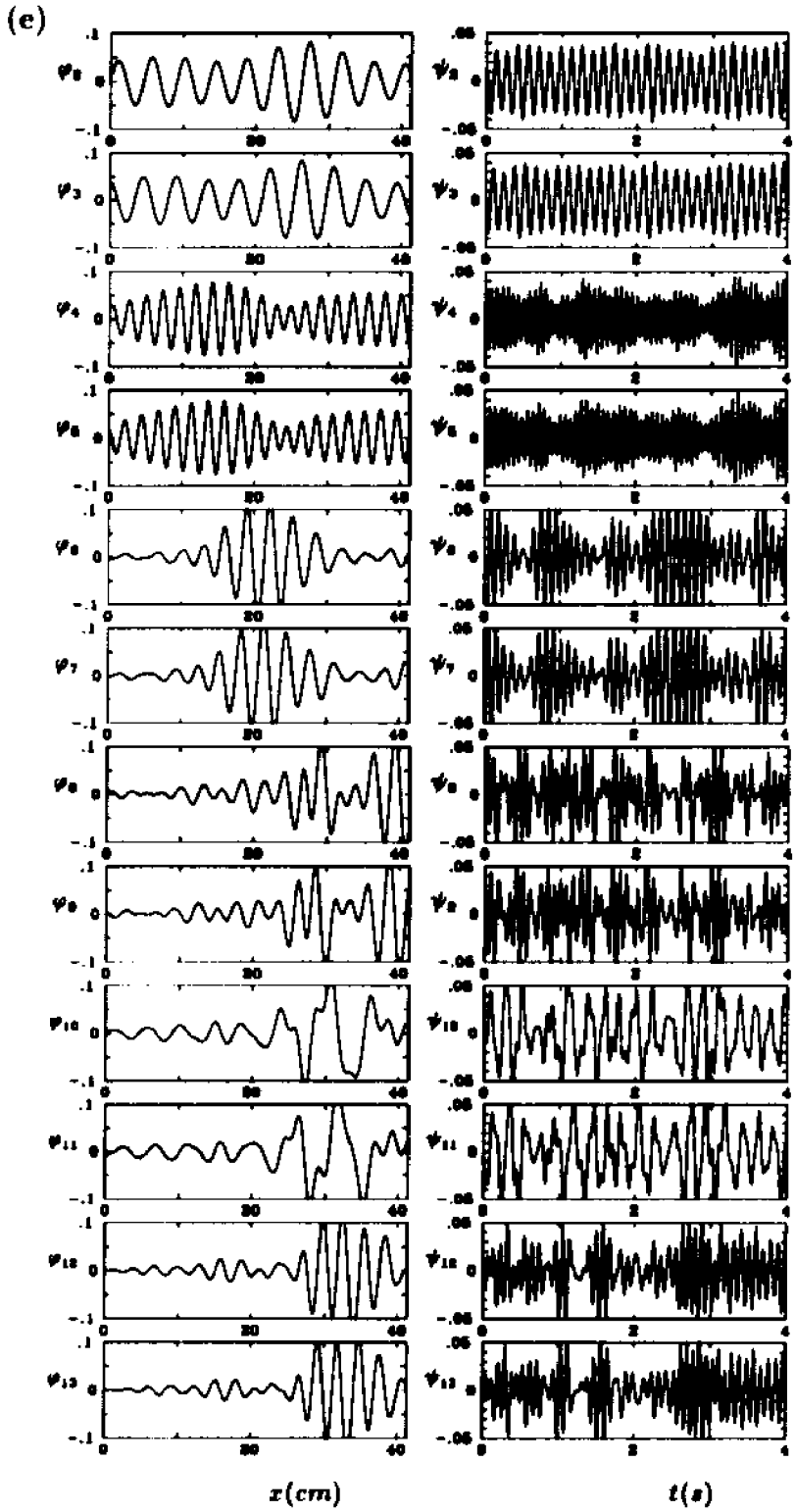

Figure 4.13 continued

(f)

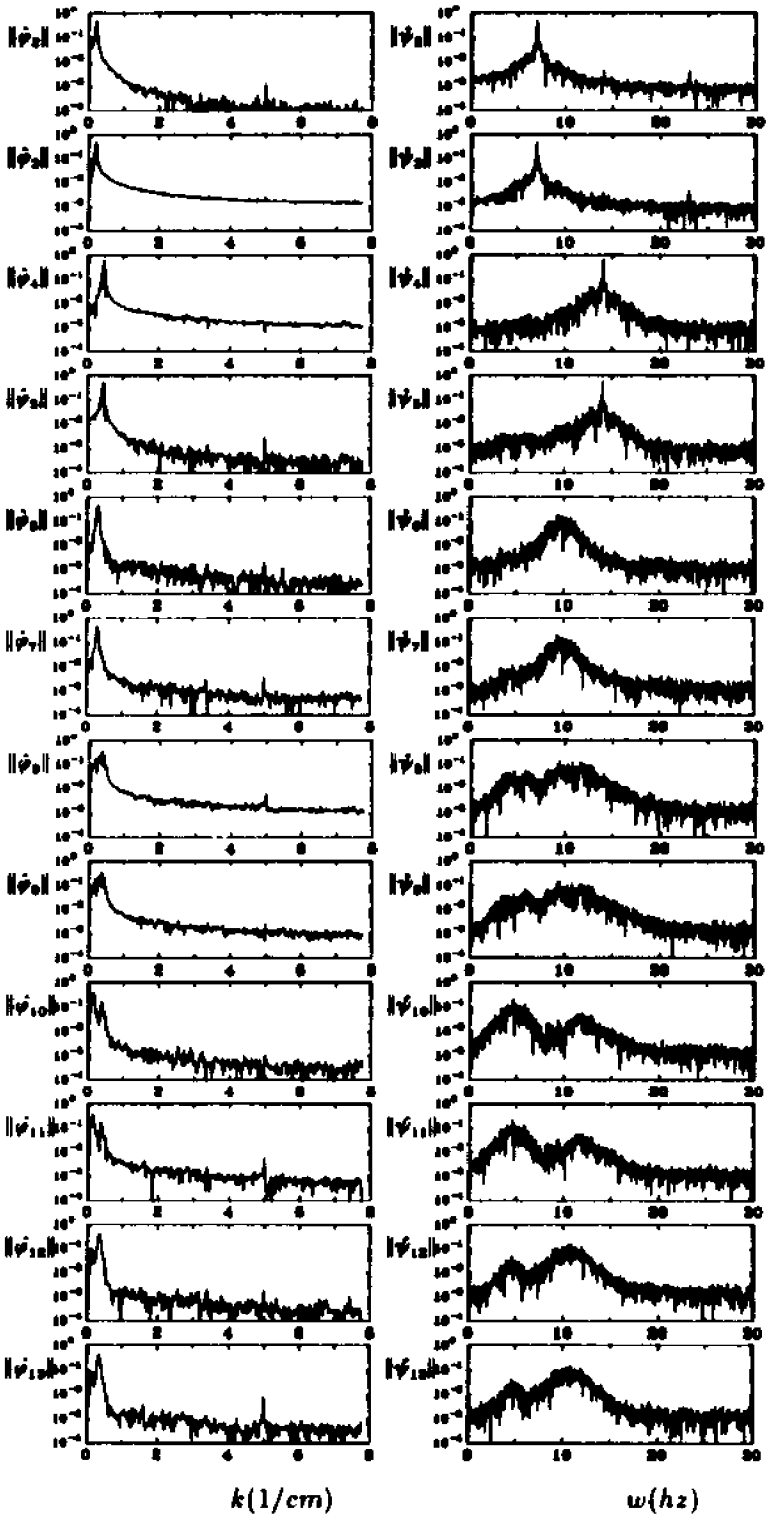

Figure 4.13 continued.

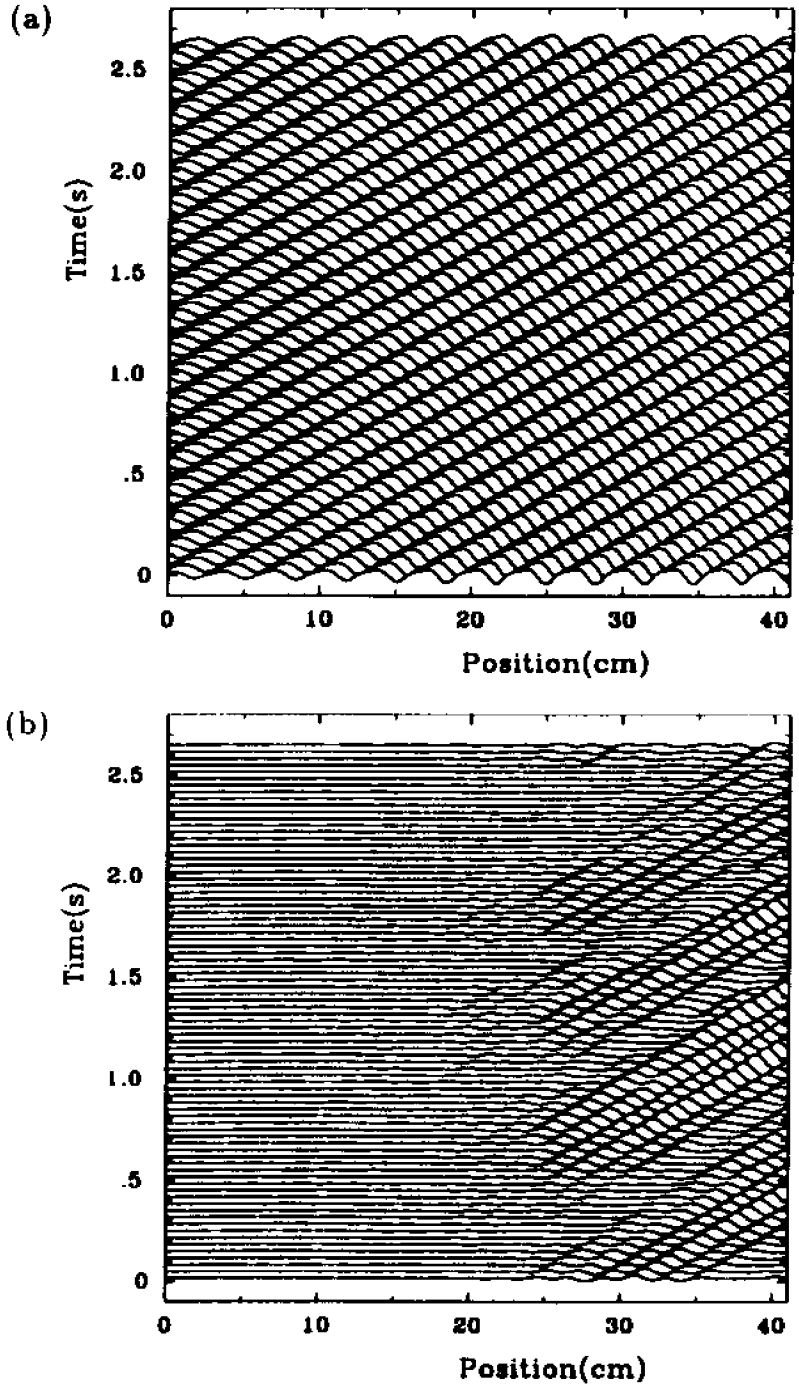

Figure 4.14: Reconstruction of the spatio-temporal representation of the film thickness for three Reynolds numbers. (a) $Re = 30.3$, modes 1 to 5, the wave fronts grow in amplitude as they travel downstream at constant velocity; (b) $Re = 30.3$, modes 6 to 13, the flow is amplified at the end of the spatial window, the convective character of the subharmonic modes is clear. Continues in next pages.

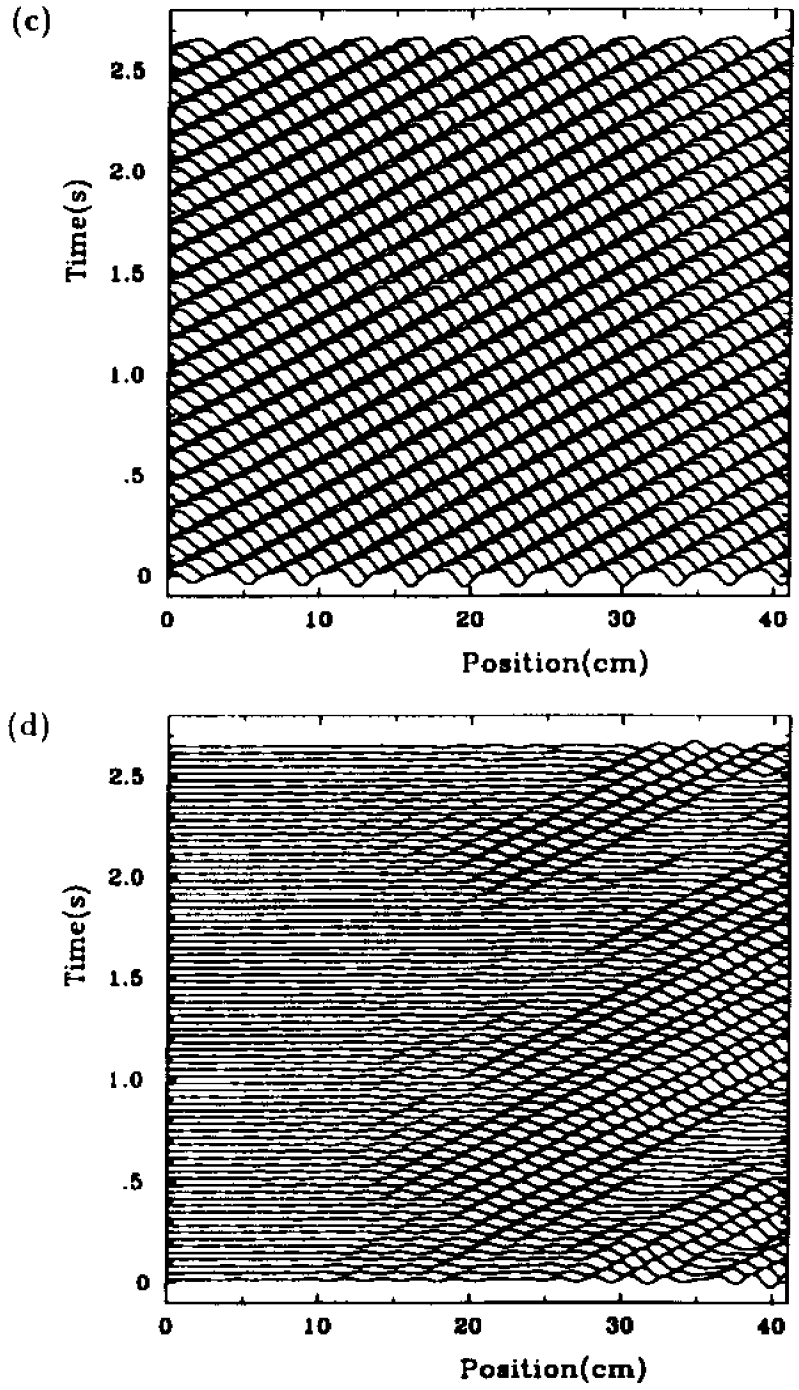

Figure 4.14 continued. (c) Re = 39.6 modes 1 to 5, the waves move at constant speed without deformation; (d) Re = 39.6 modes 6 to 13: the spatio temporal period doubling now becomes clear.

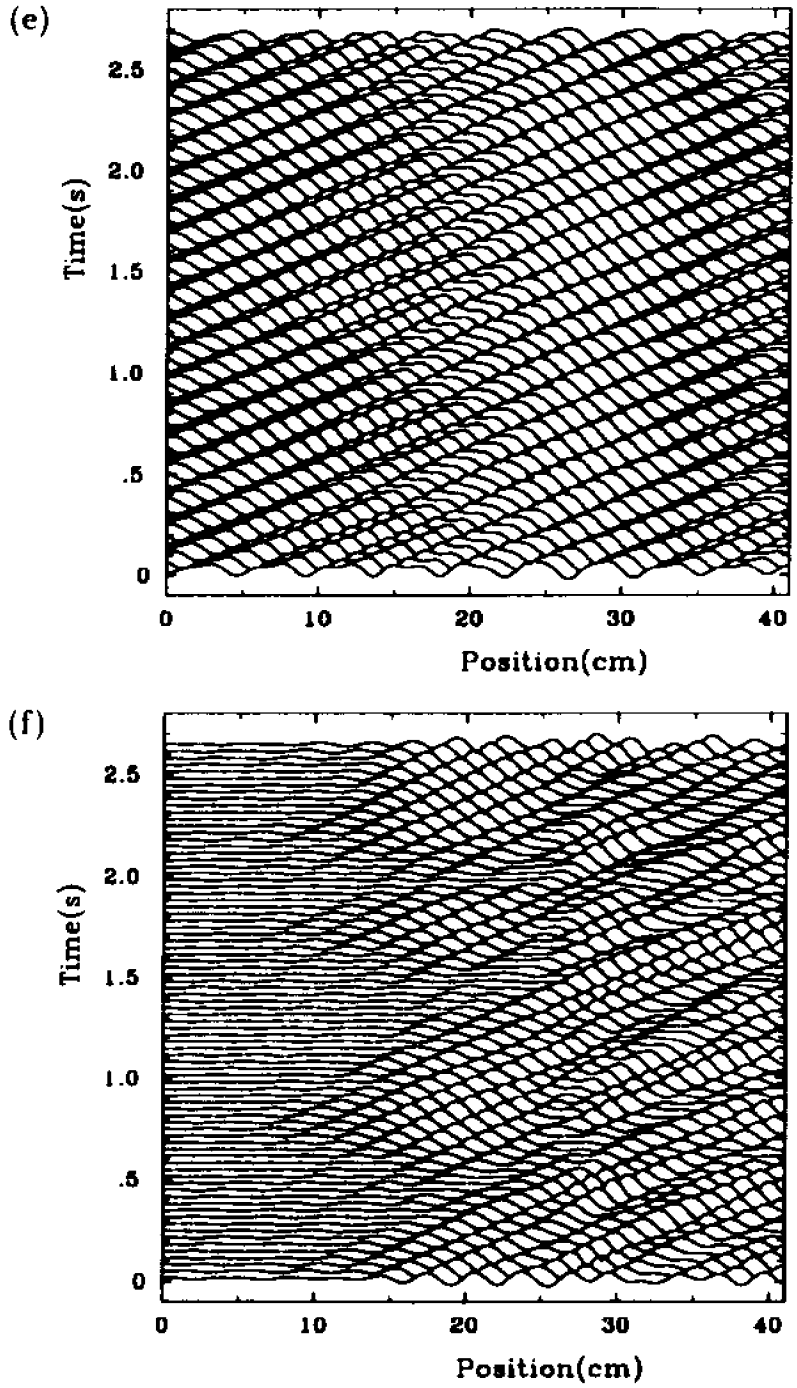

Figure 4.14 continued. (e) reconstruction of the film thickness with the first five terms of the biorthogonal decomposition at $Re = 67.7$: the split and coalesce of the waves is captured; (f) $Re = 67.7$ modes 6 to 13: spatiotemporal structures are greatly amplified in an intermitent process.

Chapter 5

Wall Bounded Shear Flows

The Navier-Stokes equations (1.1) are invariant under various symmetries. In this chapter I concentrate on the already studied spatio-temporal scaling invariance (see Chapter 2):

$$\begin{aligned} \boldsymbol{x} &\longrightarrow \lambda \boldsymbol{x} \\ t &\longrightarrow \lambda^{1-h} t \\ \nu &\longrightarrow \lambda^{1+h} \nu \\ \boldsymbol{u} &\longrightarrow \lambda^{h} \boldsymbol{u} \end{aligned} \tag{5.1}$$

for all $\lambda \in \mathbf{R}_{>0}$ and $h \in \mathbf{R}$. Note that the transformation includes the rescaling of ν, which keeps the Reynolds number constant, i.e. scale invariant. This property implies that, if $\boldsymbol{u}(\boldsymbol{x}, t)$ is a solution, then $\lambda^h \boldsymbol{u}(\lambda \boldsymbol{x}, \lambda^{1-h} t)$ is also solution, at the same Reynolds number. It is then reasonable to assume that the flow itself $\boldsymbol{u}(\boldsymbol{x}, t)$, in its turbulent state, is self-similar: it satisfies the stretching symmetry (5.1) in the "inertial range" (see eq. (2.23)). As recalled in the introduction, this is consistent with Kolmogorov's conception of turbulence and the energy cascade: as the length and time scales stretch (or compress), the flow, together with its energy, are renormalized. This property was explicitly used in the derivation of Fourier spectral laws of homogeneous turbulence

(see, e.g., references [1, 2]). This is a generalization of dimensional analysis using Lie group theory [3, 4]. The two-parameter stretching group of symmetries (5.1) is also discussed by Cantwell [5] who shows that the flow from a round jet is self-similar at all Reynolds numbers.

I now assume the flow invariant under the scale transformations (5.1) [6]. Although the Navier-Stokes equations are invariant under all transformations (5.1) corresponding to any exponent h and any (spatial) stretching factor $\lambda > 0$, I suppose, without loss of generality, that $\lambda > 1$. In addition, a specific symmetry group determined by a specific value of h (λ being the group element) can be selected by a conservation law which leaves a certain quantity invariant under the scale transformations (5.1). If this scale invariant quantity is the energy transfer (or, equivalently, the dissipation rate), then $h = 1/3$ in (5.1) [7]. In case of an homogeneous flow, this leads, as we recalled in the introduction, to Kolmogorov's spectrum law. This scaling holds only in the so-called inertial range of length scales l:

$$\eta \ll l \ll L$$

where η and L are the Kolmogorov length scale and the integral length scale.

Even when the translation symmetry hypothesis no longer holds (non-homogeneous turbulence), the previous scaling argument still holds [8]. But, due to the inhomogeneity of the flow, the Fourier basis is, however, no longer adapted to the dynamical stretching of the flow (5.1). Instead, an alternative spectral space directly related to $\boldsymbol{u}(\boldsymbol{x}, t)$ needs to be considered [9]. As seen in Chapter 2, the bases provided by biorthogonal decompositions are the best suited for this task. In fact dynamical functions with the above symmetry (5.1) are already studied in Section 2.2.3. In this case, there exists a hierarchy of orthogonal modes (2.4) which are all generated by stretching a basic "mother" mode (see equations (2.26) and (2.27)).

In this chapter, I extend the results from Section 2.2.3 to the case of finite boundary conditions. I thus obtain two scalings: the first one along the modal spectrum, the other one within each eigenfunction as the wall is approached. The dilation operator (2.25) is then explicity given, and the extended model of non-homogeneous, wall-bounded shear turbulence is tested on a direct numerical simulation of a turbulent channel flow.

5.1 The Stretching Symmetry for Wall-bounded Shear Flows

5.1.1 Scaling, along the spectrum

The symmetry

In this section I investigate the influence of a finite spatial domain, such as that confined between walls, onto the scaling symmetry previously discussed. In other words, can the spatial eigenmodes of a turbulent boundary layer be deduced from a few basic mother modes and what is the expression of the mapping leading to a recurrence relation among the eigenvalues and eigenmodes? In the following, I concentrate on one mother and its images by symmetry. In order to orient the analysis toward the channel flow which will be analyzed in the next section, I concentrate on an antisymmetric (or symmetric) mode and its family. (Very few modifications need to be made for other wall-bounded flows such as boundary layers, pipe flows, etc.) For the sake of simplicity, I consider one component of the mode considered. As recalled in Chapter 2, I can always assume that this mode is either odd or even in the direction (y) normal to the wall (see Fig. 5.1). Although the modes φ_n depend on x, y, and z, I now concentrate on their variation with distance to the wall only.

Without loss of generality, I suppose that the walls are located at $y = \pm 1$.

Since stretching occurs as an inverse energy cascade process (as the mode index decreases), the operation needs to be applied from the least energetic mode (at the tail of the inertial range), which will, hereafter, be considered as the mother mode, say φ_N. The latter has its smallest length scale (adjacent to the wall) of the order of the Kolmogorov's length scale of the flow, η. Successive stretchings of φ_N are now considered in the y-direction. More precisely, I dilate the mother φ_N in order to obtain φ_{N-1}, the mode φ_{N-1} in order to obtain φ_{N-2}, etc. Since stretching in a finite domain takes a part of the function outside of the domain, dilation needs to be carried out toward the boundaries, i.e. toward the walls. In addition, the presence of the (statistical) reflection symmetry makes this action invariant under reflection with respect to the center of the channel. Stretching thus carries a part of φ_{n+1} beyond the walls, in a manner which *must* guarantee the no-slip boundary condition at the wall, i.e. $\varphi_n(y = \pm 1) = 0$, namely the dilation is applied until the zeroe closest to the wall in φ_{n+1} reaches $y = \pm 1$ in φ_n. In this process, each wall absorbs a zeroe at each iteration of the mapping so that the mode φ_n has two zeroes less than φ_{n+1}. (Note that, for a boundary layer, only one zeroe will be absorbed.)

I now concentrate on the odd mode series only (the extension of the analysis to the even mode series is straightforward). Each function $\varphi_{n,odd}$ has at least three zeroes, two at the walls (due to the no-slip boundary condition) and one at the center of the channel (due to the oddness of the functions considered). In addition, the first mode in this set, characteristic of large scale structures, has only the three previous zeroes. This point, together with the absorption of two zeroes by the walls at each step of the iteration process, implies that mode $\varphi_{n,odd}$ has exactly $2n + 1$ zeroes (similarly, even

modes have $2n$ zeroes). These properties can be summarized in the following form

$$\begin{aligned} \varphi_{n,odd}(z_i^{(n)}) = 0, \quad & -n \leq i \leq n \\ z_0^{(n)} \;\; = \;\; & 0 \\ z_{\pm n}^{(n)} \;\; = \;\; & \pm 1, \end{aligned} \tag{5.2}$$

where I have indexed the zeroes, $z_i^{(n)}$, from the center of the channel and $i \in \mathbb{Z}$.

I then return to the stretching procedure, starting from $\varphi_{N,odd}$. For this, I consider a point P of φ_N located at distance $y^{(N)}$ from the center of the channel, $y = 0$. Under the stretching action, the corresponding point in $\varphi_{N-1,odd}$ is located at a distance $y^{(N-1)}$ from $y = 0$, larger than $y^{(N)}$ by a factor precisely equal to the stretching factor, say λ. The same operation can be repeated N times until the first mode is reached, so that all the points issued from P and belonging to all modes in the series considered, can be drawn. I now reiterate the procedure for all points in $\varphi_{N,odd}$. In particular, I consider a point P' of $\varphi_{N,odd}$ very close to the wall. It is clear that the stretching factor there, limited by the presence of the wall, has to be close to one. This remark results in the dependency of the stretching factor on the location of the point considered in the mother. This dependency of the dilation coefficient on the index of the point considered indicates that the original dilation symmetry (2.24) and (2.25) gets deformed under the influence of the wall boundary conditions. While the process permitting the deduction of a function of order n from its predecessor of order $(n-1)$ consists in stretching, the latter depends on the location of the point considered in the mother.

Although the previous remarks are valid independently of the point considered within $\varphi_{N,odd}$, zeroes play a particular role since two of them coincide with the boundary conditions of the problem. In addition, it is difficult, in practice, to follow *any* point through the stretching process. In contrast, zeroes are easy to identify and follow. Indeed, the image of the i-th zeroe in the n-th mode through stretching remains

the i-th zeroe in the $(n-1)$-st mode (for $-(n-1) \leq i \leq (n-1)$, $i \in \mathbb{Z}$). This property allows to compute the stretching factor as a function of the zeroe index. The distance corresponding to any other point located between the i-th zeroe and the $(i+1)$-st zeroe will be denoted $y_j^{(n)}$, where j is a *real number* between i and $i+1$. Note that when j is an integer, $y_j^{(n)}$ coincides with $z_{i,odd}^{(n)}$. In all cases, j is an index which permits to identify a point in the mother and follow it through the stretching process. According to our previous discussion, the ratio between the distance of the i-th zeroe in two consecutive modes $\varphi_{n-1,odd}$ and $\varphi_{n,odd}$ is independent of n. It is, however, a function of the zeroe index i, so that

$$z_i^{(n-1)} = \lambda_i \, z_i^{(n)}, \quad n \in \mathbf{N} \quad i \in \mathbf{Z}. \tag{5.3}$$

More generally, the stretching factor, for any point, is a function of the generalized index j, so that

$$y_j^{(n-1)} = \lambda_j \, y_j^{(n)}, \quad n \in \mathbf{N} \quad j \in \mathbf{R}. \tag{5.4}$$

I now assume that λ_j leads to an invertible function $y_j^{(n-1)}(j)$ which permits the derivation of an indexation procedure $j(y_j^{(n)})$. This will be used below in 5.1.3.

The location of the zeroes

While all formulae in this paragraph can be written for any point $y_j^{(n)}$, the analytical expressions are slightly more complex than in the case of zeroes. For this reason, I concentrate on the zeroes only. By applying the stretching (5.3) $(n-i)$ times and using the no-slip boundary condition (5.2) at the walls, I obtain a relation connecting the locations of the zeroes $z_i^{(n)}$ and the stretching factors λ_i

$$z_i^{(n)} = \lambda_i^{i-n}, \tag{5.5}$$

which is an exponential law in n, for a fixed i. This relation, linking the shape of the modes to the symmetry itself, is crucial.

The logarithm of (5.3) gives the following linear law in n

$$ln(z_i^{(n)}) = na_i + b_i, \tag{5.6}$$

where $\lambda_i = e^{-a_i}$ and $b_i = -ia_i$. Equation (5.3) implies that there is a direct relation between the location of the zeroe closest to the wall, $z_{n-1}^{(n)}$, in the n-th mode and the stretching factor λ_{n-1}:

$$z_{n-1}^n = \lambda_{n-1}^{-1}.$$

Note that

$$l_n = 1 - z_{n-1}^{(n)} = 1 - \lambda_{n-1}^{-1}$$

is the distance to the wall of the first zeroe, or, equivalently, the smallest length scale, in the n-th mode. As we mentioned earlier, it should coincide with the Kolmogorov length scale, η, for the mother ($n = N$), that is $l_N = \eta$.

5.1.2 Scaling, as the wall is approached

I now use the similarity between the cascade of energy to small scales down the energy spectrum and the compression of scales in physical space, as the wall is approached [10]. This analogy implies that stretching also takes place at each energy level. In other words, the length scale increases with distance to the wall *within each eigenmode*. Again, I restrict the analysis to the zeroes only and identify a length scale with the distance between two consecutive zeroes (although a generalization can be extended to all points). The compression, at constant energy level, can be expressed as

$$z_{i+1}^{(n)} - z_i^{(n)} = c_n(z_i^{(n)} - z_{i-1}^{(n)}) \tag{5.7}$$

where c_n is the compression factor ($c_n < 1, \forall n \in \mathbf{N}$). Exactly like λ depends on the index i of the zeroe, c depends on the index n of the mode. In particular, as λ_i tends to 1 as the wall is approached (i tends to infinity), c_n tends to 1 in the tail of the spectrum (n tends to infinity).

Applying the compression rule (5.7) $(n-i)$ times, I obtain the difference between two consecutive zeroes as a function of $l_n = 1 - z_{n-1}^{(n)}$, the smallest length scale (or distance of the last zeroe to the wall) within the mode of order n:

$$z_i^{(n)} - z_{i-1}^{(n)} = (c_n)^{i-n} l_n,$$

which is an exponential law in i, for a fixed n. This implies that the location of each zeroe can be expressed as a function of the smallest length scale and the compression factor c_n, i.e. $z_i^{(n)} = l_n (c_n)^{1-n}((c_n)^i - 1)/(c_n - 1)$. Now, using the relation between l_n and c_n,

$$l_n = \frac{(c_n - 1)(c_n)^{n-i}}{(c_n)^n - 1}, \tag{5.8}$$

and the boundary conditions at the wall (5.2), I can write the locations, $z_i^{(n)}$, of all zeroes as a function of the compression factor c_n:

$$z_i^{(n)} = \frac{(c_n)^i - 1}{(c_n)^n - 1} \tag{5.9}$$

or, equivalently, as a function of the smallest length scale l_n per mode, l_n being the unique, real positive root of (5.8). This equation is the equivalent of (5.5): its links the symmetry as the wall is approached (within each mode) to the shape of the modes. Therefore, all the zeroes in a given mode can be deduced from the zeroe closest to the wall, or, equivalently, from the stretching factor of order $(n-1)$, λ_{n-1} (according to (5.5)). In each mode, the ratio between the smallest length scale and the largest one can be expressed as a function of c_n, i.e. $z_1^{(n)}/l_n = c_n^{1-n}$. The relation between

the spectral stretching factor λ_i and the compression factor c_n within each mode is given by the equation

$$(\lambda_i)^{i-n}(c_n)^n - (c_n)^i + 1 - (\lambda_i)^{i-n} = 0 \,. \tag{5.10}$$

In particular, this can be applied to the mother ($n = N$) for which the smallest length scale is the Kolmogorov length scale η.

Equation (5.9) is valid for odd modes only since the existence of a zeroe at the center of the channel has been used. For even modes, the boundary condition at the center can also be written. Since the latter does not correspond to a zeroe, the derivation of an expression similar to (5.9) for even modes needs the consideration of all points.

5.1.3 Proposed form of the mapping between the modes

The next step in understanding the symmetry along the spectrum is the characterization of the operator S mapping $\phi_{n,odd}$ into $\phi_{n-1,odd}$. For this purpose, I need to express the stretching factor λ_i , or equivalently, the exponent a_i, as a function of i. Here, I recall that as one approaches the wall and the smallest length scale (l_n) tends to the Kolmogorov length scale, the stretching factor λ_i tends to one, or the exponent a_i tends to zero as i tends to infinity. The simplest law which realizes such an asymptotic behavior is the inverse proportionality:

$$a_i = -\frac{1}{\alpha i + \beta}, \tag{5.11a}$$

$$b_i = -i a_i. \tag{5.11b}$$

where two parameters (most likely Reynolds number dependent) are involved. While the consistency with equations (5.10) is difficult to check analytically, it can be guaranteed numerically for given values of the parameters (see, e.g., Section 5.2).

I now return to the stretching property (5.3) which expresses the fact that, in the (i,n)-space, the stretching factor λ is a function of i only. Writing the operator S, however, requires λ as a function of y, which is obtained by mapping the (i,n)-space to the (y,n)-space. Equations (5.6) and (5.11) imply that

$$\ln z_i^{(n)} = \frac{i-n}{\alpha i + \beta} .$$

(Note that, formally, if $\beta \neq 0$, then the previous formula is not valid at the center of the channel. In numerical applications (see, e.g. Section 5.2), the results are not very affected by this inconsistency.) I now use (5.4) to extrapolate this relation to any point and obtain $y_j^{(n)}$, as a function of j

$$\ln y_j^{(n)} = \frac{j-n}{\alpha j + \beta},$$

which, upon inversion, leads to the indexation process

$$j = \frac{n + \beta \ln y_j^{(n)}}{1 - \alpha \ln y_j^{(n)}}. \tag{5.12}$$

By substituting (5.12) into (5.4), I obtain

$$\lambda_n(y) = e^{1/(\alpha n+\beta)} y^{-\alpha/(\alpha n+\beta)} , \tag{5.13}$$

where I have dropped the subscript and superscript for y. The two-parameter stretching operator then becomes

$$(S\phi_{n,odd})(y) = \phi_{n,odd}(\frac{y}{\lambda_n(y)}) = \phi_{n-1,odd}(y), \tag{5.14}$$

where $\lambda_n(y)$ is given by (5.13).

Remark: from eq. (5.11a) and considering as above $l_N = \eta$, the index N of the mother function can be resolved as a function of the Kolmogorov length scale:

$$N = 1 - \frac{1}{\alpha}\left[\beta + \frac{1}{\ln(1-\eta)}\right]$$

5.2 Analysis of a Numerically Computed Turbulent Channel Flow

I now use data likely to exhibit the scaling laws of Section 5.1. Since full, well-resolved, three-dimensional, temporally evolving turbulent fields would require a huge amount of data storage on computers, it is reasonable to start the investigation on a simpler, more tractable problem. Furthermore, since the main purpose of this work is to show that self-similarity is present in a (strongly) inhomogeneous direction of the flow, I concentrate on such a direction only, setting aside for the moment the study of the symmetries in time and in the other directions. One of the advantages of the space-time symmetries recalled above is that they can be detected on the spatial two-point correlation when the latter is defined with a time average. The elimination of the other directions, say x and z, is less straightforward. One way to achieve this consists in including the plane (x and z) average so that the two-point velocity correlation tensor becomes

$$R_{ij}(y,y') = \int_{XZT} u_i(x,y,z,t)u_j(x',y',z',t)d(x-x')d(z-z')dt \ . \qquad (5.15)$$

The spectral decomposition of the operator whose kernel is (5.15) coincides with the proper orthogonal decomposition (POD) technique in the y-direction. A similar method was applied to experimental turbulent wake flow data [11, 12] and the track of a stretching symmetry was identified, although the lack of well-resolved data did not allow a quantitative study.

A well-resolved database is that extracted from Kim *et al.*'s [13] direct numerical simulation of a turbulent channel flow. The flow geometry and the system of coordinates are shown in Fig. 5.1. The POD was computed for this flow by Moin and Moser [14], in both one dimension (as in (5.15)) and three dimensions. Many other analyses of the same data have been performed [15, 16, 17] (see also references

[18, 19, 20] for the analysis of similar flows). Using the same data kindly provided to us by Moser, Moin and Kim, we repeat the POD computation in one dimension, the only difference being the domain considered. Here, I consider the full channel flow domain while Moin and Moser considered half of the channel only. For this reason, our eigenmodes are different from those of reference [14]. The Reynolds number based on the centerline velocity U_0, and the channel half-width, δ, is 3300. The channel centerline corresponds to a distance from the wall $y^+ = yu_\tau/\nu = 180$ where u_τ is the shear velocity. Hereafter, all velocity and length scales are normalized with u_τ and δ, respectively. The computation was performed using Fourier modes in the streamwise x and spanwise z directions, and Tchebishev polynomials in the normal (y) direction, over $128 \times 129 \times 128$ grid points. The periods of the computational box are $4\pi\delta$ in the x-direction and $2\pi\delta$ in the z-direction. The grid-points in the normal direction, given by

$$y_j = -\cos\left[\frac{\pi(j-1)}{N-1}\right] \quad 1 \le j \le N$$

are used in the computation of the two-point correlation (5.15). The total averaging time is about $190\delta/U_0$. More details can be found in references [13, 16].

The POD (eigen)modes, solutions of the eigenvalue/eigenfunction problem

$$\int_Y R_{ij}(y,y')\phi_j^n(y')dy' = B_n\phi_i^n(y), \tag{5.16}$$

are required to be orthonormal, i.e.

$$\int_Y \phi_i^n \phi_i^m dy = \delta_{nm} .$$

The kinetic energy (defined with an average over the three spatial directions and time) corresponding to each mode is given by the eigenvalue B_n. The sum of the eigenvalues,

$$E = \sum_n B_n,$$

represents the total turbulent energy. Figure 5.2 shows the first 100 eigenvalues of the spectrum of (5.16) capturing 99.9% of the total energy. The structure of this spectrum is not discussed in detail here, since it corresponds to the three velocity components. I only point out that, in logarithmic scale, the eigenvalues, except the first few ones, have the tendency to align on a straight line, indicating that the spectrum law decays exponentially and that the corresponding part of the velocity field is self-similar (see Section 2.2.3). In what follows, I concentrate on the streamwise component of the eigenmodes, i.e. ϕ_{1n}, referred to as ϕ_n. As discussed earlier, it is always possible to choose either odd or even eigenfunctions. Figure 5.3(a) displays twenty odd modes which seem to be recurrently related. In the following, we refer to this family of modes as $\{\phi_{n,odd}\}_{n=1}^{20}$, keeping in mind that n is now the index within the set. An analogous family of nineteen even modes, $\{\phi_{n,even}\}_{n=1}^{19}$, is displayed in Fig. 5.3(b). Although more similar modes of the same families could be extracted (further down the spectrum), they are not represented here. The displayed modes are sufficient for the confirmation and derivation of the similarity law; once this is achieved, additional modes can be easily generated. The extracted modes contain 86% of the total energy contained in R_{ij}, $i,j = 1,2$. The reconstruction of the correlations from these two series of modes and the original eigenvalues is shown in Fig. 5.4. Figure 5.4 also displays a reconstruction based on the first pair of modes $(\phi_{1,odd}, \phi_{1,even})$.

I now study the two previous families of functions. Figure 5.5(a), (b) show the eigenvalue spectra in logarithmic scale corresponding to each subset. Although both curves have some small concavity, particularly in the energy containing range of the spectra (i.e. consisting of the first few eigenvalues), straight lines are good approximations, the slopes from least mean square fits being -0.414 and -0.417. The fact that the two slopes are nearly the same is confirmed by Fig. 5.5(c) which displays the two spectra. In addition, the regular interlacement of the eigenvalues shows that

the selected modes alternate in parity. Next I explore whether these families obey stretching laws as those described in Section 5.1. Figure 5.3 displays the selected eigenvectors and shows how the latter are qualitatively related: starting from the last mode of each series, $n = 20$ or $n = 19$, and stretching $\phi_{n,odd}$ from the center of the channel toward the walls until the zeroes closest to the walls reach $y = \pm 1$, we obtain $\phi_{n-1,odd}$, stretching $\phi_{n-1,odd}$, we obtain $\phi_{n-2,odd}$, etc. All modes can thus be deduced from the last one by a stretching action. The odd modes $\phi_{n,odd}$ have thus $2n + 1$ zeroes and the even modes $\phi_{n,even}$ have $2n$ zeroes. As showed in Section 5.1, the stretching can be represented by an operator S mapping $\phi_{n,odd}$ into $\phi_{n-1,odd}$. I investigate the nature of this mapping by first studying the zeroes of the functions. For this, I restrict my study to half of the functions ($0 < y \leq 1$), the other half being recovered by reflection symmetry. In Fig. 5.6, the location of the zeroes $z^{(n)}_{i,odd}$ and $z^{(n)}_{i,even}$ for all values of n and i is displayed in logarithmic scale.

The fact that the i-th zeroe remains located on a straight line as the mode index n varies (except for low order modes) confirms the existence of a recurrence relation

$$z^{(n+1)}_{i,odd} \longrightarrow z^{(n)}_{i,odd} \longrightarrow z^{(n-1)}_{i,odd} \longrightarrow \cdots \longrightarrow z^{(i)}_{i,odd} = 1.$$

of the form (5.6). This can be observed in Fig. 5.6(b) which is a zoom of the top right hand corner of Fig. 5.6(a) in which the first five zeroes are excluded. Here, it is also clear that the slopes $a_{i,odd}$ of each line depends on the index i of the zeroes, or equivalently on the position of each zeroe in the last mode $\phi_{20,odd}$ or $\phi_{19,even}$. This dependency of the exponent $a_{i,odd}$ or, equivalently, that of the dilation coefficient, $\lambda_{i,odd}$, with i confirms that the original dilation symmetry (2.25) adapts to the wall boundary conditions (as in (5.3)). Close to the wall, i.e. as values of i increase, straight lines tend to become parallel to the wall, or, equivalently, the stretching factor tends to one. The subplot of Fig. 5.6(b) shows that the exponent $a_{i,odd}$ is inversely proportional to i, confirming the two-parameter model (5.11) where $\alpha_{odd} = 1.60$ and

$\beta_{odd} = 7.29$ are computed from a least mean square fit. Fig. 5.6(c), (d) show the same property for the even mode family where the two parameters take the values $\alpha_{even} = 1.59$ and $\beta_{even} = 8.27$. While the numerical values of α are very close in both cases, the discrepancy between β_{odd} and β_{even} is due to the fact that the zeroes $z_{i,odd}^{(n)}$ and $z_{i,even}^{(n)}$ do not coincide, especially in the vicinity of the center of the channel. The stretching factors themselves are represented in Fig. 5.7. The locations of the zeroes computed from the stretching factor, λ_i, (5.5) is compared with the original positions in Fig. 5.8 for $i > 5$. A good agreement is found. Returning to Fig. 5.6(a), I observe that the previous features persist for the first zeroes (close to the center of the channel), for relatively high order modes. The range of values of n over which (5.3) is valid extends fast to low values as i increases: at $i = 6$, (5.3) holds for all n. In the complementary part of the (i, n) plane, the stretching factor depends on both i and n. More precisely, it increases as n decreases, so that stretching is larger than that given by (5.3). This adjustment of the symmetry to the center of the channel (located at finite distance from the walls) will also be clear when modes are generated from the mapping (5.14).

In the part of the (i, n) plane where (5.3) is valid, I investigate the stretching property of the flow as the distance from the wall is increased, in each mode. In order to test equation (5.7), I study the location of the zeroes in each mode. Fig. 5.9 clearly confirms the compression law (5.7) (for $n > 5$) for both the odd and even mode families. The compression factor c_n, independent of i, clearly varies with n, tending to 1 as n increases. This dependency on n is displayed in the subplots of Fig. 5.9.

The next step consists in computing the zeroes of the odd modes from equation (5.9) where c_n is deduced from the distance to the wall of the (n-1)-st zero in the n-th mode, $l_n = 1 - z_{n-1}^{(n)}$, and equation (5.8). The extraction of l_n from the modes

is displayed in Fig. 5.10(a) while the positions of the zeroes computed from (5.9) are compared with the original location in Fig. 5.10(b). As an intermediate step, the one-to-one relation between the length scale l_n and the compression factor c_n obtained by solving (5.8) can be read in the subplot. This computation compares well with that obtained in Fig. 5.8(a).

I show now that the modes can be generated from one odd mode and one even mode by the operator (5.14) in which the stretching factor is taken of the form (5.13). The values of the two parameters α and β are those previously found by the data analysis. In Fig. 5.11(a), the original functions $\phi_{n,odd}$, $\phi_{n,even}$ are compared with those obtained by successive applications of S starting from the last mode ($n = 20$ or $n = 19$). Fig. 5.11(b) displays the same comparison for the even mode series. As the previous study of the location of the zeroes showed, the computation gives reliable results for $n \geq 5$ for the two families. In the "energetic range" of the spectrum ($n < 5$), the stretching factor is larger in the original flow.

5.3 A Revised Model

From the analysis of the previous numerical simulation, it is clear that the stretching law (5.13) is not the correct one for large eddies, i.e. small values of n. Mathematically speaking, the stretching is not large enough, or, physically speaking, these high energy modes, in direct contact with the walls, have to "bend" more than (5.6) to adjust to the boundary conditions. This can be confirmed from either Fig. 5.6, or Fig. 5.11. The adjustment of the large eddies to the wall no-slip boundary condition manifests itself as a departure from the linear equation (5.6) and a higher order relation is obviously needed. The degree of the polynomial characterizes the influence of the wall on the large eddies in a somewhat quantitative manner. This question is

answered in Fig. 5.12, where the zeroes of the functions (for small values of n) are fitted accurately by means of quadratic polynomials in n whose coefficients are only functions of the index i. Although a procedure similar to that described in Section 5.1.3 can be performed, the inversion achieved in the derivation of the mapping now involves a high order polynomial in i. Consequently, the expression of the stretching factor (5.13) cannot be given in a compact form. Note that the new stretching factor depends on both the location in the channel and the index of the mode considered.

5.4 Conclusions

Kolmogorov's scaling laws for homogeneous turbulence can be extended to inhomogeneous flows by using the scaling symmetries of the Navier-Stokes equations and assuming that the flow is itself self-similar. As seen in Chapter 2, this self-similarity manifests itself in the description of the flow by families of modes. Each of these families is characterized by a spatio-temporal mother mode from which the rest of the set can be deduced (see equations (2.26), (2.27), (2.29, and (2.30)). The former model, only valid in an infinite spatio-temporal domain, was extended in this chapter to the case of wall-bounded shear turbulence. The stretching action persists, but gets deformed by adapting itself to wall boundary conditions. The stretching factor is independent of the mode index, n, but depends on the index j of the point considered in the mother. As there is a cascade of energy down the spectrum, there is a cascade toward smaller scales also as the wall is approached at each energy level, namely in each eigenmode. The stretching there is independent of the distance to the wall, but depends on the mode index n. I have derived an explicit relation connecting both stretching factors and shown that, within a self-similar family, i) all modes can be deduced from their mother and ii) the shape of the modes is related to the symmetries

themselves. In particular, the positions of all zeroes of all functions (within the same family) can be deduced from the stretching symmetries.

The analysis of statistical data obtained from direct numerical simulation of a turbulent channel flow by Kim *et al.* [13] agrees with the model. Two self-similar families of modes were extracted, due to the reflection symmetry of the flow about the centerline, one set of odd modes, one set of even modes. In each set, both dilation symmetries, the first one along the spectrum of energy and the other one as the wall is approached, were confirmed, in an "inertial" range of the spectrum, excluding the first five eigenmodes. The expression of the symmetries is similar for both sets. In the energy containing range of the spectrum including the first five modes of each series, dilation is still present but the precise symmetry laws are not as simple as in the inertial range: the stretching factors depend on both the distance from the wall and the mode index as shown in Section 5.3. There, the symmetry has to adjust to the center of the channel (located at finite distance from the walls), independently of the Reynolds number considered. I have shown that this adjustment can be performed by means of second order polynomials. Whether the scaling in the inertial range discussed here depends on Reynolds number or not is an open question. It seems likely that, as Reynolds number increases, stretching varies through the precise values of the two parameters α and β introduced in Section 5.2. This point, of course, will require further investigations.

References for Chapter 5

[1] R. Z. Sagdeev, S. S. Moiseev, A. V. Tur and V. V. Yanovskii, "Problems of the theory of strong turbulence and topological solitons," in *Nonlinear Phenomena in Plasma Physics and Hydrodynamics*, edited by R. Z. Sagdeev, Advances in Science and Technology in the USSR (Physics Series, Mir Publishers, Moscow), p. 137 (1984); see also S. S. Moiseev, V. I. Petviashvily, A. V. Toor and V. V. Yanovsky, "The influence of compressibility on the self-similar spectrum of subsonic turbulence," PhysicaD **2**, 218 (1981).

[2] U. Frisch, "From global (Kolmogorov, 1941) scaling to local (multifractal) scaling in fully developed turbulence," in *Turbulence and Stochastic Processes* (The Royal Society, 1991), p. 89.

[3] G. W. Bluman and S. Kumei, "Symmetries and Differential Equations," Applied Mathematical Sciences (Springer-Verlag, New York, 1989), Vol.**81**.

[4] R. E. Boisvert, W. F. Ames, and U. N. Srivastava, "Group properties and new solutions of Navier-Stokes equations," J. Engr. Math **17**, 203 (1983).

[5] B. Cantwell, "Viscous starting jets," J. Fluid Mech. **173**, 159 (1986).

[6] N. Aubry, R. Guyonnet and R. Lima, "Turbulence Spectra," J. Stat. Phys. **67**, 183 (1992).

[7] W. Lian and N. Aubry, "Self-similarity of compressible turbulence," FED-Vol. 151 (ASME), 129 (1993).

[8] F. Carbone, and N. Aubry, "Hierarchical order in wall-bounded shear turbulence", Physics of Fluids **8** (4), (1996).

[9] N. Aubry, R. Guyonnet and R. Lima, "Spatio-temporal analysis of complex signals: theory and applications," J. Stat. Phys. **64**, 683 (1991).

[10] H. Tennekes and J. L. Lumley, *First Course in Turbulence* (The MIT Press, Cambridge, 1972).

[11] N. Cao, "Analysis of reduced simulations of laminar/turbulent wake flows," Ph.D. thesis, Levich Institute, the City University of New York, New York, NY (1993).

[12] N. Cao and N. Aubry, "Detection of self-similar modes in turbulence: application to a wake flow," in *Eddy Structure Identification in Free Trubulent Shear Flows*, edited by J. P. Bonnet and M. N. Glauser (Kluwer Academic, Dordrecht, 1993), pp. 215-224.

[13] J. Kim, P. Moin and R. Moser, "Turbulence in fully developed channel flow at low Reynolds number," J. Fluid Mech. **177**, 133 (1987).

[14] P. Moin and R. Moser, "Characteristic-eddy decomposition of turbulence in a channel," J. Fluid Mech. **200**, 471 (1989).

[15] B. Knight and L. Sirovich, "Kolmogorov inertial range for inhomogeneous turbulent flows," Phys. Rev. Lett. **65**, 1356 (1990).

[16] R. Moser, "Kolmogorov inertial range spectra for inhomogeneous turbulence," Phys. Fluids **6**, 794 (1994).

[17] L. Keefe, P. Moin and R. Moser, "The dimension of attractors underlying turbulent Poiseuille flow," J. Fluid Mech. **242**, 1 (1992).

[18] S. Herzog, "The large scale structure in the near-wall region of turbulent pipe flow," Ph.D. thesis, Cornell University (1986).

[19] A. C. Liu, R. J. Adrian and T. J. Hanratty, "Reynolds number similarity of orthogonal decomposition of the outer layer of turbulent wall flow," Phys. Fluids **6**, 2815 (1994).

[20] L. Sirovich, K. S. Ball and L. Keefe, "Plane waves and structures in turbulent channel flow," Phys. Fluids A **2**, 2217 (1990).

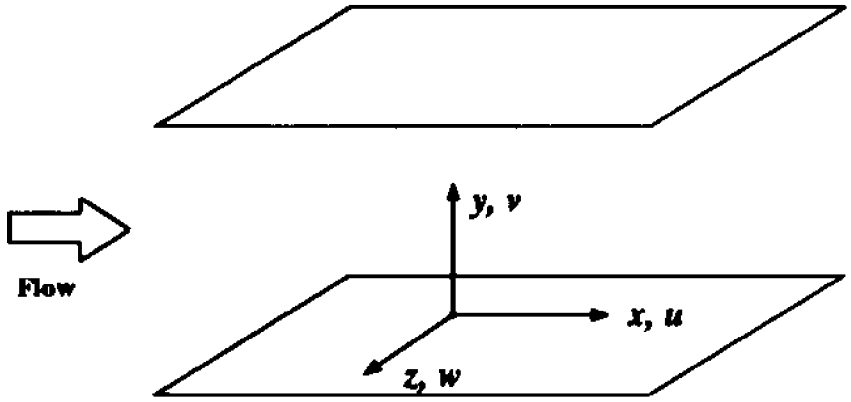

Figure 5.1: Coordinate system in the channel

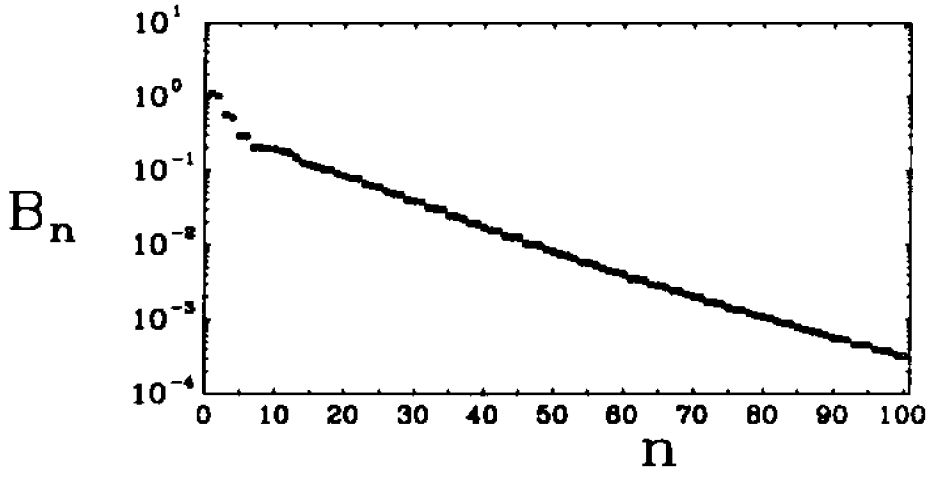

Figure 5.2: POD spectrum corresponding to the two-point correlation tensor $R_{ij}(y, y')$; only the first one hundred eigenvalues are shown.

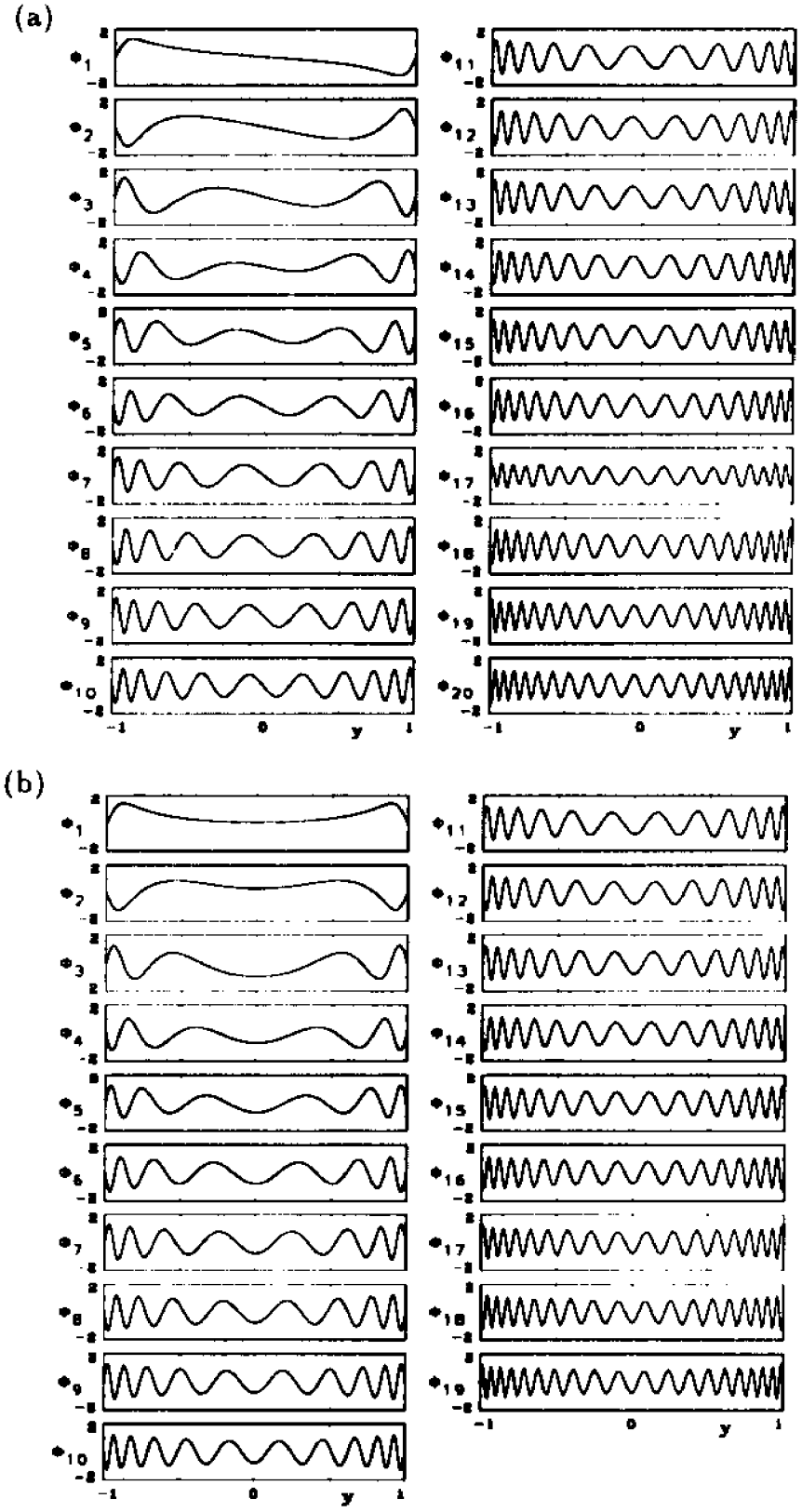

Figure 5.3: The two extracted self-similar families of modes: (a) the odd mode family $\{\phi_{nodd}\}_{n=1}^{20}$; (b) the even mode family $\{\phi_{neven}\}_{n=1}^{19}$.

(a)

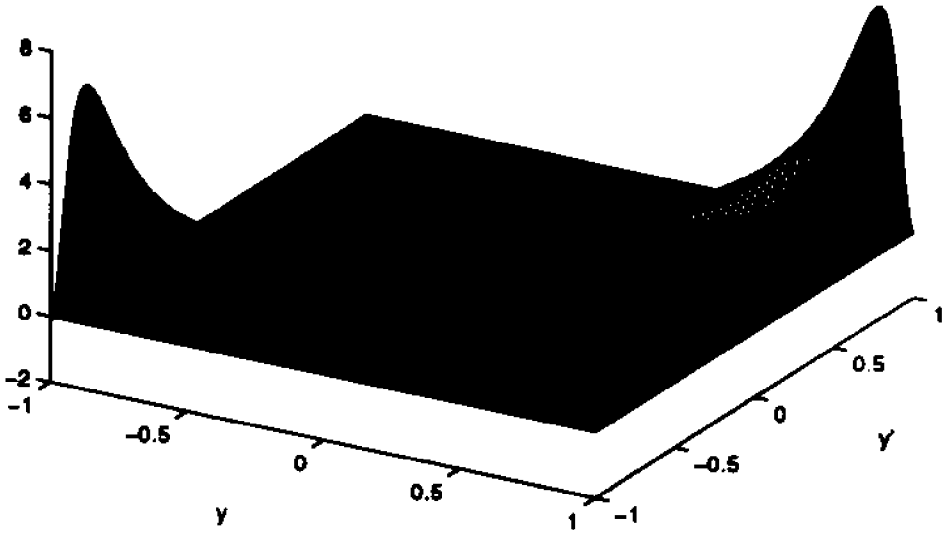

(b)

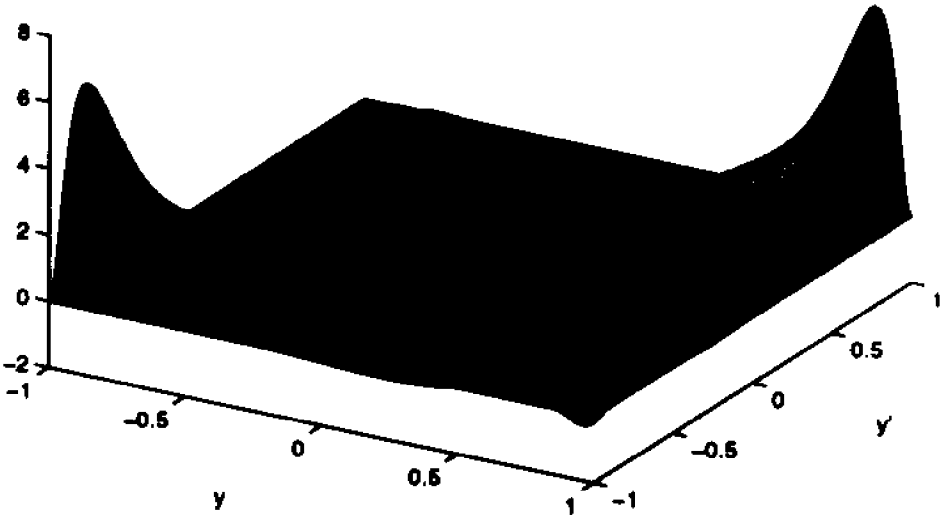

Figure 5.4: The streamwise correlation $R_{11}(y,y')$: (a) the original correlation $R_{11}(y,y')$, (b) that restricted to the two families of modes studied in this paper, next page (c) the autocorrelation $R_{11}(y,y)$: the original autocorrelation (solid line), the autocorrelation reconstructed with the first pair ($\phi_{1odd}, \phi_{1even}$) (dashed line), the autocorrelation reconstructed with the odd mode and even mode families studied in this paper (dotted line).

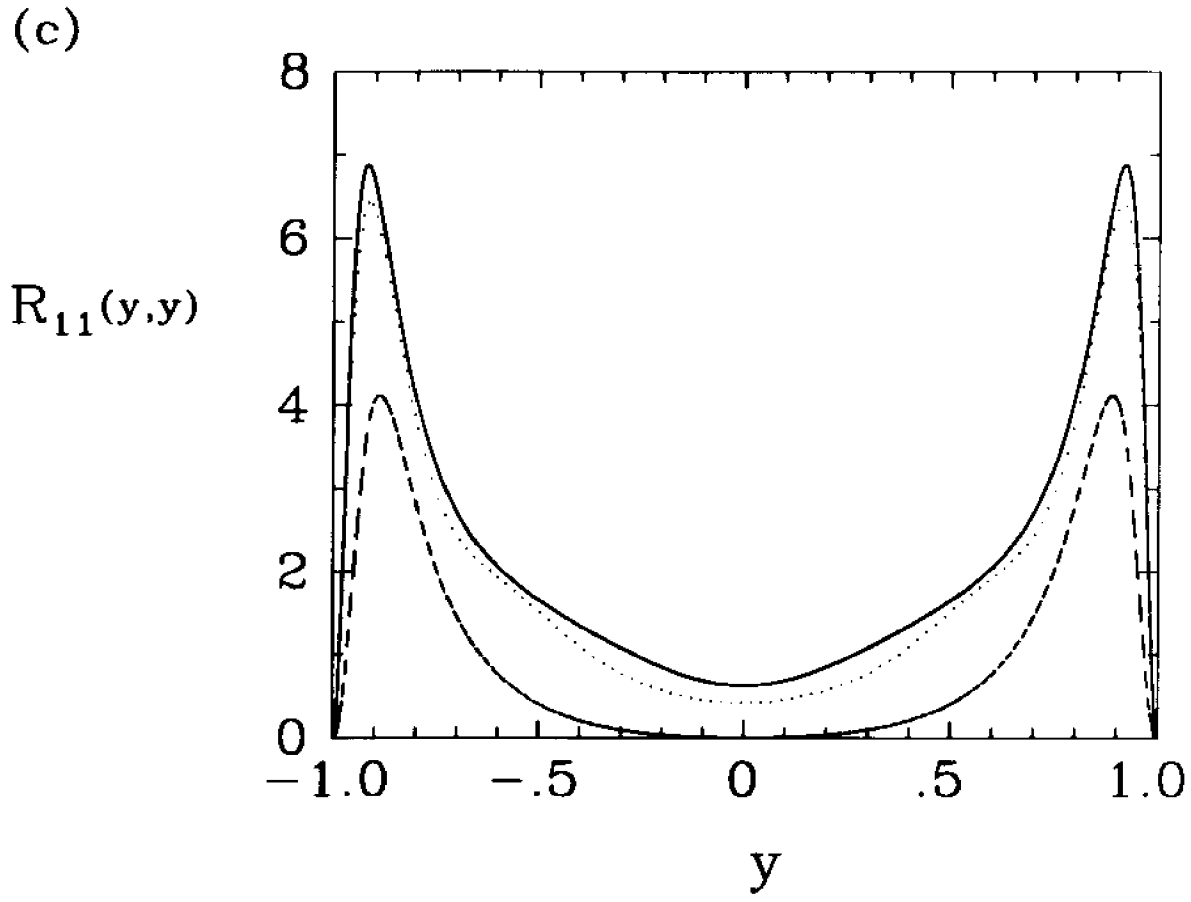

Figure 5.4 continuation

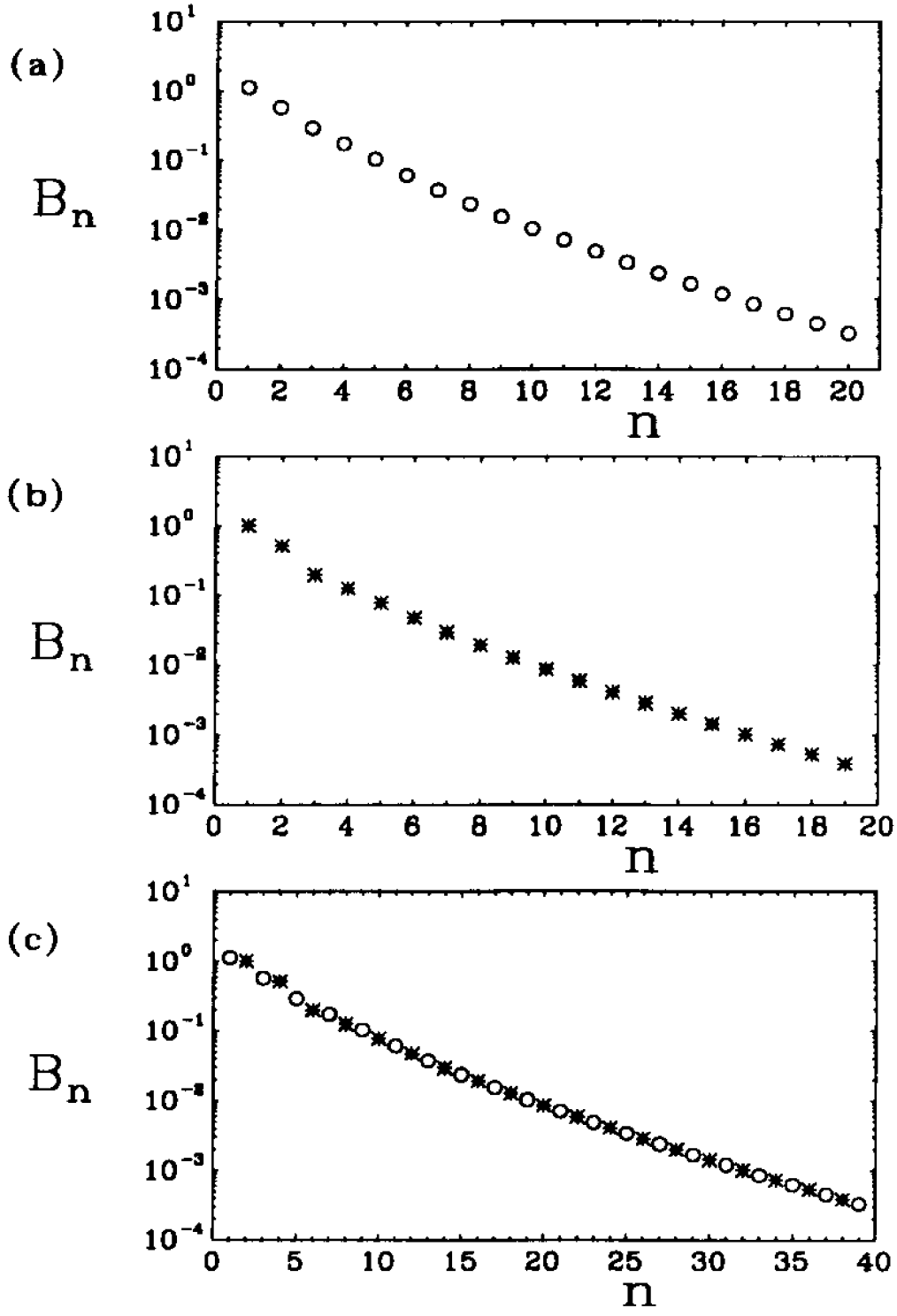

Figure 5.5: POD spectrum B_n of: (a) the odd mode family $\{\phi_{nodd}\}_{n=1}^{20}$, (b) the even mode family $\{\phi_{neven}\}_{n=1}^{19}$, (c) the odd mode (circles) and even mode (stars) families.

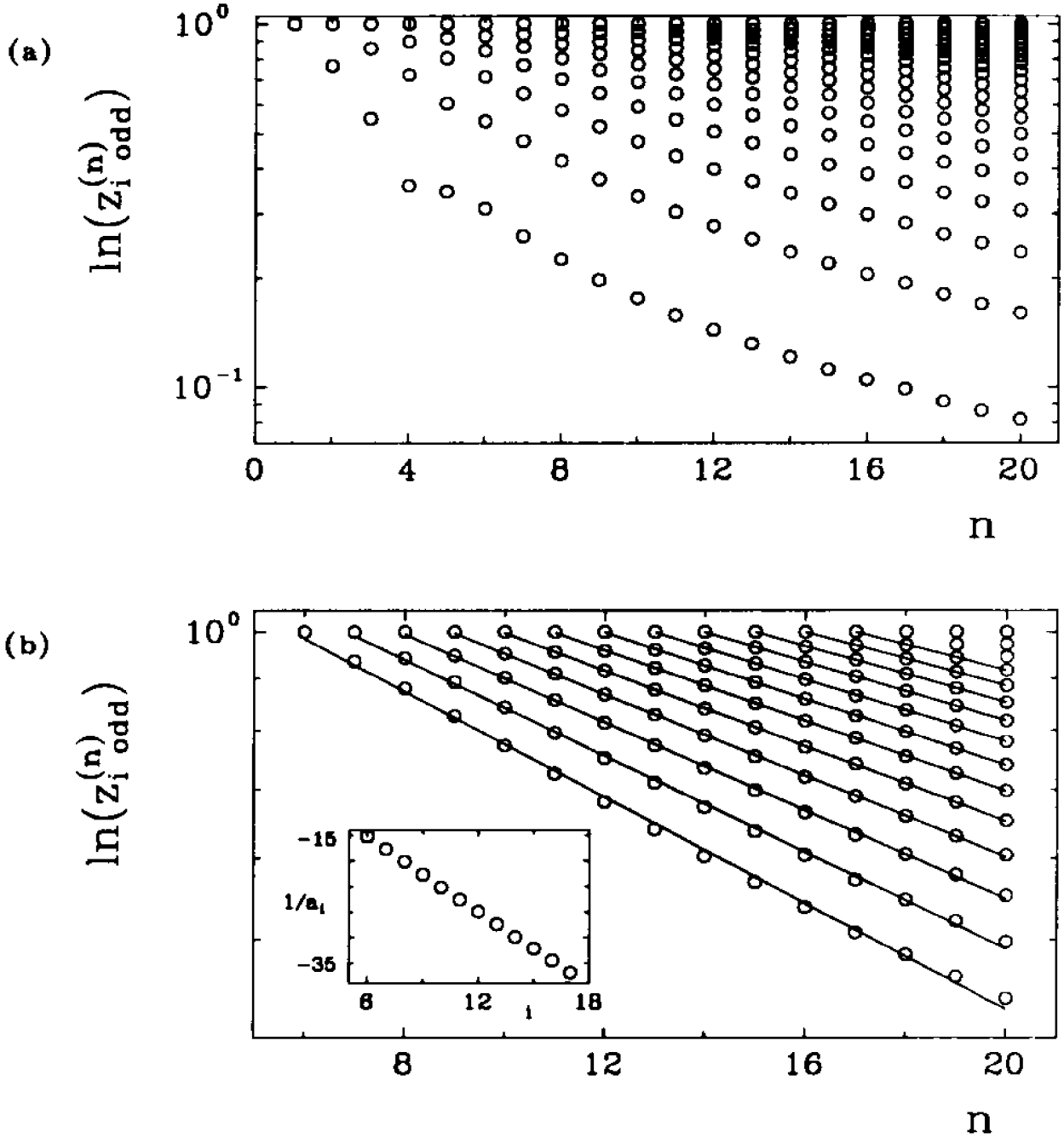

Figure 5.6: Location of the zeroes of the modes, $ln(z_i^{(n)})$, versus n : (a) for the odd mode family, (b) zoom on the top right hand corner of (a) ($i > 5$) showing that, in this domain, the i-th zeroe remains on the same straight line for all n, indicating a linear stretching (see equation (5.6) in the text) as n increases ; the subplot shows the linear relation between the inverse of the slope $1/a_i$ of each straight line and the index i of the zeroes; next page (c), (d): the same as (a), (b) for the even mode family.

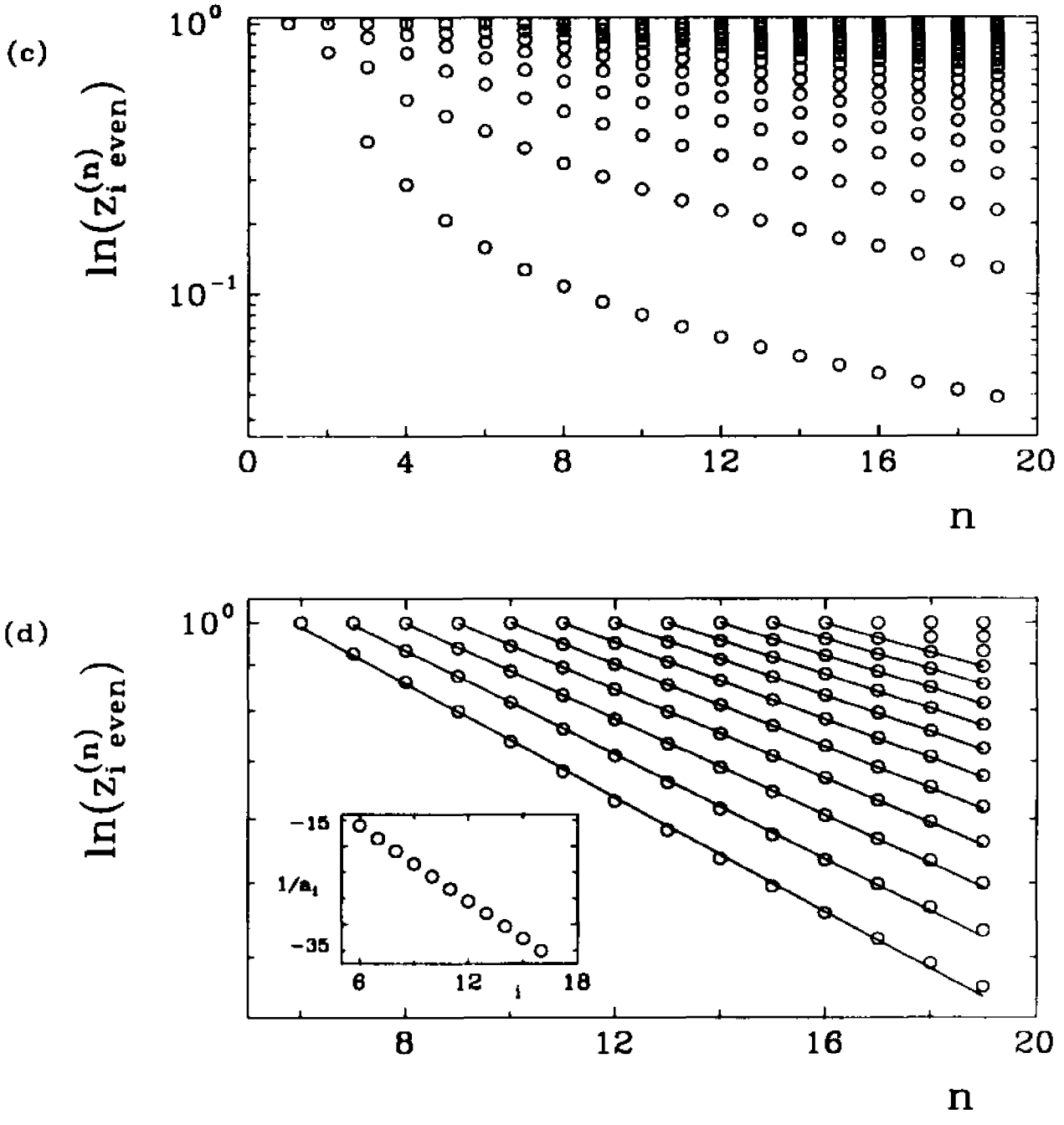

Figure 5.6 continuation

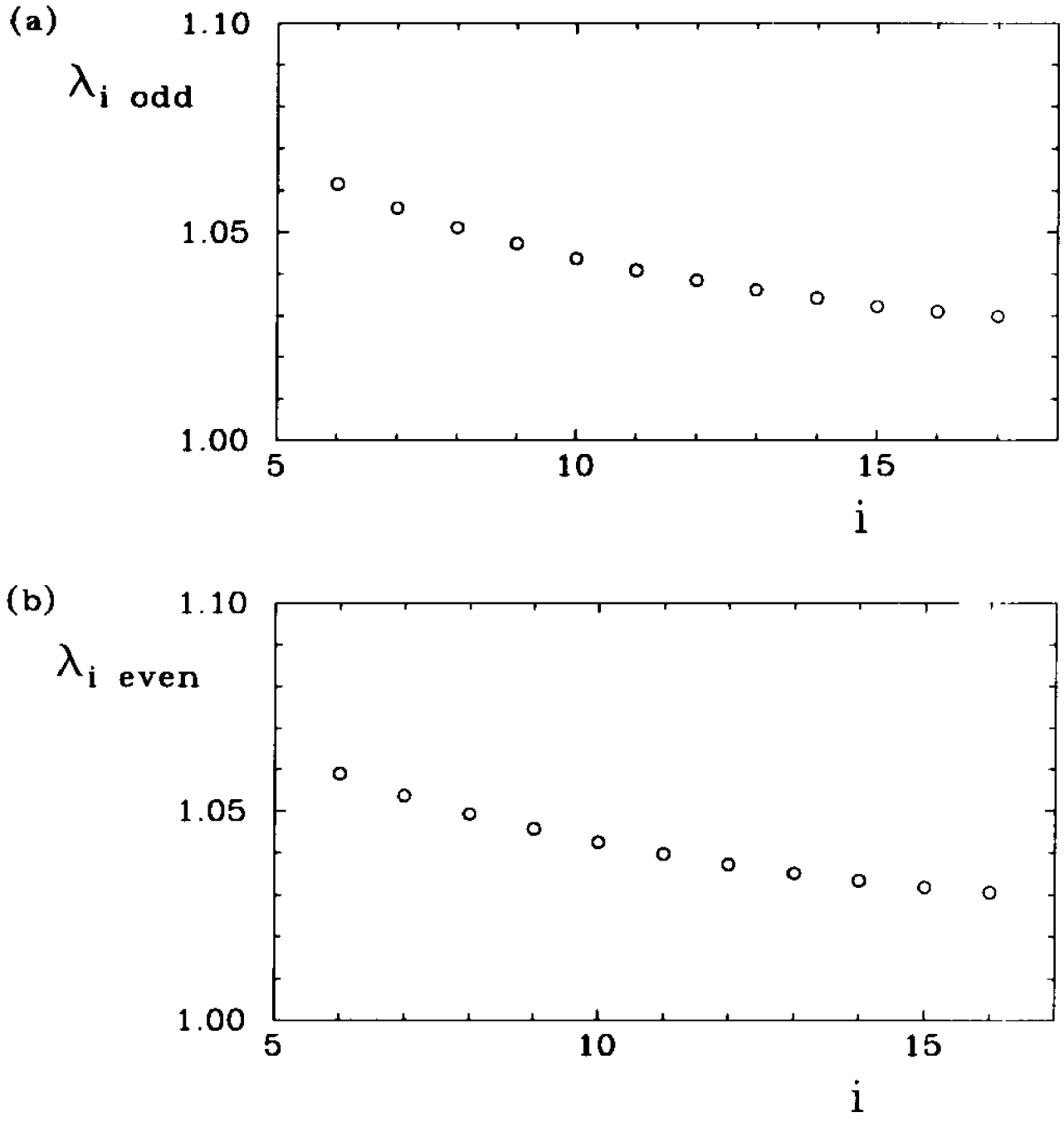

Figure 5.7: The stretching factor, λ_i, involved in the mapping between the modes, as a function of the zeroe index: (a) for the odd mode family, (b) for the even mode family.

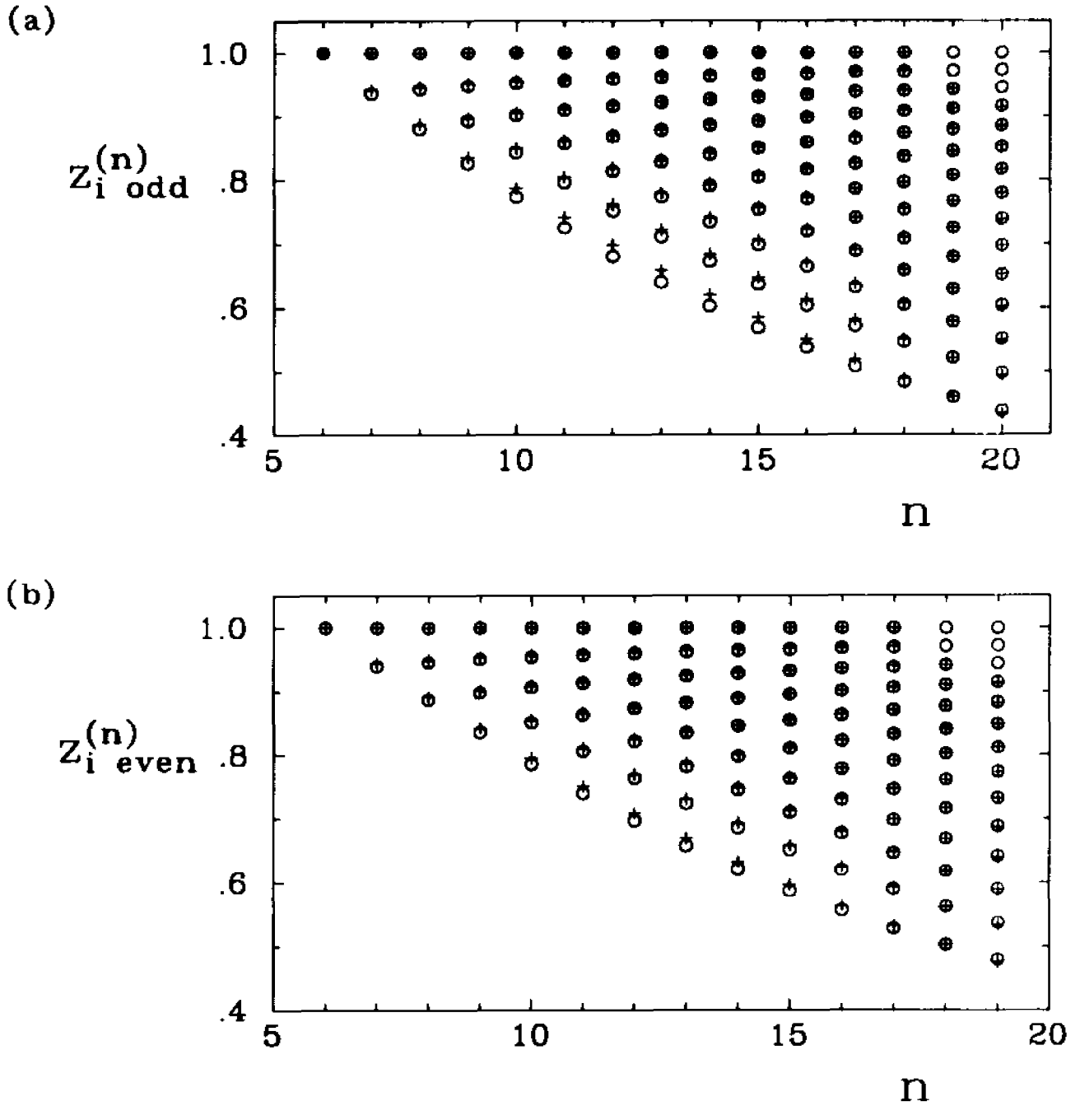

Figure 5.8: Computation of the zeroes from the stretching factor, λ_i, using equation (5.5) in the text (crosses). The reconstructed zeroes can be compared with the original ones (circles): (a) zeroes of the odd mode series, (b) zeroes of the even mode series.

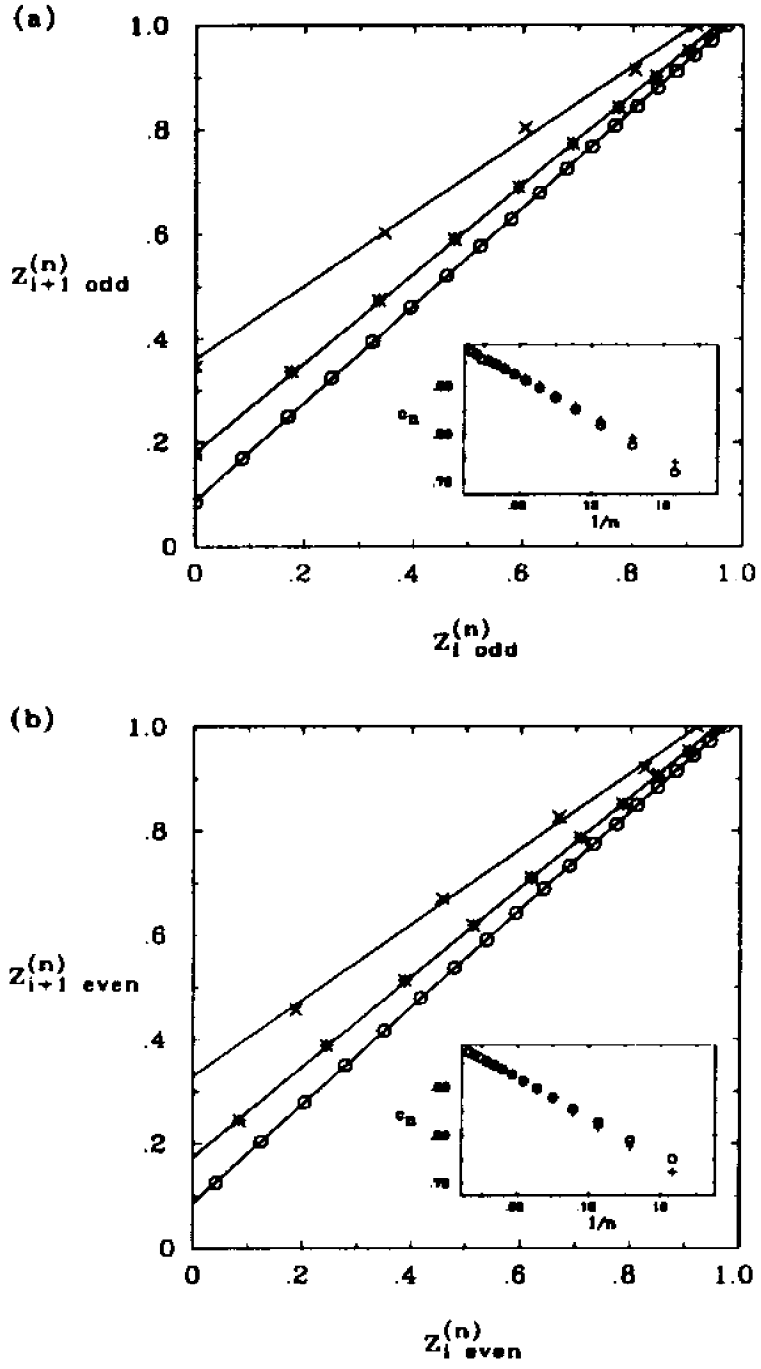

Figure 5.9: The location of the $(i+1)$-st zeroe, $z_{i+1}^{(n)}$, versus the location of the i-th zeroe, $z_i^{(n)}$, (distances are measured with respect to the center of the channel) for $n = 5$ (crosses), $n = 10$ (stars) and $n = 20$ (for (a)) or $n = 19$ (for (b)) (circles): (a) for the odd mode family, (b) for the even mode family. The straight lines show the existence of a compression factor c_n as the wall is approached. The subplot displays c_n versus $1/n$.

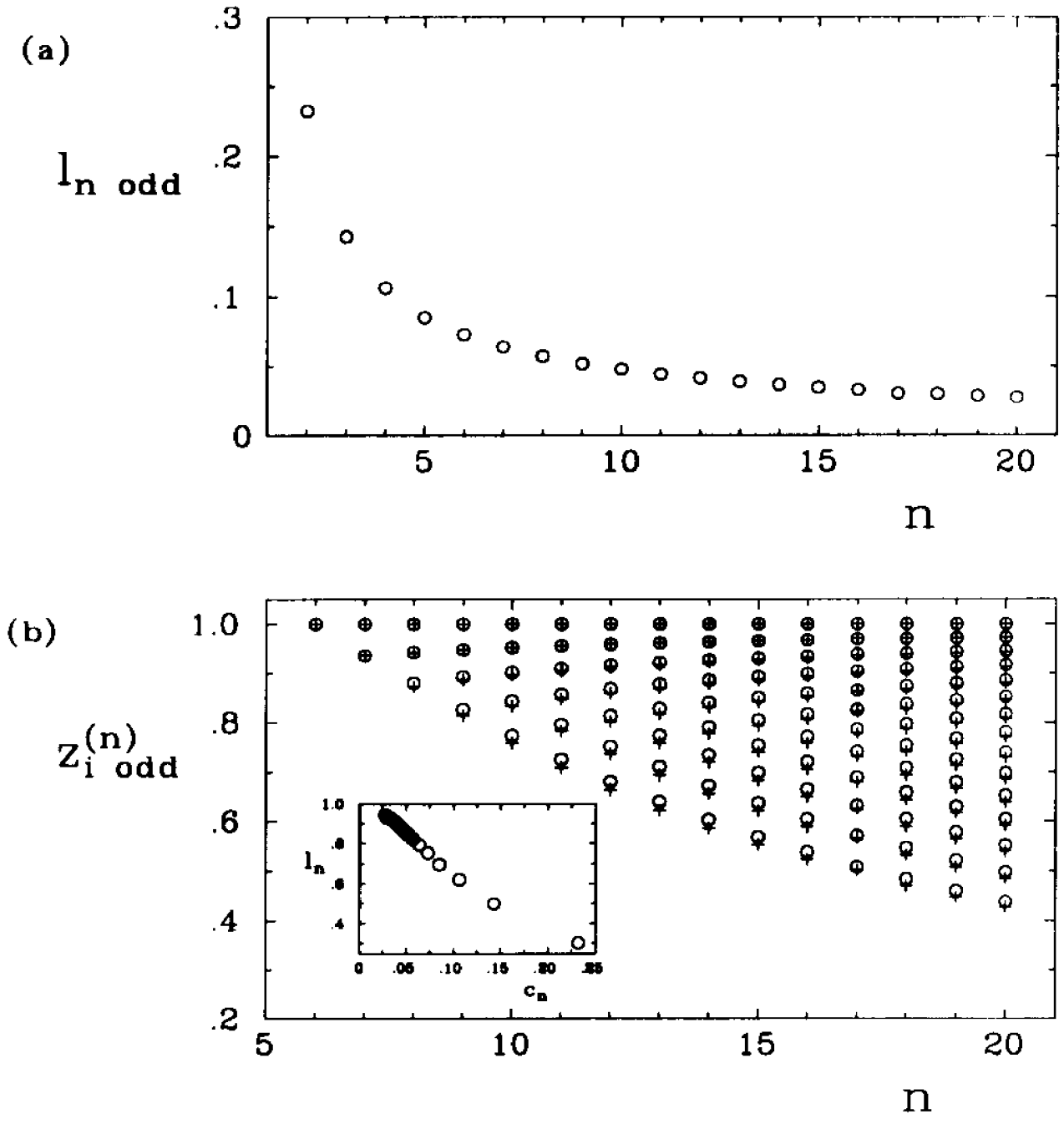

Figure 5.10: Computation of the zeroes in the odd modes from the location of the zeroe closest to the wall in the n-th mode, l_n, or equivalently, the compression factor, c_n, as the wall is approached: (a) l_n versus n; (b) locations of the zeroes for the odd mode family: original zeroes (circles), computed zeroes (crosses); here, we use equation (5.9) in the text (in which we obtain c_n as a function of l_n from (5.8) (see the subplot).

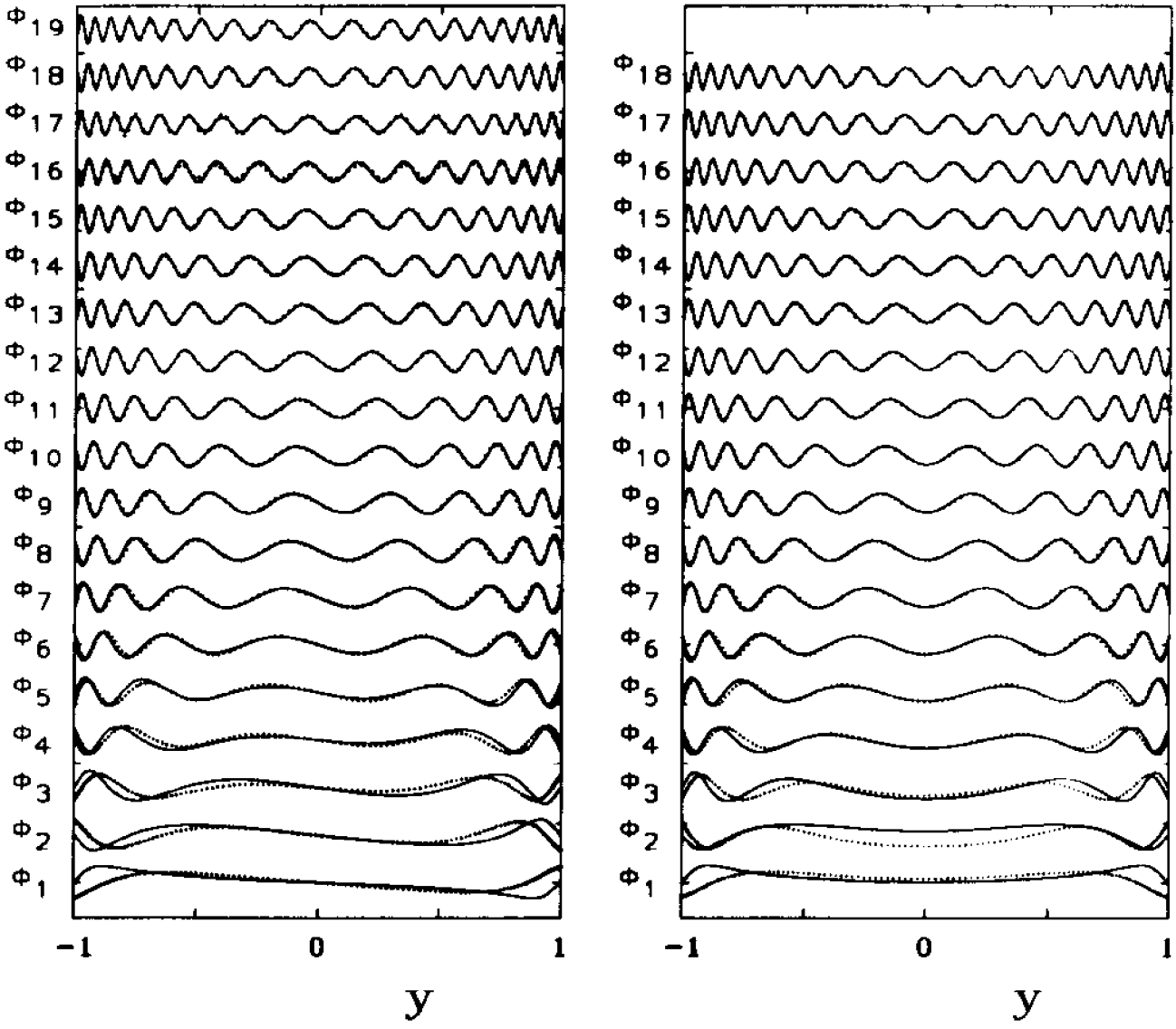

Figure 5.11: Comparison between the original families of modes (full line) and those obtained by successive applications of the operator S (dotted line) from the last function in each series, showing that the symmetry operator leads to a good reconstruction, except for the first few modes. On the left hand side: the set of odd functions; on the right hand side: the set of even functions.

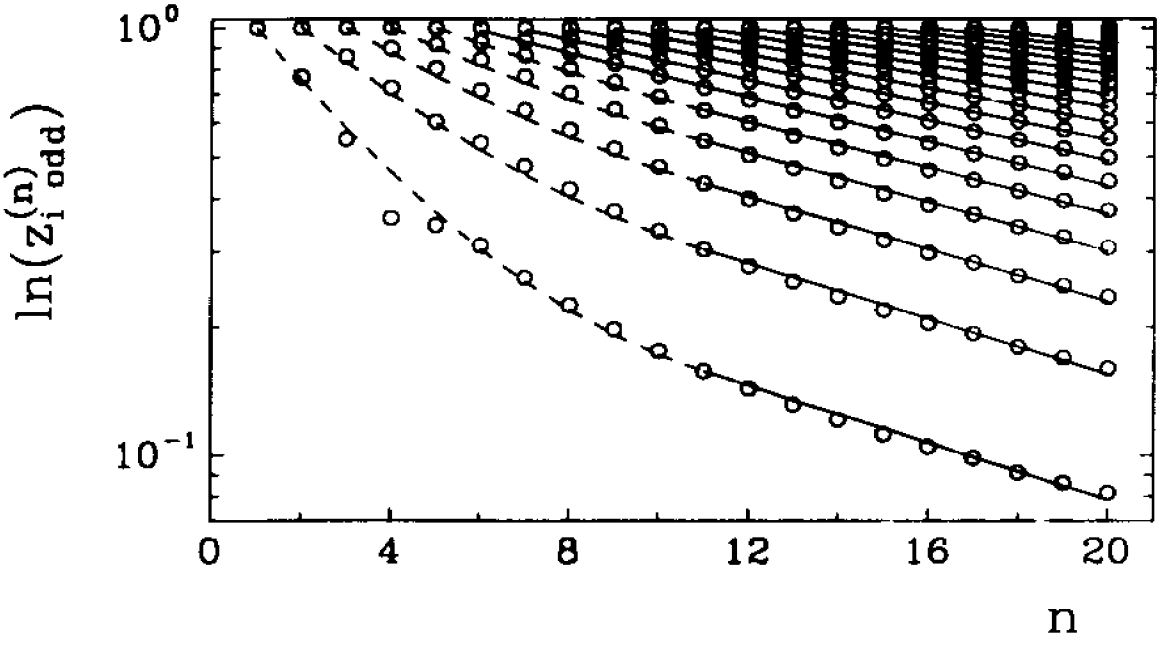

Figure 5.12: The location of the zeroes, $ln(z_i^{(n)})$, versus n, are well fitted by quadratic polynomials in n, for each i: (a) for the odd mode family; (b) for the even mode family.

Chapter 6

Summary and Conclusions

In this work I have concentrated in the understanding of the spatio-temporal dynamical behavior of two complex unsteady fluid systems: a falling film flowing down an inclined plane, and a turbulent wall-bounded shear flow. In both cases, the universal character of spatio-temporal symmetries have played an essential role. The determination of the invariant groups involved in these two flows, together with the "deformation" or "breaking" these symmetry groups may undergo, led to the derivation of simple quantitative models describing their dynamics. These models, based on biorthogonal decompositions, were tested on specific spatio-temporal data. Biorthogonal decompositions, having their foundations in linear operator theory, led to the introduction of the concept of space-time symmetries as operators. This method that defines an isomorphism between space and time, leads also to the identification of spatio-temporal patterns or structures.

Due to the relative novelty of biorthogonal decompositions (compared with more classical data analysis methods like Fourier decompositions), there was no understanding regarding the effect of numerical discretization on the analysis. In this work, I have derived new results equivalent to the sampling theorem of the Fourier analysis.

Indeed, there exists a minimal sampling frequency/wavenumber (the counterpart of the Nyquist condition) such that the biorthogonal decomposition of the discretized function coincides with the discretization of the biorthogonal decomposition of the continuous function.

Regarding the study of falling film flows, I have focussed my attention on the spatio-temporal translation invariance of uniformly traveling waves and its deformation via modulational instabilities, as a route toward space-time complexity. The biorthogonal analysis of experimental data proved that, as Reynolds number increases, uniformly traveling interfacial waves become modulated, first only spatially, and then both spatially and temporally as Reynolds number is increased further [1]. These modulational processes, manifesting themselves in phase space by the thickening of the original trajectories, translate into the splitting and coalescence of wave fronts in physical space. The non-resonant character of these modulations implies that the original space-time translation symmetry present at low Reynolds numbers is not broken but deformed; in addition, the number of biorthogonal modes does not increase. In contrast, the (comparative) Fourier analysis shows a clear increase of the number of modes involved due to the modulations. The biorthogonal decomposition was also able to provide us with a space-time description of the subharmonic instability the system undergoes at higher perturbation frequencies [2]. In particular, the convective character, the spatio-temporal period doubling, and the space-time intermittent behavior of such an instability could be clearly established.

The starting point for the model of wall bounded shear turbulence is the space-time dilation symmetry (5.1) of the Navier-Stokes equations (1.1) already studied in the biorthogonal decomposition context by Aubry *et al.* [3] in their extension of Kolmogorov's scaling law to inhomogeneous turbulence. For wall-bounded flows, the above symmetry no longer holds; in this work, I have presented an extension of the

former theory to the case of finite boundary conditions [4]. The new arguments still predict the existence of families of modes as in [3]; within each family, all modes are hierarchically generated by a basic one (the "mother") through generalized dilation symmetry operators in which the stretching factor is independent of the mode index, n, but depends on the index j of the point considered in the mother. In addition to the previous energy cascade generated by the dilation operator along the (biorthogonal) spectrum, there is also a cascade toward smaller scales as the boundary is approached within each eigenmode. The proper biorthogonal decomposition of statistical data obtained from direct numerical simulation of a turbulent channel flow by Kim *et al.* [5] confirms the model within the inertial range of the spectrum. Higher energy modes still display a dilation relation but the latter is slightly more complex: in this range of the spectrum, the walls of the channel have a strong influence on the modes as shown by studying the location of the zeroes of the modes in logarithmic scale. Here, the linear behavior of the inertial range is replaced by quadratic polynomials.

The significance of these findings lies on a somewhat paradoxical situation: an extremely chaotic system in physical space has a very ordered and simple description in a (well-chosen) functional space. The knowledge of both the symmetries and the mother functions (that are also symmetry dependent) suffices to generate the complex flow. Besides its intrinsic theoretical importance, this result may greatly simplify (and, in some cases, render possible) the numerical simulation of high Reynolds number flows.

References for Chapter 6

[1] F. Carbone, N. Aubry, Jun Liu, J. P. Gollub, and R. Lima, "Space-time description of the splitting and coalescence of wave fronts in film flows", PhysicaD (in press).

[2] J. Liu and J. P. Gollub, Onset of spatially chaotic waves on flowing films, Phys. Rev. Lett. **70**, 2289 (1993).

[3] N. Aubry, R. Guyonnet and R. Lima, "Turbulence Spectra," J. Stat. Phys. **67**, 183 (1992).

[4] F. Carbone, N. Aubry, "Hierarchical order in wall-bounded shear turbulence", Physics of Fluids **8** (4), (1996).

[5] J. Kim, P. Moin and R. Moser, "Turbulence in fully developed channel flow at low Reynolds number," J. Fluid Mech. **177**, 133 (1987).

Bibliography

Alekseenko, S. V. Nakoryakov, V. Y. and Pokusaev, B. G. Wave formation on a vertical falling liquid film, AIChE J. **31**, 1446 (1985).

Aubry, N. Holmes, P. Lumley, J. L. and Stone, E. The Dynamics of Coherent Structures in the Wall Region of a Turbulent Boundary Layer, J. Fluid Mech. **192**, 115 (1988).

Aubry, N. Guyonnet, R. and Lima, R. Spatio-temporal analysis of complex signals: theory and applications, J. Stat. Phys. **64**, 683 (1991).

Aubry, N. Guyonnet, R. and Lima, R. Spatio-temporal symmetries and bifurcations via biorthogonal decompositions. J. Nonlinear Sci. **2**, 183 (1992).

Aubry, N. Guyonnet, R. and Lima, R. Turbulence Spectra, J. Stat. Phys. **67**, 183 (1992).

Aubry, N. Carbone, F. Lima, R. and Slimani, S. Wave propagation phenomena from a spatio-temporal viewpoint: resonances and bifurcations, J. Stat. Phys. **76**, 1005 (1994).

Aubry, N. and Lima, R. "Spatio-temporal and statistical symmetries," J. Stat. Phys. **81**, 793 (1995). (1995).

Aubry, N. and Lima, R. "The dynamics of spatio-temporal modulations," Chaos **5**, 578 (1995).

Batchelor, G. K. "An Introduction to Fluid Dynamics" (Cambridge University Press, Cambridge, 1967).

Benney, J. Long waves on liquid films, J. Math. Phys. **45**, 150 (1966).

Berkooz, G. Holmes, P. and Lumley, J. L. Intermittent dynamics in simple models of the wall layer, J. Fluid Mech. **230** 75 (1991).

Berkooz, G. Holmes, P. and Lumley, J. L. The proper orthogonal decomposition in the analysis of turbulent flows, Annu. Rev. Fluid Mech. **25**, 539 (1993).

Bluman, G. W. and Kumei, S. "Symmetries and Differential Equations," Applied Mathematical Sciences (Springer-Verlag, New York, 1989), Vol.**81**.

Boisvert, R. E. Ames, W. F. and Srivastava, U. N. "Group properties and new solutions of Navier-Stokes equations," J. Engr. Math **17**, 203 (1983).

Cantwell, B. "Viscous starting jets," J. Fluid Mech. **173**, 159 (1986).

Cao, N. and Aubry, N. "Detection of self-similar modes in turbulence: application to a wake flow," in *Eddy Structure Identification in Free Trubulent Shear Flows*, edited by J. P. Bonnet and M. N. Glauser (Kluwer Academic, Dordrecht, 1993), pp. 215-224.

Cao, N. "Analysis of reduced simulations of laminar/turbulent wake flows," Ph.D. thesis, Levich Institute, the City University of New York, New York, NY (1993).

Carbone, F. Aubry, N. Jun Liu, Gollub, J. P. and Lima, R. "Space-time description of the splitting and coalescence of wave fronts in film flows", Physical) (in press).

Carbone, F. and Aubry, N. "Hierarchical order in wall-bounded shear turbulence", Physics of Fluids **8** (4), (1996).

Chang, H.-C. Demekhin, E. A. and Kopelevich, D. I. Nonlinear evolution of waves on a vertically falling film, J. Fluid Mech. **250**, 433 (1993).

Chang, H.-C. Wave evolution on a falling film, Annu. Rev. Fluid Mech. **26**, 103 (1994).

Cheng, M. and Chang, H.-C. A generalized sideband stability theory via center manifold projection, Phys. Fluids A **2**, 1364 (1990).

Cheng, M. and Chang, H.-C. "Subharmonic instabilities of finite amplitude monochromatic waves," Phys. Fluids A **4**, 505 (1992).

Deissler, R. J. Physica (Amsterdam) **25D**, 233 (1987).

Demekhin, E. A. Demekhin, I. A. and Shkadov, V. Y. Solitons in flowing layer of a viscous fluid, Izv. Akad. Nauk. SSSR, Mekh. Zhid. Gaza, No. 4, 9 (1983) [English translation: Fluid Dyn. **18**, 500 (1983)].

Dukler, A. E. in *Progress in Heat and Mass Transfer*, ed. G. Hetsroni, S. Sideman and J. P. Hartnet (Pergamon, New York, 1972) Vol. 6, p. 207.

Frisch, U. Sulem, P. L. and Nelkin, M. J. Fluid Mech. **87**, 719 (1978).

Frisch, U. From Global (Kolmogorov 1941) scaling to local (multifractal) scaling in fully developed turbulence, Proc. Roy. Soc. **A**, (1991).

Fujimura, K. Method of center manifold and multiple scales for weakly nonlinear stability of fluid motions. Proc. R. Soc. Lond. A **434**, 719-733 (1991).

Hamermesh, M. "Group Theory and its Applications to Physical Problems" (Dover Publications, New York, 1989).

Herzog, S. "The large scale structure in the near-wall region of turbulent pipe flow," Ph.D. thesis, Cornell University (1986).

Joo, S. W. Davis, S. H. Bankoff, S. G. On falling film instabilities and wave breaking, Phys. Fluids A **3**: 231-32 (1991)

Joo, S. W. Davis, S. H. Instabilities of three-dimensional viscous falling films, J. Fluid Mech. **242**, 529 (1992).

Joseph Weaver, H. "Theory of Discrete and Continuous Fourier Analysis," (John Whiley and Sons, New York, 1989).

Kapitza, P. L. Kapitza, S. P. Wave flow of thin viscous fluid layers, Zh. Eksp. Teor. Fiz. **19** 105 (1949); also in Collected Papers of P L. Kapitza, edited by D. Ter Haar (Pergamon, Oxford, 1965).

Karhunen, K. "Zur spektral theorie stochatischer prozesse," Ann. Acad. Sci. Fennicae Ser. A **1**, 34 (1944).

Keefe, L. Moin, P. and Moser, R. "The dimension of attractors underlying turbulent Poiseuille flow," J. Fluid Mech. **242**, 1 (1992).

Kim, J. Moin, P. and Moser, R. "Turbulence in fully developed channel flow at low Reynolds number," J. Fluid Mech. **177**, 133 (1987).

Knight, B. and Sirovich, L. "Kolmogorov inertial range for inhomogeneous turbulent flows," Phys. Rev. Lett. **65**, 1356 (1990).

Kolmogorov, A. N. "The local structure of turbulence in incompressible viscous fluid for very large Reynolds number," Dokl. Acad. Nauk SSSR **30**, 301 (1941).

Kolmogorov, A. N. J. Fluid Mech. **13**, 82 (1962).

Kolodner, P. Slimani, S. Aubry, N. and Lima, R. Characterization of dispersive chaos and related states of binary-fluid convection, Physica D, **85**, 165 (1995).

Landau, L. D. and Lifshitz, E. M. "Fluid Mechanics", Course of Theoretical Physics (Pergamon Press, Oxford, 1980), Volume 6.

Lian, W. and Aubry, N. "Self-similarity of compressible turbulence," FED-Vol. 151 (ASME), 129 (1993).

Lin, S. P. Finite-amplitude stability of a parallel flow with a free surface, J. Fluid Mech. **36**, 113 (1969).

Lin, S. P. Finite amplitude side-band stability of a viscous film, J. Fluid Mech. **63**. 417 (1974).

Lin, S. P. and Wang, C. Y. Modeling wavy film flows, in *Encyclopedia of Fluid Mechanics*, edited by N. P. Cheremisinoffs (Gulf, Houston, 1985), Vol. 1, p. 931.

Liu, A. C. Adrian R. J. and Hanratty, T. J. "Reynolds number similarity of orthogonal decomposition of the outer layer of turbulent wall flow," Phys. Fluids **6**. 2815 (1994).

Liu, J. Paul, J. D. and Gollub, J. P. Measurements of the primary instabilities of film flows, J. Fluid Mech. **250**, 69 (1993).

Liu, J. and Gollub, J. P. Onset of spatially chaotic waves on flowing films, Phys. Rev. Lett. **70**, 2289 (1993).

Liu, J. and Gollub, J. P. Solitary wave dynamics of film flows, Phys. Fluids **6**, 1702 (1994).

Liu, J. Nonlinear dynamics of wavy film flows, Ph.D. Thesis, University of Pennsylvania (1994), available through University Microfilms, Inc.

Liu, J. Schneider, J. and Gollub, J. P. Three-dimensional instabilities of film flows Phys. Fluids **7**, 55 (1995).

Loeve, M. "Probability Theory," Van Nostrand, New York (1955).

Lumley, J. L. The structure of inhomogeneous turbulent flows, in: Atmospheric turbulence and radio wave propaganon, eds. A.M. Yaglom and V.I. Tatarski:, Moscow: Nauka, 166 (1967).

Lumley, J. L. Stochasnc Tools in Turbulence, Academic (1970).

Mandelbrot, B. J. Fluid Mech. **62**, 331 (1974).

Moin, P. and Moser, R. D. Characteristic-eddy decomposition of turbulence in a channel," J. Fluid Mech. **200**, 471 (1989).

Moser, R. "Kolmogorov inertial range spectra for inhomogeneous turbulence," Phys. Fluids **6**, 794 (1994).

Obukhov, A. M. J. Fluid Mech. **13**, 77 (1962).

Olver, P. Applications of Lie Groups to Differential Equations, Graduate text in mathematics **107**.

Pumir, A. Manneville, P. and Pomeau, Y. On solitary waves running down an inclined plane, J. Fluid Mech. **135**, 27 (1983).

Rosenau P. and Oron, A. Bounded and unbounded patterns of the Benney equation, Phys. Fluids A **4**, 1102 (1992).

Sagdeev, R. Z. Moiseev, S. S. Tur, A. V. and Yanovskii, V. V. "Problems of the theory of strong turbulence and topological solitons," in *Nonlinear Phenomena in Plasma Physics and Hydrodynamics*, edited by R. Z. Sagdeev, Advances in Science and Technology in the USSR (Physics Series, Mir Publishers, Moscow), p. 137 (1984); see also S. S. Moiseev, V. I. Petviashvily, A. V. Toor and V. V. Yanovsky, "The influence of compressibility on the self-similar spectrum of subsonic turbulence," PhysicaD **2**, 218 (1981).

Salamon, T. R. Armstrong, R. C. and Brown, R. A. Traveling waves on vertical films: Numerical analysis using the finite element method, Phys. Fluids **6**, 2202 (1994).

Sanghi, S. and Aubry, N. Interaction mode models of near wall turbulence, J. Fluid Mech. **247**, 455 (1993).

Sirovich, L. Turbulence and the dynamics of coherent structures: I, II, III Q. Appl. Maths **5**, 561 (1987).

Sirovich, L. Ball K. S. and Keefe, L. "Plane waves and structures in turbulent channel flow," Phys. Fluids A **2**, 2217 (1990).

Tennekes, H. and Lumley, J. L. *First Course in Turbulence* (The MIT Press, Cambridge, 1972).

Trifonov Yu. Ya. and Tsvelodub, O. Yu. Nonlinear waves on the surface of a falling liquid film. Part 1. Waves of the first family and their stability, J. Fluid Mech. **229**, 531 (1991).

Tsvelodub O. Yu. and Trifonov, Yu. Ya. Nonlinear waves on the surface of a falling liquid film. Part 2. Bifurcations of the first-family waves and other types of nonlinear waves, J. Fluid Mech. **244**, 149 (1992).